UNIVERSITÀ DEGLI STUDI DI MILANO

Scuola di Dottorato in Fisica, Astrofisica e Fisica Applicata
Dipartimento di Fisica

Corso di Dottorato in Fisica, Astrofisica e Fisica Applicata
Ciclo XXVIII

Quantum probing and characterization techniques for system of interest in quantum information processing

Settore Scientifico Disciplinare FIS/03

Supervisore: Professor Matteo G.A. PARIS

Coordinatore: Professor Francesco RAGUSA

Tesi di Dottorato di:
Antonio MANDARINO

Anno Accademico 2014/2015

Commission of the final examination:

External Referee:
Professor G. Massimo PALMA

External Members:
Professor Mauro PATERNOSTRO

Professor Francesco PLASTINA

Final examination:

Date 20/01/2015

Università degli Studi di Milano, Dipartimento di Fisica, Milano, Italy

Ai miei Nonni e alle mie Nonne

Cover illustration:
Quantum Technologies

MIUR subjects:
FIS/03

PACS:
03.67.-a
03.65.Yz

Contents

Introduction

Motivation

Quantum physics is a theory born more than 100 years ago, but like all the good theories is like wine: the older the better. In its early stage its interpretation and validity was deeply and debated for long time, because quantum physics shows some spooky features coming into direct conflict with common sense. Anyway in science, particularly in physics, common sense it is not a discriminant when developing a new theory and analysing data. Surprisingly the quantum *mirabilia* have turn to be of practical interest too and not only theoretician brain-teaser to not speak to much about Bell (2004). The turning point could be dated in a seminal paper of Feynman Feynman (1982) who asked if the computer based on the classical theory of information and communication Shannon (2001); Turing (1936) were able to simulate the intrinsic non-deterministic behavior of the phenomena happening in the quantum domain. Quantum computer was and still is the aim and the need of the physicist community involved in quantum information and computation, but a wider range of unexpected applicability was disclosed. The field of quantum technologies now involves among others quantum computing, quantum cryptography, quantum metrology and quantum imaging. All these branches do not simply rely on some quantum effects but instead they are based on the exploitation and manipulation of quantum states in an active way Dowling & Milburn (2003). Another keystone in quantum technologies is the use of quantum effect with no analogue in classical physics, such as entanglement and quantum discord or non-Poissonian distribution when dealing with radiation field just to cite a few.

The features even if promising have some disadvantages they are fragile and quantum mechanics ensures that a quantum states is spoiled when observed. The latter is unavoidable, in fact quantum mechanics implies that a measurement collapses a state into an eigenvalues of the measure quantity, the former is more subtle and it is somehow related to the other. Daring we may state that the surrounding environment is classical and it always, in certain sense, acts as a measurement apparatus on the quantum state, letting it decohere and lose its quantum features. The decoherence theory was firstly introduced as an attempt to clarify the intricate quantum to classical transition dilemma. Anyway the advance of the experimental ability has lead to engineering quantum states in order to preserve and build up quantum features in what are called decoherence-free subspaces. Entanglement is the first form of quantum correlation identified and it has many quantifiers depending on what aspect we would like to catch. For example we can use the relative entropy of entanglement if we want to know how much noise we

have to add to a bipartite system if we want it to be only classical separated; otherwise we can employ the negativity if we want to know how far a bipartite system is far from the set of separable state. Quantum discord is based on the intuition that given a quantity amounting all the correlations between two parties and a reasonable definition for the correlations established between them by local operation and classical communication their differences should quantify non-classical correlation. It has been proven to be more robust than entanglement and to be responsible of a speed-up in certain quantum algorithms. This two measure was largely adopted in different field leading to a quantum bound in the ultra-precise metrology protocol: probing a system with N entangled probes gives a more precise estimation than the same procedure with uncorrelated probes, in figure the variance of the measured quantity scales with N^{-1} instead of $N^{-1/2}$. Quantum correlation and quantum information tools are also widely adopted in the study of condensed matter systems showing phases transition, giving insight to the mechanism of quantum phase transition in a way that usual theory based on order parameter have not been able to do.

Abstract

This PhD thesis collects part of the work I have done during my years as PhD student and it is devoted to the study and understanding of some technique used in quantum information theory. The thread of the main chapters of the thesis is an attempt to clarify some assumptions that sound reasonable but whose correctness has never been proved or demonstrated formally. Although those could not lead to an absurd in a great variety of situations it is not a proper scientific, viz. in the popperian sense, procedure to consider always valid an epistemic even if logical and reasonable statement.

The first question I consider is: Do two quantum states near in the Hilbert space have the same, or almost the same, physical properties?

The answer seems to be obvious and quite naive at first sight but the Hilbert space is a bit more tricky than the classical phase space. First of all we have to clarify with which kind of measure we would like to quantify the distance between two states; in fact the space where quantum states live is endowed of several metric: just to cite a few the usual euclidean one and the Bures metric. I do not consider a proper metric but a function, called Fidelity, that acts from the Hilbert space of a bipartite system to the $\mathbb{R}$-subset $[0, 1]$. Its name is clear when considering a setup able to produce a precise state, if everything is correct in the experimental generation we obtain faithful copies of the original one, but the experimental generation could lead to states that are a little bit different from the target state, so when Fidelity is null the two states are orthogonal while if it is 1 the two states coincides. Fidelity was widely adopted for easiness of computation in discrete and continuous variable system, in fact a computable analytical formula for the quantum fidelity between two arbitrary multimode Gaussian Banchi et al. (2015).

Secondly I question: Does a good quantum thermometer could be build with a system showing phase transition?

Thermometers we employ in daily life are built guaging the temperatures range from two critical points where two phase transition occur in water. I employ a critical magnetic system, known as Lipkin-Meshkov-Glick model, I will study it in contact with a reservoir with it has thermalized but whose temperature is an unknown temperature to be estimated. I will show that the best precision for temperature estimation it is not at critical point as someone could suspect but nevertheless criticality is an unmatchable resource even in the quantum realm.

Last but not least question is: When two different probes spatially separated interact with a common or a separate bath?

It is quite a common opinion in community of open quantum system physics that items, located far away one from each others, feel the effect of different environments. Dissipation and decoherence are the two main processes which a quantum system undergo when its evolution is not unitary, i.e. when it is not isolated, but when it interacts with another system much bigger than itself called alternatively the environment, the heath bath or the reservoir. I will explore how two different systems put in contact with a common bath show decoherence with typical quantum interference leading to a non obvious definition of separate environments.

The present thesis cover some of the plethora of applications that quantum technologies could have. In particular it is structured as follow:

- in chapter 1 we recall the basic definition of the quantum theory and of the estimation theory in quantum mechanics framework, in addition we will introduce some notion typical of the quantum optics formalism;
- in chapter 2 we will debate how fidelity a common measure used to certify quantum features should be employed with caution, using example from continuous variable systems and qubit and eventually we will show how our theoretical evidence is experimentally confirmed;
- in chapter 3 the tools of quantum estimation theory are used to derive a ultra-precise measure of the temperature based on a quantum critical spin system;
- in chapter 4 a microscopic model for the description of the emergence of collective decoherence in extended systems is derived, starting with no phenomenological assumption.

CHAPTER 1

Basic tools of quantum theory

This is an introductory chapter that has an ancillary function for the other chapters of this thesis. In fact here we recall the basic concepts, formalism and tools we will employ in the following. This chapter consists of five sections, in the first we briefly review the postulates of the quantum mechanics, in the second section we outline some relevant distances used to address the distance between two states in the Hilbert space, this section is preparatory for the third one where a sketch of the quantum estimation theory is given. The following section deals with a treatise of operators commonly adopted in Gaussian states quantum optics.

1.1 Potulates of Quantum Mechanics

Quantum Mechanics is based on postulates relating its formal and mathematical structure to the real world

1. Each quantum mechanical system is associated to a vectorial space known as Hilbert space$\mathcal{H}$ and its physical state is described by a vector of that space.

   A Hilbert space $\mathcal{H}$ is a complex vector space, whose elements are denoted in the Dirac notation as $|\psi\rangle$. It has endowed with an inner product $\langle\phi|\ \psi\rangle$ mapping pair of states into c-numbers with the following properties:

   - Positivity: $\langle\psi|\ \psi\rangle \geq 0 \quad \forall\, |\psi\rangle$ and equality holding only for $|\psi\rangle$;
   - Linearity: $\langle\phi|\,(\alpha\,|\psi_1\rangle + \beta\,|\psi_2\rangle) = \alpha\,\langle\phi|\ \psi_1\rangle + \beta\,\langle\phi|\ \psi_2\rangle$;
   - Skew symmetry: $\langle\phi|\ \psi\rangle = \langle\psi|\ \phi\rangle^*$;
   - Metric: $||\psi||^2 = \langle\phi|\ \psi\rangle$ the square root of the norm induce an euclidean distance among vectors.

2. Each physical quantities that could, in principle, be measured is associated with an hermitean operator acting on the Hilbert space. An hermitean, or self-adjoint, operator $\hat{A}$ on a Hilbert space $\mathcal{H}$ is a linear operator $\mathcal{H} \to \mathcal{H}$ which satisfies

   $$\langle y|\ Ax\rangle = \langle Ay|\ x\rangle \quad \text{for} \quad x, y \in \mathcal{H} \tag{1.1}$$

   Any self-adjoint operator has a spectral decomposition in terms of its eigenvalues λ_j, i.e. $\hat{A} = \sum_j \lambda_j |e_j\rangle\langle e_j|$ where $|e_j\rangle\langle e_j| = P_j$ are a set of orthonormal projectors definied by:

   $$P_j P_k = \delta_j k P_j \tag{1.2}$$

   $$P_j^\dagger = P_j \tag{1.3}$$

In particular a system is described by a statistical operator, usally referred to as density matrix, ϱ, that could be always written in the form

$$\varrho = \sum_j \mu_j |u_j\rangle\langle u_j| \tag{1.4}$$

where the set of all $|u_j\rangle$ is a basis of the Hilbert space and their coefficients μ_j are the probabilities to find the state in $|u_j\rangle$ such that $\mu_j > 0$ and $\sum_j \mu_j = 1$.

3. The probability of obtaining the outcome λ_j from the measurement of the observable A is given by $|\langle\psi|\ u_j\rangle|^2$ or explicity by

$$p(\lambda_j) = \langle\psi| P_j |\psi\rangle = \sum_k \langle u_k|\ \psi\rangle \langle\psi| P_j |u_k\rangle \tag{1.5}$$

The state just after a measurement is an eigenstate of the measured operator and it is

$$|\psi_j\rangle = \frac{P_j |\psi\rangle}{p(\lambda_j)} \tag{1.6}$$

4. The operator governing the states' time evolution is unitary and it is defined as:

$$|\psi(t)\rangle = U_t |\psi\rangle = e^{-iHt} |\psi\rangle \tag{1.7}$$

and it is the formal solution of the dynamical equation for a quantum state, the Schrodinger equation

$$\frac{d}{dt}|\psi(t)\rangle = -iH|\psi(t)\rangle. \tag{1.8}$$

where H is the system Hamiltonian the hermitian operator related to the observable energy.

The states we have considered until now have the peculiarity to be pure, in other words they are systems without interaction with an external extended environment. Although closed systems are a good description of some well controllable experimental situations, the real word seems to be a little bit more messy. A quantum state is never separated from its surrounding environment, this evidence leads to a different mathematical description of the quantum states. In order to accomplish this task we should introduce the formalism of the density operator, which accounts of an additional degree of ignorance we have on the system. The ignorance is about the way the state has been prepared; given an ensemble of pure states $|\psi_i\rangle$ they can recur with classical probabilities p_i. Throughout the set $\{p_i, |\psi_i\rangle\}$ and imposing the self-adjointness, the positivity and the unitary of the operator we define the density matrix:

$$\varrho = \sum_i p_i |\psi_i\rangle\langle\psi_i| \tag{1.9}$$

which recovers the close system dynamics when all p_i are null except for one.

The equation describing time evolution of the density matrix is analogue to Eq.(1.8) and it is

$$i\frac{\partial\varrho(t)}{\partial t} = [H, \varrho(t)] \tag{1.10}$$

whose solution is

$$\varrho(t) = e^{-iHt}\varrho_0 e^{iHt} \tag{1.11}$$

1.2 Distances in the Hilbert space

We have stated before that states live in Hilbert space. When dealing with vector space a distance inducing a norm is necessary to prove if it is also a metric space. The above space is endowed with different distances inducing a metric, we recall here some of those widely adopted in quantum information and we will employ in the next chapters . A distance $\mathcal{D}(\varrho_1,\varrho_2)$ between two density matrices ϱ_1 and ϱ_2 of any kind has to satisfy the following properties:

- has to be positive semi-definite

$$\mathcal{D}(\varrho_1,\varrho_2) \geq 0 \qquad \forall \varrho_1,\varrho_2 \tag{1.12}$$
$$\mathcal{D}(\varrho_1,\varrho_2) = 0 \qquad \varrho_1 = \varrho_2 \tag{1.13}$$
$$\tag{1.14}$$

- has to be symmetric

$$\mathcal{D}(\varrho_1,\varrho_2) = \mathcal{D}(\varrho_2,\varrho_1) \tag{1.15}$$

- satisfies the triangular inequality

$$\mathcal{D}(\varrho_1,\varrho_2) \leq \mathcal{D}(\varrho_1,\varrho) + \mathcal{D}(\varrho,\varrho_2) \tag{1.16}$$

1.2.1 Trace distance

Any L_p norm of an operator defined has

$$||A||_p = \left(\frac{1}{2}\mathrm{Tr}|A|^p\right)^{1/p} \tag{1.17}$$

naturally induces a distance of the form

$$\mathcal{D}(\varrho_1,\varrho_2)_p \propto ||(\varrho_1-\varrho_2)||_p.$$

For $p = 2$ the L_p distance is Euclidean and it is known as Hilbert-Schimtd distance. While when $p = 1$ we have the trace distance that is related to the average probability of success when trying to distinguish with a projective measurement two different states.

$$\mathcal{D}_{\mathrm{Tr}}(\varrho_1,\varrho_2) = \frac{1}{2}|(\varrho_1-\varrho_2)| = \frac{1}{2}\mathrm{Tr}(\varrho_1-\varrho_2) \tag{1.18}$$

where the trace norm is defined as

$$|A| = \mathrm{Tr}|A| = \mathrm{Tr}[\sqrt{A^\dagger A}]. \tag{1.19}$$

It can be proved following the definition and the three characterizing properties that the trace distance is bounded in the interval $[0,1]$

$$0 \leq \mathcal{D}_{\mathrm{Tr}}(\varrho_1,\varrho_2) \leq 1 \tag{1.20}$$

it is 0 for orthogonal states and it is 1 when the two states coincide. Finally it is subadditive under tensor product:

$$\mathcal{D}_{\mathrm{Tr}}(\varrho_1\otimes\sigma_1,\varrho_2\otimes\sigma_2) \leq \mathcal{D}_{\mathrm{Tr}}(\varrho_1,\varrho_2) + \mathcal{D}_{\mathrm{Tr}}(\sigma_1,\sigma_2). \tag{1.21}$$

1.2.2 Fidelity

We introduce here the Uhlmann fidelity between two quantum mixed states. It is not a proper distance in the Hilbert space but it will useful when dealing with that induced by the Bures metric. Fidelity was introduced in Uhlmann (1976) as a quantifiers of the transition amplitude in the state space of a C^*-algebras, although its ready-to-use definition for quantum information purposes appeared in Jozsa (1994). Hence fidelity is defined as

$$F(\varrho_1, \varrho_2) = \left(\mathrm{Tr} \left[\sqrt{\sqrt{\varrho}_1 \varrho_1 \sqrt{\varrho_1}} \right] \right)^2 \tag{1.22}$$

It is worth noting that fidelity can be proved to be symmetric for states swapping, non-negative, continuos and a concave function of both the arguments: ϱ_1 and ϱ_2. Fidelity, it is easy to check, reduce to the overlap between the states when they are pure $\varrho_1 = |\psi_1\rangle\langle\psi_1|$ and $\varrho_2 = |\psi_2\rangle\langle\psi_2|$

$$\begin{aligned} F(|\psi_1\rangle, |\psi_2\rangle) &= \left(\mathrm{Tr} \left[\sqrt{|\psi_1\rangle\langle\psi_1|\psi_2|\psi_1\rangle\langle\psi_1|)} \right] \right)^2 \\ &= |\langle\psi_1|\psi_2\rangle|^2 \mathrm{Tr}[\sqrt{|\psi_1\rangle\langle\psi_1|}]^2 \\ &= |\langle\psi_1|\psi_2\rangle|^2. \end{aligned} \tag{1.23}$$

The overlap between two pure states has a geometric interpretation in terms of an angle between them and this allows to define the Fubini-Study distances

$$\mathcal{D}_{FS}(|\psi_1\rangle, |\psi_2\rangle) = \cos^{-1} \sqrt{|\langle\psi_1|\psi_2\rangle|^2}. \tag{1.24}$$

1.2.3 Bures distance

An extension of the Fubini-Study distance to mixed states is obviously given in terms of fidelity and it is referred to be the Bures angle (or lenght)

$$\mathcal{D}_A(\varrho_1, \varrho_2) = \cos^{-1} \sqrt{F(\varrho_1, \varrho_2)}. \tag{1.25}$$

This allows us to construct a distance linked to the statistical distinguishability of two arbitrary mixed states. We begin considering a mixed state ϱ belonging to an Hilbert space $\mathcal{H}_1$, it is possible to purificate it letting it live in a bigger space $\mathcal{H}_1 \otimes \mathcal{H}_2$. A purification of ϱ is any pure state $|\psi\rangle$ having the mixed state as marginal, such that

$$\varrho = \mathrm{Tr}_2[|\psi\rangle\langle\psi|].$$

This allows us to restate Eq.(1.22)

$$F(\varrho_1, \varrho_2) = \max |\, \langle\psi_1|\, |\psi_2\rangle \,|$$

where the maximum is taken over all the purification $|\psi_1\rangle$ and $|\psi_2\rangle$ of ϱ_1 and ϱ_2 respectively. If we think a pure states, they lose coherence when in contact with their own environment becoming mixed states. In this framework, when no information about the correlation between systems and each own environment is accessible, fidelity gives a measure of how much probable is to distinguish the two states. Therefore by minimizing the distance between all the purification of ϱ_1 and ϱ_2 constrained by the condition

imposed by the parallel transport of two rays in the Hilbert space it is possible to write:

$$\begin{aligned}\mathcal{D}_B(\varrho_1,\varrho_2) &= \sqrt{2(1-Tr[\sqrt{\sqrt{\varrho}_1\varrho_2\sqrt{\varrho}_1}])} \\ &= \sqrt{2\left(1-\sqrt{F(\varrho_1,\varrho_2)}\right)}.\end{aligned} \tag{1.26}$$

It is interesting to note that this distance is either Reimannian and monotone, in contrast with the trace distance that is only monotone and with the Hilbert-Schmidt one is Riemannian only. This allow to have a well defined infinitesimal version of the Bures metric:

$$ds_B^2 = \mathcal{D}_B^2(\varrho,\varrho+d\varrho) = \mathrm{Tr}G^2\varrho = \frac{1}{2}TrGd\varrho \tag{1.27}$$

where we have introduced the symmetric derivative operator G

$$d\varrho = G\varrho + \varrho G. \tag{1.28}$$

The Bures metric In the following paragraph we will derive the Bures distances between two density matrix $\varrho_1 = \varrho$ and $\varrho_2 = \varrho + d\varrho$, following the strategy adopted in Sommers & Zyczkowski (2003). Firstly we write the operator whose trace should be computed in the fidelity definition as

$$\sqrt{\varrho_1^{1/2}\varrho_2\varrho_1^{1/2}} = \sqrt{\varrho^{1/2}(\varrho+d\varrho)\varrho^{1/2}} = \varrho + X + Y \tag{1.29}$$

where the matrix X is of the first order in $d\varrho$, while Y is of second order. Upon squaring both sides and forgetting terms upper to the second order in $d\varrho$

$$\varrho^2 + \varrho^{1/2}d\varrho\varrho^{1/2} \simeq \varrho^2 + X^2 + \varrho^X + X\varrho + \varrho^Y + Y\varrho \tag{1.30}$$

we hence have

$$\varrho^{1/2}d\varrho\varrho^{1/2} = X\varrho + \varrho X \qquad \text{1st order} \tag{1.31}$$

$$-X^2 = Y\varrho + \varrho Y \qquad \text{2nd order} \tag{1.32}$$

or in the diagonal basis $\varrho = \sum_\mu p_\mu|\mu\rangle\langle\mu|$

$$X_{\nu,\mu} = d\varrho_{\nu,\mu}\frac{p^{1/2_\nu}p^{1/2_\mu}}{p_\nu + p_\mu} \tag{1.33}$$

$$Y_{\nu,\mu} = -\frac{(X^2)_{\nu,\mu}}{p_\nu + p_\mu} \tag{1.34}$$

Since $\mathrm{Tr}[\varrho] = 1$, hence $\mathrm{Tr}[d\varrho] = 0$ and $\mathrm{Tr}X = \mathrm{Tr}[d\varrho/2] = 0$, while

$$\mathrm{Tr}Y = -\sum_{\nu,\mu}\frac{1}{2p_n}|X_{\nu,\mu}|^2 = -\sum_{\nu,\mu}\frac{|d\varrho_{\nu,\mu}|^2}{4(p_\nu+p_\mu)} \tag{1.35}$$

let us derive the results of Hubner in for the Bures metric:

$$ds_B^2 = \mathcal{D}_B(\varrho,\varrho+d\varrho))^2 = \frac{1}{2}\sum_{\nu,\mu}\frac{|d\varrho_{\nu,\mu}|^2}{p_\nu+p_\mu} = \frac{1}{2}\sum_{\nu,\mu}\frac{|\langle\nu|d\varrho|\mu\rangle|^2}{p_\mu+p_\nu}. \tag{1.36}$$

Let us now write the infinitesimal variation of the density matrix in the diagonal basis of ϱ

$$d\varrho = \sum_{\mu} d(p_\mu|\mu\rangle\langle\mu|) = \sum_{\mu} dp_\mu|\mu\rangle\langle\mu| + p_\mu|d\mu\rangle\langle\mu| + p_\mu|\mu\rangle\langle d\mu| \tag{1.37}$$

Projetting it onto $|\nu\rangle$ and using the orthogonality of the eigenvectors

$$\langle\nu|\, d\varrho\, |\nu\rangle = \delta_{\mu,\nu} dp_\mu + (dp_\mu - dp_\nu)\, \langle\nu|\, d\mu\rangle \tag{1.38}$$

obtaining

$$ds_B^2 = \frac{1}{4}\sum_{\nu} \frac{dp_\nu^2}{p_\nu} + \frac{1}{2}\sum_{\nu\neq\mu} \frac{(p_\mu - p_\nu)^2}{p_\nu + p_\mu} |\langle\nu|dm\rangle|^2. \tag{1.39}$$

The last expression can be interpreted as a sum of two different terms: a classical contribution linked to the statical distinguishability of two probability distribution and a purely quantum contribution. With impunity we can infere that when two density matrix are diagonal in the same basis, the problem of computing the distance between them is amenable to the study of Fisher-Rao metric of the classical probability theory.

1.3 Quantum Estimation Theory

In this section we introduce Quantum Estimation Theory (QET) and the theoretical tools it provides to evaluate bounds to the precision of an estimation process in a Quantum Mechanics.

The intrinsic probabilistic nature of quantum mechanics arises when performing a measurement of an observable $\hat{A}$ on the considered system, in fact it is not possible to predict with certainty the result even if it is in a known state. Nevertheless if multiple measures are performed on several copies of the same system, i.e. in the same quantum state, the results will follow a probability distribution known $a\ priori$. Without lost of generality we can assume $\hat{A} = \Pi_x$ being one item of a POVM so it is possible to derive such a distribution by mean of the Burn rule:

$$p(A, x) = \mathrm{Tr}[\Pi_x \varrho], \tag{1.40}$$

where x is the measurement output.

It is common in physics to not have direct access to some physical quantities, so the strategy is to measure some variable and then estimate the quantity of interest with with the minimum error. When dealing with quantum systems we may imagine a situation in which its state is known unless for a parameter λ. For example we could have a system with a known Hamiltonian in thermal equilibrium with a reservoir at unknown temperature $1/\beta$, so the corresponding state describing this system is known to be the canonical distribustion $\varrho_\beta = \exp(-\beta H)/Z$. A formal description of this situation is to consider a map $\lambda \to \varrho_\lambda$ associating to each parameter's value a quantum state. In this framework measuring an observable $\hat{A}$ yields a probability distribution $p(A, x, \lambda)$. The estimation of λ then turns into the problem of inferring from a known set of data the best value for the parameter.

1.3.1 Classical Estimation Theory

Consider a random variable X assuming values in a sample space Ω, which could be for example the real axis or a vector of n elements, and imagine to use a parameter λ to

label some normalized measures, with probability density functions $p(x,\lambda)$, on Ω. An estimator for the parameter λ is a random variable that depends on the sample information; its value provides approximations of this unknown parameter. While a specific value of that random variable is called an estimate. In searching for an estimator, some properties are required

1. Unbiasedness

$$E[\hat{\lambda}-\lambda]_\lambda = \int_\Omega \mathrm{dx}\, p(x,\lambda)(\hat{\lambda}(x)-\lambda) = 0 \qquad \forall\lambda, \tag{1.41}$$

2. Efficiency

$$\mathrm{Var}(\lambda,\hat{\lambda}) := E[(\hat{\lambda}-\lambda)^2]_\lambda. \tag{1.42}$$

where $E[.]_\lambda$ denotes the mean with respect to the probability distribution $p(x,\lambda)$, if Ω is a finite set then the integral is substituted with a sum.

A lower bound for the variance of any estimator is given by the Cramer-Rao inequality

$$\mathrm{Var}(\lambda,\hat{\lambda}) \geq \frac{1}{F(\lambda)}, \tag{1.43}$$

where $F(\lambda)$ is the Fisher Information (FI) given by

$$F(\lambda) = E\left[\frac{\partial \ln(p_i(X_i,\lambda))}{\partial\lambda}\right]_\lambda \tag{1.44}$$

$$= \int_\Omega dx\; p(x,\lambda)\left(\frac{\partial \ln(p(x,\lambda))}{\partial\lambda}\right)^2$$

$$= \int_\Omega dx\; \frac{1}{p(x,\lambda)}\left(\frac{\partial p(x,\lambda)}{\partial\lambda}\right)^2. \tag{1.45}$$

To prove the Cramer-Rao bound let us consider two arbitrary function $f_1(x)$ and $f_2(x)$ and note that their average according to a probability distribution $p(x,\lambda)$

$$\langle f1, f2\rangle = \int dx p(x|\lambda) f1(x) f2(x) \tag{1.46}$$

could be seen as a scalar product in the function space. Choosing opportunely $f_1(x) = \hat{\lambda}-\lambda$ and $f_2(x) = \partial_\lambda \ln p(x,\lambda)$ we have

$$\begin{aligned} |f1|^2 &= \mathrm{Var}(\lambda) \\ |f2|^2 &= F(\lambda) \\ \langle f1, f2\rangle &= 1 \end{aligned} \tag{1.47}$$

hence the Fisher information when just one measurement is performed would reduce to the Cauchy-Schwartz inequality. While when considering M measurements and they are described by the random variables $x_1, x_2, ..., x_M$ the corresponding probability distribution function are independent too and it is possible to write

$$\begin{aligned} F_M(\lambda) &= \int dx_1 \ldots dx_M\; p(x_1,x_2,...,x_M|\lambda)[\partial_\lambda \ln p(x_1,x_2,...,x_M|\lambda)]^2 \\ &= M\int dx p(x|\lambda)[\partial_\lambda \ln p(x|\lambda)]^2 = MF(\lambda). \end{aligned} \tag{1.48}$$

A point remains to be clarified: how to construct an estimator able to saturate always the bound, at least in the asymptotic limit ($M >> 1$). In order to give an answer let us construct the probability distribution function of a set of M independent variable, i.e. the variable describing a random sample of M measurements outputs:

$$\mathcal{L}(x_1, x_2, ..., x_M|\lambda) = \prod_{k=1}^{M} p(x_k|\lambda). \tag{1.49}$$

The above function is called the likelihood function and it is clear it is the joint probability of the given data sample. A maximum-likelihood estimator for the unknown parameter is defined as the quantity that minimizes $\mathcal{L}(\{x_k\}, \lambda)$ and it is a function of all the random variables, namely $\lambda_{ml} = \lambda_{ml}(\{x_k\})$. Therefore the optimization problem to be solved is

$$\frac{\partial \mathcal{L}(\lambda)}{\partial \lambda} = 0; \qquad \frac{\partial^2 \mathcal{L}(\lambda)}{\partial \lambda^2} < 0. \tag{1.50}$$

Why this method is called maximum-likelihood is naive and intuitive, in fact it is based on the evidence that the observed sample have been observed because its probability was larger than any other samples. Thus the value of the parameter maximizing the likelihood function is that generating the sample. The resolving strategy starts noting that it would be more convenient to deal with the log-likelihood function , since $\mathcal{L}(\lambda)$ is positive and a product of function

$$L(\lambda) = \log \mathcal{L}(\lambda) = \sum_{k=1}^{M} log p(x_k|\lambda).$$

The variance of the max-likelihood estimator is finally given by

$$\mathrm{Var}(\lambda_{ml}) = \int [\prod_k dx_k \, p(x_k|\lambda)][\lambda_{ml}(\{x_k\}) - \lambda]^2, \tag{1.51}$$

which in the large M limit saturates the Cramer-Rao bound.

As stated above the probability distributions arises naturally in the context of the quantum mechanics as probability of measurement results, thus the equation rewrites substituting Eq.(1.40),

$$F(\hat{A}, \lambda) = \int_\Omega dx \, \frac{1}{\mathrm{Tr}[P_x \varrho_\lambda]} \frac{\partial \mathrm{Tr}[P_x \varrho_\lambda]}{\partial \lambda}^2. \tag{1.52}$$

therefore an estimator becomes a function of the eigenvalues of the measured observable. Alongside it is worth noting that a not to subtle difference, in fact the measurement outcome is crucial feature in the quantum context and it is quite different from a classical random variable.

Any experimental setup does not perform a single measurement but gather several measurement outputs, ideally from identical and independent replies of the experiment performed on replicas of the same state hence they are analyzed. Formally this mean that the random variable is vector valued, $X = (X_1, \ldots, X_n)$, and that the joint distribution is factorized

$$p(X = (x_1, \ldots, x_n); \lambda) = \prod_{i=1}^{n} p_i(X_i = x_i; \lambda).$$

Not surprisingly, the Fisher Information turns to be an addictive quantity

$$F(\lambda) = E_\lambda \left[\frac{\partial \ln(p(X,\lambda))}{\partial \lambda} \right] = \sum_{i=1}^{n} E_{\lambda,i} \left[\frac{\partial \ln(p(X_i,\lambda))}{\partial \lambda} \right] = \sum_{i=1}^{n} F(\lambda)_i, \tag{1.53}$$

where we used that

$$E_{\lambda,i} \left[\frac{\partial \ln(p_i(X_i,\lambda))}{\partial \lambda} \right] = 0 \qquad \forall i. \tag{1.54}$$

An estimator achieving the Cramer-Rao bound is said to be efficient.

Although it is not always possible to find an efficient estimator, generally exist estimators unbiased and $asimptotically$ efficient, i.e. in the limit of large replicas they deviate from Cramer-Rao bound infinitesimally. Among those estimators there are maximum likelyhood estimators, that employ the maximum likelyhood principle, and Bayesian estimators.

For further reference on classical estimation theory see, for example, Neyman (1937).

1.3.2 Quantum Cramer-Rao bound

For whom it concerns the estimation theory, we simply note that it is clear from Eq.(1.52) that different observables give rise to different FIs and hence to different optimal precisions for the estimate of λ. A question thus arises on whether it is possible to find an upper bound for these FIs, which corresponds to an optimal measurement. It turns out that this is possible, and such maximum FI is known as Quantum Fisher Information.

In order to obtain an expression for the Quantum Fisher Information it is necessary to introduce the symmetric logarithmic derivative (SLD). This is the operator L_λ solving

$$\frac{L_\lambda \varrho_\lambda + \varrho_\lambda L_\lambda}{2} = \frac{\partial \varrho_\lambda}{\partial \lambda}. \tag{1.55}$$

SLD allow us to rewrite the derivative of ϱ_λ in a more comfortable way so that Eq.(1.45) becomes

$$F(\hat{A},\lambda) = \int dx \, \frac{\mathrm{Re}(\mathrm{Tr}[\varrho_\lambda P_x L_\lambda])^2}{\mathrm{Tr}[\varrho_\lambda P_x L_\lambda]} \tag{1.56}$$

It is possible to evaluate an upper bound for such expression :

$$\begin{aligned}
F(\lambda) &= \int dx \, \frac{\mathrm{Re}(\mathrm{Tr}[\varrho_\lambda P_x L_\lambda])^2}{\mathrm{Tr}[\varrho_\lambda P_x L_\lambda]} \\
&\leq \int dx \, \left| \frac{\mathrm{Tr}[\varrho_\lambda P_x L_\lambda]}{\sqrt{\mathrm{Tr}[\varrho_\lambda P_x L_\lambda]}} \right|^2 \\
&= \int dx \, \left| \mathrm{Tr} \left[\frac{\sqrt{\varrho_\lambda}\sqrt{P_x}}{\sqrt{\mathrm{Tr}[\varrho_\lambda P_x]}} \sqrt{P_x} L_\lambda \sqrt{\varrho_\lambda} \right] \right|^2 \\
&\leq \int dx \, \mathrm{Tr}[P_x L_\lambda \varrho_\lambda L_\lambda] \\
&= \mathrm{Tr}[\varrho_\lambda L_\lambda^2]
\end{aligned}$$

In order to provide an optimal estimator, one has first to find the observable A for which the $F(A,\lambda)$ is equal to $G(\lambda)$ and eventually saturate the classical Cramer-Rao constructing an optimal classical estimator as explained before.

In order to achieve the optimization over the possible observables the two inequalities in Eq.(1.57) must be saturated. The first inequality simply requires the trace to be real, the second inequality is a Cauchy-Schwartz inequality for the inner product $(A,B) := \mathrm{Tr}[A^\dagger B]$ where $A^\dagger = \frac{\sqrt{\varrho_\lambda}\sqrt{P_x}}{\sqrt{\mathrm{Tr}[\varrho_\lambda P_x]}}$ and $B = \sqrt{P_x}L_\lambda\sqrt{\varrho_\lambda}$. This becomes an equality when A and B are proportional, i.e. when the following holds

$$\frac{\sqrt{P_x}\sqrt{\varrho_\lambda}}{\sqrt{\mathrm{Tr}[\varrho_\lambda P_x]}} = \frac{\sqrt{P_x}L_\lambda\sqrt{\varrho_\lambda}}{\sqrt{\mathrm{Tr}[\varrho_\lambda \Pi_x L_\lambda]}} \qquad \forall\lambda. \tag{1.57}$$

Therefore the Quantum Fisher Information $G(\lambda)$ bounds the Fisher information and

$$F(\lambda) \leq G(\lambda) \equiv \mathrm{Tr}[\varrho_\lambda L^{2_\lambda}] = \mathrm{Tr}[\partial_\lambda \varrho_\lambda L_\lambda] \tag{1.58}$$

we have a more stringent condition on the variance of the estimator of a quantum parameter, the quantum Cramer-Rao bound:

$$\mathrm{Var}(\lambda) \geq \frac{1}{MG(\lambda)}. \tag{1.59}$$

The last equation is true if and only if the set of all P_x is the set of projection operators on the eigenspaces spanned by L_λ, so that the optimal measurement is that associated to the any observable diagonal in the same basis of the SLD. It is convenient to do two consideration about the role of the SLD, first having found in it the optimal measure to be performed does not mean that we have found the estimator yet: we now are in the same situation as in the classical estimation theory where an estimator actually achieving the Cramer-Rao bound is to be found. What we have done until now is to overcome a difficulty that in classical estimation it is not present, viz. the fact that measurements could not be commuting and therefore one has first to choose an observable to measure and then to choose the classical random variable, a function of the eigenvalues of the observable, to be statistically processed. Secondly, it appears that the knowledge of the true λ value is necessary to design the optimal measure to estimate it. This is a sort of logical loop and it is is usually solved by implementing an adaptative strategy; a guess is made about the true value of λ then relative optimal measure then a preliminary data analysis is performed, therefore the λ obtained is used to construct a new optimal measure, iterating this process until the best estimator is found. An optimal quantum estimator is given by

$$O_\lambda = \lambda\mathbb{I} + \frac{L_\lambda}{G(\lambda)} \tag{1.60}$$

for which indeed we have

$$Tr[\varrho_\lambda O_\lambda] = \lambda, \quad \mathrm{Tr}[\varrho_\lambda O^2] = \lambda^2 + \frac{\mathrm{Tr}[\varrho_\lambda L_\lambda^2]}{G_\lambda^2} \tag{1.61}$$

and thus

$$\langle \Delta O_\lambda^2 \rangle = \frac{1}{G(\lambda)}. \tag{1.62}$$

Let us now focus on how obtain an explicit form for both the SLD and the Quantum Fisher Information . First one has to solve equation (1.55) defining the Symmetric Logaritmic Derivative, known as Lyapunov matrix equation,

$$L_\lambda = \int_0^\infty dt \exp(-\varrho_\lambda)\partial_\lambda \varrho_\lambda \exp(-\varrho_\lambda), \tag{1.63}$$

whose solution, writing $\varrho_\lambda = \sum_n p_n(\lambda)|\psi_n(\lambda)\rangle\langle\psi_n(\lambda)|$ in its basis reads

$$L_\lambda = 2\sum_{nm} \frac{\langle\psi_n|\partial_\lambda \varrho_\lambda|\psi_m\rangle}{p_n + p_m}|\psi_n\rangle\langle\psi_m|. \tag{1.64}$$

And hence Quantum Fisher Information rewrites

$$G(\lambda) = 2\sum_{nm} \frac{|\langle\psi_n|\partial_\lambda \varrho_\lambda|\psi_m\rangle|^2}{p_n + p_m}, \tag{1.65}$$

with the sum carried over those indexes for which $p_n + p_m \neq 0$ or in a basis independent form

$$G(\lambda) = \int_0^\infty dt\, \mathrm{Tr}\left[\partial_\lambda \varrho_\lambda \exp\{-\varrho_t\}\partial_\lambda \varrho_\lambda \exp\{-\varrho_\lambda t\}\right]. \tag{1.66}$$

Rewriting $\partial_\lambda \varrho_\lambda$ in terms of eigenvectors and eigenvalues of ϱ_λ,

$$\partial_\lambda \varrho_\lambda = \sum_n \partial_\lambda p_n|\psi_n\rangle\langle\psi_n| + p_n|\partial_\lambda\psi_n\rangle\langle\psi_n| + p_n|\psi_n\rangle\langle\partial_\lambda\psi_n|, \tag{1.67}$$

Eq.(1.65) for the Quantum Fisher Information assume the following form

$$G(\lambda) = \sum_n \frac{(\partial_\lambda p_n(\lambda))^2}{p_n(\lambda)} + 2\sum_{nm} \sigma_{nm}|\langle\psi_n(\lambda)|\partial_\lambda\psi_m(\lambda)\rangle|^2, \tag{1.68}$$

with

$$\sigma_{nm} = \frac{(p_n - p_m)^2}{p_n + p_m}. \tag{1.69}$$

It is worth specifying the two contributions to the final form of the Eq.(1.68). The first sum is dependent just on the eigenvalues of ϱ_λ, i.e. on the classical mixture character of density matrix ϱ_λ, whilst the second term depends on the eigenvectors so it contains the genuine quantum contribution to Quantum Fisher Information , in the sense that when the states are pure and ϱ_λ is a projector its eigenvalues are λ-independent, and the second sum is the only term contributing to the Quantum Fisher Information . The two terms are usually referred to as the *classical* and the *quantum* contribution to the Quantum Fisher Information , respectively. For further reference on quantum estimation theory see, for example, Paris (2009). Finally we can obtain also an expression for an optimal observable

$$O_\lambda = \sum_p (\lambda + \frac{\partial_\lambda \varrho_p}{\varrho_p})|\psi_p\rangle\langle\psi_p| + \frac{2}{G(\lambda)}\sum_{n\neq m} \frac{\varrho_n - \varrho_m}{\varrho_n + \varrho_m}\langle\psi_m|\partial_\lambda\psi_{n\rangle}|\psi_{m\rangle\langle\psi_n}|. \tag{1.70}$$

1.4 Quantum Estimation theory and Geometry of quantum states

The Fisher information arises in statistics when treating the problem of estimating parameters but interestingly such quantities emerge in a very natural way applying tools from differential geometry to statistical mechanics.

In Brody & Hughston (1996) the authors show how Fisher Information emerges as a Riemannian metric over the classical probability distribution describing the microscopic states They procede in the following way: let consider a space (X,Σ), with space of events X, σ-algebra Σ and a normalized positive measures μ, which under some hypotheses this measure may be written as integral of a function with respect to a fixed measure $d\nu$:

$$\mu(B) = \int_B f_\mu d\nu \quad \forall B \in \Sigma \tag{1.71}$$

As μ is positive so will be f_μ, at least almost everywhere with respect to the measure ν in B, and this allows to define an injective map between measures and the unit sphere S^1 of $L^2(X, \Sigma, \nu)$ of $real$ square modulus summable functions, defined by

$$\Phi(\mu) = \sqrt{f_\mu}. \tag{1.72}$$

The unit sphere is furnished with a Riemaniann metric inherited from the inner product of the Hilbert Space that we will call g.
Consider now a smooth manifold M of parameters together with a map $\Psi : M \to \mu$, the map $\Theta = \Phi \circ \Psi$ allows to obtain Riemannian metric for M defined as

$$i_{\theta_0}(v, w) = g(d\Theta\, v, d\Theta\, w) \quad \forall v, w \in T_{\theta_0} M. \tag{1.73}$$

The matrix elements $i_r s$ could be expressed, after some algebra, by

$$(i_{\theta_0})_{rs} = \int \left[\frac{\partial \ln(p(x,\theta))}{\theta^r} \frac{\partial \ln(p(x,\theta))}{\theta^s} \right]_{\theta=\theta_0} p(x,\theta) d\nu, \tag{1.74}$$

where by $p(x, \theta)$ we mean the function $\Theta(\theta)^2$. Eq(1.74) is exactly the matrix element for the multi-parametric Fisher Information (a general case we did not mentioned above).

In order to clarify what we have considered untill now, let us consider the situation in which the sample space X is composed by a finite number of items n, the algebra Σ is given by the subsets of X and measures are vectors $(p_1, \ldots, p_n)$ such that

$$\sum_{i=1}^{n} p_i = 1 \qquad p_i \geq 0 \quad \forall i. \tag{1.75}$$

Geometrically this is the condition describing the n $simplex$ in the $\mathbb{R}^n$ vector space, and it could be thought as a manifold with coordinates p_i. Now consider the positive octant of the unit hypersphere, i.e. the set of vectors $(x_1, \ldots, x_n)$ satisfying

$$\sum_{i=1}^{n} x_i^2 = 1 \qquad x_i \geq 0 \quad \forall i, \tag{1.76}$$

this set may be seen as a manifold as well, and it is given a Riemannian metric that, in the coordinate x_i assume the form

$$g(\frac{\partial}{\partial x_i}|_{x_i}, \frac{\partial}{\partial x_j}|_{x_j}) = \delta_{ij}. \tag{1.77}$$

From eq.s (1.75,1.76) it is natural to consider the map ϕ from positive part of the unit hypersphere to the simplex given by $\phi((x_1,\ldots,x_n)) = (x_1^2,\ldots,x_n^2)$, this map is analogue to the one of Eq.(1.72). The differential of ϕ yields a map between the tangent spaces given by $d\phi(\frac{\partial}{\partial x_i}|_{x_i}) = 2x_i\frac{\partial}{\partial p_i}|_{p_i}$. Eventually $d\phi$ induces a metric $\hat{g}$ from g in the simplex, given by

$$\hat{g}(\frac{\partial}{\partial p_i}|_{p_i}, \frac{\partial}{\partial p_j}|_{p_j}) = \frac{\delta_{ij}}{p_i}. \tag{1.78}$$

The latter allows to write an infinitesimal distance on the simplex given by

$$ds^2 = \sum_{i<j}\hat{g}_{ij}dp_i dp_j = \frac{1}{4}\sum_i \frac{dp_i^2}{p_i} \tag{1.79}$$

As a last step we may consider a sub-manifold of the simplex, whose coordinates are θ_a that induce on it a metric tensor F_{ab}, in the same way as we induced the metric for the simplex, obtaining

$$F_{ab} = \frac{1}{4}\sum_i \frac{\partial_a p_i \partial_b p_i}{p_i}, \tag{1.80}$$

that is the Fisher information matrix.

In Venuti & Zanardi (2007) the authors consider the quantum scenario and the mapping Φ is obviously into quantum states described by densty matrix, i.e. into the projective space of a proper complex Hilbert space, $\mathcal{PH}$.

Analogously to the real case, a Riemannian metric may be induced into PH (actually one induces a complex tensor whose real part is a proper metric), such metric is known as Bures or Fubini-Study metric. If a parameter manifold M is embedded into PH by a map $\Phi : M \to \mathcal{PH}$, pulling back the Fubini-Study metric to M one obtains the Quantum Fisher Information matrix.

Possibly, Quantum Fisher Information meaning is more clear when looking at it from the geometrical point of view: Quantum Fisher Information is just the restriction of the most natural concept of infinitesimal distance one is given in the space of quantum states, the one hereditated by the metric in the whole Hilbert space, to the subset of states actually explored by a given system (the map Φ).

Finally, let us note that $\mathcal{PH}$ is equipped with a distance induced by the Riemannian metric mentioned above, the so called Fubini-Study distance, defined by

$$d_{fs}(\psi,\phi) = \cos^{-1}(|\langle\psi,\phi\rangle|) \tag{1.81}$$

Such distance is quite meaningful, in fact it quantifies the distinguishability between two quantum states by mean of any projective measurement. For further reference on the geometrical approach to classical and quantum probability see, for example, Bengtsson & Zyczkowski (2006).

1.5 Relevant operators in quantum optics

We briefly recall in this paragraph some unitary operators that will be extensively used in the following chapters Ferraro et al. (2005).

1.5.1 Continuous variable states

The free hamiltonian of a collection of N free harmonic oscillators of unit mass is, in natural unit $\hbar = c = 1$,

$$H = \frac{1}{2}\sum_{k=1}^{n} = p_k^2 + \omega_k q_k^2 = \sum_{k=1}^{n} \omega_k (a_k^\dagger a_k + \frac{1}{2}) \tag{1.82}$$

where the conjugate position and momentum are linked to bosonic annihilation and creation operators as:

$$q_k = \frac{1}{\sqrt{2\omega_k}}(a_k + a_k^\dagger), \qquad p_k = i\sqrt{\frac{\omega_k}{2}}(a_k - a_k^\dagger) \tag{1.83}$$

that satisfy respectively the commutation relations

$$[q_k, p_j] = i\delta_{kj} \qquad [a_k, a_j^\dagger] = \delta_{kj}. \tag{1.84}$$

Introducing the vector of operators $\mathbf{R} = (q_1, q_2, ..., q_n, p_1, p2, ..., p_n)^T$ the commutation relation become

$$[R_k, R_j] = i\Omega_{kj}\Pi \tag{1.85}$$

where $\Omega_k j$ are the elements of the symplectic matrix

$$\Omega = \bigoplus_{j=1}^{n} \varpi_j, \qquad \varpi = \begin{pmatrix} 0 & 1 \\ -1 & 0 \end{pmatrix}. \tag{1.86}$$

The Hilbert space of a collection of N quantum harmonic oscillators[1] is infinite dimensional, for this reason its correspondingly density matrix should be infinite to in principle. In particular cases, that we will clarify later, a convenient way to treat bosonic states is to give their covariance matrix $\sigma[\varrho]$

$$\sigma_{kj} = \frac{1}{2}\langle\{R_{k,}R_j\}\rangle - \langle R_k\rangle\langle R_j\rangle \tag{1.87}$$

where $\{A, B\} = AB + BA$ is the anticommutator of two operators and $\langle A\rangle = \mathrm{Tr}[\varrho A]$, in particular the expectation values of the R_k are known as first order moment. The positivity of the density matrix combined with the uncertainty relations among the operators imposes a constraint on the covariance matrix

$$\sigma + \frac{i}{2}\mathbf{\Omega} \geq 0, \tag{1.88}$$

We give an example of the covariance matrix of some remarkable states. The first is the vacuum state $|0\rangle$, whose covariance matrix is $\sigma = \frac{1}{2}\mathbb{I}_{2n}$. Another relevant state is that describing the $n-$mode radiation in thermal equilibrium $\nu = \otimes_{k=1}^{n}\nu_k$ where

$$\nu_k = \frac{e^{-\beta a_k^\dagger}}{\mathrm{Tr}[e^{-\beta a_k^\dagger a_k}]} = \frac{1}{n_{kT}+1}\sum_m \left(\frac{n_{kT}}{n_{kT}+1}\right)^m |m\rangle_{kk}\langle m|. \tag{1.89}$$

[1] in this chapter we will assume all the oscillators have the same frequency and we will impose without loss of generality $\omega_k = 1 \quad \forall k$

is the density matrix for a single light mode k, hence

$$\sigma[\nu] = \text{Diag}(n_{1T} + \frac{1}{2}, ..., n_{nT} + \frac{1}{2}) \tag{1.90}$$

While the interaction Hamiltonian among light-modes is of the type

$$H = \sum_{k=1}^{n} g_k^{(1)} a_k^\dagger + \sum_{k>l=1}^{n} g_{kl}^{(2)} a_k^\dagger a_l + \sum_{k,l=1}^{n} g_{kl}^{(3)} a_k^\dagger a_l^\dagger + h.c., \tag{1.91}$$

that it is the sum of three blocks.

1.5.2 Displacement operator

The first block $H \propto g^{(1)} a^\dagger + h.c.$ of 1.91 and the corresponding unitary transformation is the displacement operator that for a collection of n bosons reads

$$D(\boldsymbol{\lambda}) = \otimes_{k=1}^{n} D_k(\boldsymbol{\lambda}_k) \tag{1.92}$$

where $\boldsymbol{\lambda}$ is the column vector $\boldsymbol{\lambda} = (\lambda_1, ..., \lambda_n)^T$ with each $\lambda_k \in \mathbb{C}$ and

$$D_k(\lambda) = \exp\{\lambda_k a_k^\dagger - \lambda_k^* a_k\}) \tag{1.93}$$

is the single-mode displacement operator. This operator owns its name to the action it has in the Heisenberg picture on the annihilation operator, namely

$$D_k^\dagger(\boldsymbol{\lambda}) a_k D_k(\boldsymbol{\lambda}) = a_k + \lambda_k \qquad (k = 1, ..., n) \tag{1.94}$$

In addition the coherent state $|\alpha\rangle$ is generated by acting with the displacement operator on the vacuum state:

$$\begin{aligned} |\alpha\rangle = D(\alpha)\,|0\rangle &= e^{\{\alpha_k a_k^\dagger - \alpha_k^* a_k\}}\,|0\rangle \\ &= e^{-\frac{1}{2}|\alpha|^2} e^{\alpha_k a_k^\dagger} e^{\alpha_k^* a_k}\,|0\rangle \\ &= e^{-\frac{1}{2}|\alpha|^2} \sum_{k=0}^{\infty} \frac{\alpha^k}{\sqrt{k!}}\,|k\rangle \end{aligned} \tag{1.95}$$

where in the third passage we have used the Baker-Hausdorf-Campbell formula.

1.5.3 Squeezing operators

The second block of Eq.(1.91) contains linear terms of the form $g^{(2)} a^\dagger b$ describing the linear mixing of two different modes, such as the interaction of two modes of light in a beam-splitter, but we do not report the corresponding transformation. While the third building block of Eq.(1.91) containins quadratic terms $g^{(2)} {a^\dagger}^2$ or $g^{(2)} a^\dagger b^\dagger$ and describes the single or two mode squeezing. The single mode squeezing transformation is

$$S(\xi) = \exp \frac{1}{2}\xi (a^\dagger)^2 - \frac{1}{2}\xi^* a^2 \tag{1.96}$$

and generates the following mode evolution

$$\begin{aligned} S^\dagger(\xi) a S(\xi) &= \mu a + \mu^\dagger, \\ S^\dagger(\xi) a^\dagger S(\xi) &= \mu^\dagger + \nu^* a \end{aligned} \tag{1.97}$$

where $\xi = re^{i\psi}$, $\mu = \cosh r$ and $\nu = e^{i\psi}\sinh r$. In order to have an handy expression of the operator in Eq.(1.96) we can use the two-boson representation of the $SU(1,1)$ algebra

$$\begin{aligned} K_+ &= \frac{1}{2}a^{\dagger 2} \\ K_- &= (K_+)^\dagger = \frac{1}{2}a^2 \\ K_3 &= -\frac{1}{2}[K_+, K_-] = \frac{1}{2}(a^\dagger a + \frac{1}{2}) \end{aligned} \tag{1.98}$$

obtaining

$$\begin{aligned} S(\xi) &= \exp\{\xi K_+ - \xi^* K_-\} \\ &= \exp\left\{\frac{\xi}{|\xi|}K_+\right\} \exp\left\{\log(1-\tanh^2|\xi|)K_3\right\} \exp\left\{-\frac{\xi^*}{|\xi|}K_-\right\}, \\ &= \exp\left\{-\frac{\nu}{2\mu}a^{\dagger 2}\right\} \mu^{-(a^\dagger a + \frac{1}{2})} \exp\left\{\frac{\nu^*}{2\mu}a^2\right\} \end{aligned} \tag{1.99}$$

from the last expression it is to derive the action of the squeezing operator on the vacuum state $S(\xi)\,|0\rangle = |\xi\rangle$, shorthand known as squeezed vacuum state:

$$|\xi\rangle = \frac{1}{\sqrt{\mu}}\sum_{k=0}^{\infty}\left(\frac{\nu}{2\mu}\right)^k \frac{\sqrt{(2k)!}}{k!}|2k\rangle. \tag{1.100}$$

In contrast to what the name can ambiguously suggests the vacuum state contains photons and in particular the mean photon energy is given by $\langle\xi|\, a^\dagger a\,|\xi\rangle = |\nu|^2$. When dealing with two mode the corresponding squeezing operator reads:

$$S_2(\xi) = \exp \xi a^\dagger b^\dagger - \xi^* ab \tag{1.101}$$

or in matrix notation:

$$S_2^\dagger(\xi)\begin{pmatrix} a \\ b^\dagger \end{pmatrix} S_2(\xi) = \begin{pmatrix} \mu & \nu \\ \nu^* & \mu \end{pmatrix}\begin{pmatrix} a \\ b^\dagger \end{pmatrix}. \tag{1.102}$$

Using the the two-mode realization of the $SU(1,1)$ algebra

$$\begin{aligned} K_+ &= \frac{1}{2}a^\dagger b^\dagger \\ K_- &= (K_+)^\dagger = \frac{1}{2}ab \\ K_3 &= -\frac{1}{2}[K_+, K_-] = \frac{1}{2}(a^\dagger a + b^\dagger b + \frac{1}{2}) \end{aligned} \tag{1.103}$$

we obtain:

$$S_2(\xi) = \exp\left\{\frac{\nu^*}{\mu}a^\dagger b^\dagger\right\} \mu^{-(a^\dagger a + b^\dagger b)} \exp\left\{-\frac{\nu}{\mu}ab\right\}. \tag{1.104}$$

that allows to compute an analytic expression for the two-mode squeezed vacuum state

$$S_2(\xi)|0\rangle = |\xi\rangle\rangle = \frac{1}{\sqrt{\mu}\sum_{k=0}^{\infty}(\frac{\nu}{\mu})^k}|k\rangle \otimes |k\rangle. \tag{1.105}$$

This state is usually referred to as twin-beam state for the perfect correlation in the photon number of the mode a and b, in fact

$$(a^\dagger a - b \dagger b)|\xi\rangle\rangle = 0. \tag{1.106}$$

whereas the mean energy transported by each mode is given by

$$(a^\dagger a) = \langle b^\dagger b\rangle = \sinh^2 r. \tag{1.107}$$

.

1.5.4 Chacteristic function and Wigner function

The displacement operator let us to introduce the Glauber formula Glauber (1963a); Cahill & Glauber (1969a,b) for the expansion of any operator

$$O = \int_{\mathbb{C}^n} \frac{d^{2n}\boldsymbol{\lambda}}{\pi^n} \chi[O](\boldsymbol{\lambda}) D^\dagger(\boldsymbol{\lambda}) \tag{1.108}$$

where we have introduced the characteristic function

$$\chi[O](\boldsymbol{\lambda}) = \mathrm{Tr}[OD(\boldsymbol{\lambda})]. \tag{1.109}$$

These formulas and the identity

$$\frac{1}{\pi}\mathrm{Tr}[D(\boldsymbol{\lambda})] = \delta^{(n)}(\boldsymbol{\lambda})$$

that the trace rule of two operators could be reconducted from the Hilbert space to an integration over a phase space parametrized by the complex vector $\boldsymbol{\lambda}$

$$\mathrm{Tr}[O_1 O_2] = \frac{1}{\pi^n}\int_{\mathbb{C}^n} d^2n\boldsymbol{\lambda}\chi[O_1](\boldsymbol{\lambda})\chi[O_2](-\boldsymbol{\lambda}). \tag{1.110}$$

The Fourier transform of the characteristic function has a widespread use in the context of the quantum technologies

$$W[O](\alpha) = \int_c n\frac{d^{2n}\boldsymbol{\lambda}}{\pi^{2n}}\, exp\{\boldsymbol{\lambda}^*\alpha + \alpha^\dagger\boldsymbol{\lambda}\}\chi[O](\boldsymbol{\lambda}). \tag{1.111}$$

and it is known as the Wigner quasiprobability distribution. The formalism of the Wigner function let us to introduce a widely class of states widely employed for the development of the quantum information protocols; they are called Gaussian states because their Wigner or characteristic function is Gaussian. Namely a state ϱ of a continuos variable system has

$$W[\varrho](\chi) = \frac{\exp\{-\frac{1}{2}(X-\overline{X})^T\sigma^{-1}(X-\overline{X})}{(2\pi)^n\sqrt{\mathrm{Det}[\boldsymbol{\sigma}]}} \tag{1.112}$$

$$\chi[\varrho](\boldsymbol{\Lambda}) = \exp\frac{1}{2}\boldsymbol{\Lambda}^T\boldsymbol{\sigma}\boldsymbol{\Lambda} + \overline{X}^T\boldsymbol{\Lambda} \tag{1.113}$$

where $\overline{X}$ is the vector of the first order moment and $\boldsymbol{\sigma}$ is the covariance matrix. The expression in 1.112 justify the previous assertion, when we have stated that for a class

of continuos variable systems the covariance matrix is a complete and more manageable tool than the infinite density matrix of the system. Moreover all the states generated by linear and bilinear interaction induced by hamiltonian of the form 1.91 are Gaussian states. Another important function is the Glauber $P-$function defined as the Fourier transform of the normal ordered characteristic function,

$$P[\varrho](\alpha) = \int_c n \frac{d^{2n}\boldsymbol{\lambda}}{\pi^{2n}}\, exp\{\boldsymbol{\lambda}^*\alpha + \alpha^\dagger\boldsymbol{\lambda}\}\mathrm{Tr}[e^{-\frac{1}{2}|\boldsymbol{\lambda}|^2} e^{\boldsymbol{\lambda}a^\dagger} e^{\boldsymbol{\lambda}^* a}\varrho]. \tag{1.114}$$

The peculiarity of this function is that its non analicity is a signature of quantum behavior of the state.

1.6 Summary

In this introductory chapter we have given a brief sketch of the theoretical framework where quantum technologies has been developed. We have started recalling the postulates of the quantum theory, the mathematical theory born in order to understand the behaviour of photons and atoms, and we have given an overview of relevant operators when dealing with optical systems. Then we moved to the geometry of quantum states listing some of the most common distances among them, and we analyzed the quantum estimation theory starting by the classical theory for parameter's estimation. This last theory has deep implication we the geometry of Hilbert space, for this reason a connection between the Bures distance and the estimability of a parameter is addressed.

CHAPTER 2

Drawbacks in the use of fidelity

This chapter is devoted to the analysis how much the evaluation of Uhlmann fidelity between a target state and an unknown one is a good way to asses if the second one has the same physical behaviour of the target. We deal with the most common states used in quantum information protocols, such us gaussian states in continuous variable and qubit system. The chapter is structured in eight sections: in the first four we show off the problem from a theoretical point of view, while in the last four we display the experimental setup to generate the state, we are interested in, the behaviour of fidelity in a realistic scenario compared with the tomographic reconstruction of a state.

2.1 Fidelity and quantum technologies

In this section we address the problem of benchmarking quantum resources with fidelity. The reconstruction of a quantum state given a set of experimental data is a problem that rose in the physics community when the formalization of the quantum mechanics was at its early stage. In fact the intrinsic randomness of the theory does not allow to know the definite state of the system just by a single shot measurement Pauli (1933); Reichenbach (1944); Fano (1957). This problem was eventually solved during the last two decades by the quantum tomography technique. Quantum tomography was applied to a wide range of physical systems ranging from continuous variable quantum optics Smithey et al. (1993); Lvovsky & Raymer (2009); Banaszek et al. (1999); D'ariano et al. (1994) to states living in finite dimensional Hilbert space implemented either on optical supports or on trapped ions Řeháček et al. (2004); James et al. (2001); Steffen et al. (2006). Alongside quantum state tomography is a hard and long experimental procedure that involves the analysis of a huge amount of data. In recent years in the prosperous field of quantum technologies a strategy was introduced to circumvent this expensive situation procedure: once the state has been prepared the fidelity between itself and the state wanted to be achieved, i.e. the target state, is calculated. Fidelity is bounded to the interval $[0; 1]$, so high values such as 0.9 or 0.99 could considered as a piece of evidence in order to assess that two states i) are very close in the Hilbert space ii) share nearly identical physical properties. In this way the quantum resources of the real state could be benchmarked with those of the target one. Given two quantum states described by density matrix ρ_1 and ρ_2 the fidelity between them is defined asUhlmann (1976)

$$F(\rho_1, \rho_2) = \mathrm{Tr}\left[\sqrt{\sqrt{\rho_1}\rho_2\sqrt{\rho_1}}\right]^2 \tag{2.1}$$

although it is not a proper distance in the Hilbert space, fidelity can be linked to distances inducing a metric over the manifold of density matrix. In fact fidelity is directly related

to the Bures distance

$$D_B(\rho_1, \rho_2) = \sqrt{2[1 - F(\rho_1, \rho_2)]} \tag{2.2}$$

between the two states and provides an upper and a lower bound to the trace distance Fuchs et al. (1999)

$$1 - \sqrt{F(\rho_1, \rho_2)} \leq \frac{1}{2}||\rho_1 - \rho_2||_1 \leq \sqrt{1 - F(\rho_1, \rho_2)} \tag{2.3}$$

These relationships ensure that the statement about the closeness of the two states is certainly true, while they do not seem to justify the statement about the physical properties. It has been point out in Bina et al. (2014); Mandarino et al. (2014) that a pair of states close in terms of fidelity may have opposite quantum behaviour. Namely, when considering qubits or two-mode gaussian states, the pair could be composed by one entangled and one separable states, while when dealing with single-mode gaussian states a high value of fidelity is reached even if it is computed between one classical and one quantum state of the radiation field.

2.2 Single-mode Gaussian States

In this section we address the use of fidelity to assess the quantumness of single-mode CV states. In particular subsection 2.2.1 we address nonclassicality of squeezed thermal states, whereas subsection 2.2.2 is devoted the subPossonian character of their displaced version.

2.2.1 Squeezed thermal states

Firstly we consider single-mode CV systems and in particular those having a Gaussian preparation of the form

$$\rho_{s\mu} = S(r)\nu(n_T)S^\dagger(r). \tag{2.4}$$

We refer to them as single-mode squeezed thermal states (STS_1) with real squeezing as introduced in Eq.1.96 $S(r) = \exp\{\frac{1}{2}r(a^{\dagger 2} - a^2)\}$ and n_T thermal photons, $\nu(n_T) = n_T^{a^\dagger a}/(1 + n_T)^{a^\dagger a + 1}$. This class of states is characterized to have null first order moment and therefore their covariance matrix is (CM) given by

$$\sigma = \frac{1}{2\mu}\begin{pmatrix} 1/s & 0 \\ 0 & s \end{pmatrix}, \tag{2.5}$$

where

$$\mu = (2\sqrt{\det \sigma})^{-1} = (2n_T + 1)^{-1} \tag{2.6}$$

$$s = e^{-2r}. \tag{2.7}$$

are the purity of the state and the squeezing factor respectively.

In order to verify if the state is classical or not we will calculate the expression for Glauber P-function introduced in Glauber (1963b). For this class of states

$$P[\rho_{s\mu}](\lambda) = \exp\left\{-(e^r \sinh r + n_T e^{2r})\Re[\lambda]^2 - (-e^{-r}\sinh r + n_T e^{-2r})\Im[\lambda]^2\right\} \tag{2.8}$$

Since the coefficient of $\Re[\lambda]$ is always of opposite sign of that of $\Im[\lambda]$, a singular Glauber P-function occurs when $s < \mu$ or $s > 1/\mu$, see e.g. Lee (1991). Once the figure of merit

for the quantumness has been introduced we can consider the fidelity between two of them; it has an analytic expression derived in Twamley (1996); Scutaru (1998) in terms of the covariance matrix and it is given by

$$F_{s\mu} = \frac{1}{\sqrt{\Delta + \delta} - \sqrt{\delta}} \tag{2.9}$$

where

$$\Delta = \det[\sigma_1 + \sigma_2] \tag{2.10}$$

$$\delta = 4 \prod_{k=1}^{2} \left[\det[\sigma_k] - \frac{1}{4} \right] \tag{2.11}$$

with σ_1 and σ_2 being the CM of the two states. In Fig. 2.1 we report the region of classicality together with the balloons of STS_1 having fidelity larger than $F_{s\mu} > 0.99$ to three STS_1 chosen as targets: one classical thermal state and two nonclassical thermal squeezed states. As it is apparent from the plot, the balloons have large overlaps with

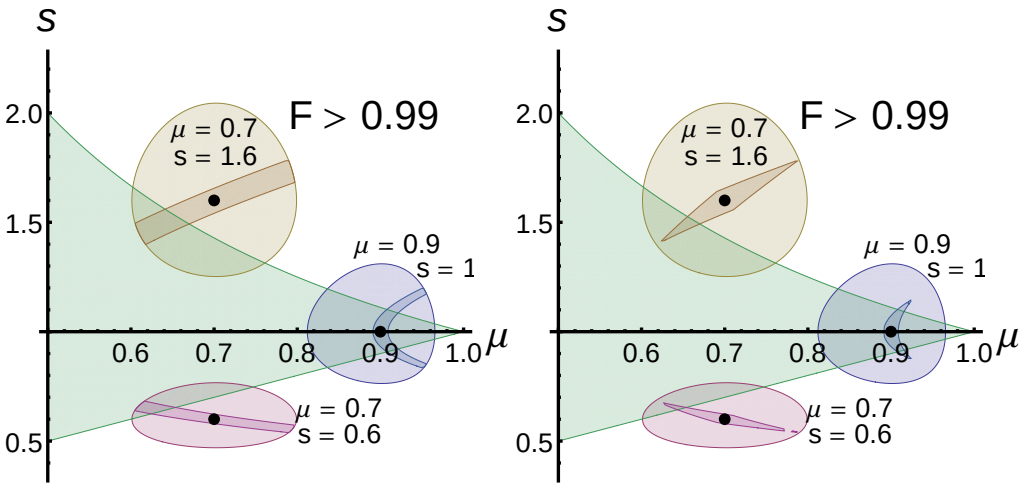

Figure 2.1: The plots show the region of classicality (the green triangular-like regions) together with the balloons of STS_1 having fidelity larger than $F_{s\mu} > 0.99$ to three STS_1 chosen as targets: two nonclassical STS_1 with $\mu = 0.7$ and $s = 0.6$ and $s = 1.6$ and a classical thermal state with $s = 1$ and $\mu = 0.9$ respectively. In the left panel the stripes of states close to the targets contain states having $F_{s\mu} > 0.99$ and mean photon numbers which differ at most 10% from that of the target. In the right panel the states close to the targets satisfy the additional constraints of having number fluctuations within a 10% interval from that of the targets.

both the classical and the nonclassical region, such that fidelity cannot be used, for this class of states, to certify the creation of quantum resources. A strategy to partially overcome this situation is the imposition of additional constraints to the set of states under examination Abramovicz et al. (2013). The first example is shown in the left panel of Fig. 2.1 and it is to bound the energy range of variation. We show the "stripes" of states that have both a fidelity $F_{s\mu} > 0.99$ *and* a mean photon numbers $\langle n \rangle$, (i.e. the mean energy of state) differing at most 10% from that of the target. In the right panel we show the regions of states satisfying also the additional constraints of having photon number fluctuations

$\langle \Delta n^2 \rangle$ within a 10% interval from that of the targets. Overall, we have strong evidence that fidelity should not be used to certify the presence of a quantum character, and that this behaviour is persisting even when we add quite stringent constraints to delimit the class of states under consideration. In fact, only by performing the full tomographic reconstruction of the state one imposes a suitable set of constraints to make fidelity a fully meaningful figure of merit Řeháček et al. (2009). In this case fidelity represents a summary of the precision achieved by the full tomographic reconstruction. Moreover

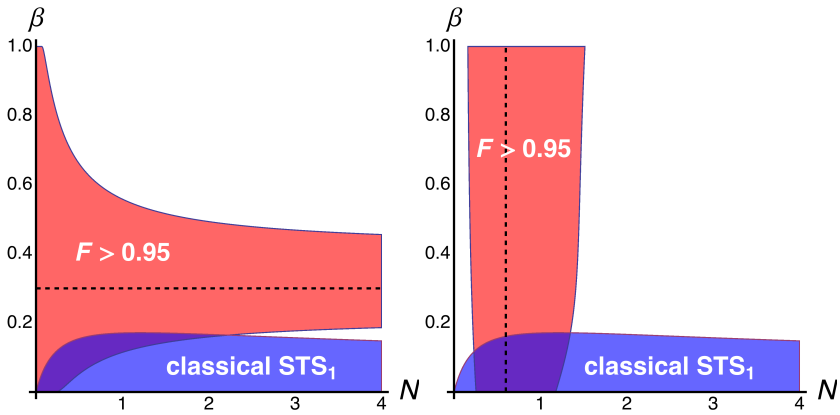

Figure 2.2: Fidelity and nonclassicality. The classical region for STS_1 in the lower part of the plots together with the blue area of states having fidelity $F_{N\beta} > 0.95$ to the set of target state (black dashed line). In the left panel the states are constrained to have the same N and the target state has $\beta = 0.3$. In the right panel the fidelity area is between a target state (black dashed line) with $N = 0.6$ while β is arbitrary but is imposed to be equal to the state with whom fidelity is computed.

another example in the left panel of Fig. 2.2 where we show the region of classicality as a function of the total energy $\langle n \rangle = N$ and the squeezing fraction β (the pink area in the lower part of the picture) together with the region (blue area) of states having a fidelity larger than $F_{N\beta} > 0.95$ to the set of nonclassical states having fixed squeezing fraction $\beta = 0.3$. In the right panel of Fig. 2.2 we show again the region of classical states together with the region of states (blue area) having a fidelity larger than $F_{N\beta} > 0.95$ to the set of states with fixed energy $N = 0.6$. In both cases the areas have a non zero overlap and cross the non classical boundary, such that fidelity cannot be used as unique figure of merit in order to assess quantumness. To summarize: even in this case, when attention is focused on states where we focused our attention on state with quite stringent physical constraints, as fixed energy or squeezing we have strong evidence that fidelity should not be used in benchmarking the generation of quantum resources. We underline that only after a full tomographic reconstruction of the state it is possible to obtains a suitable quorum of physical quantities to properly decrease the area of accessible states, having a given value of fidelity to the target or the set of target states Řeháček et al. (2009).

2.2.2 Displaced squeezed thermal states

In order to illustrate the possible drawbacks of fidelity in certifying this form of quantumness, let us consider the displaced squeezed thermal states, i. e. the displaced version of STS_1

$$\rho_G = D(x)\rho_{s\mu}D^\dagger(x), \tag{2.12}$$

where $D(\alpha) = \exp\{\alpha a^\dagger - \bar{\alpha} a\}$ is the displacement operator introduced in 1.93 and we chose real displacement $\alpha = x \in \mathbb{R}$. The CM is determined by $\rho_{s\mu}$ whereas the displacement change only the mean values of the canonical operators. The covariance matrix of the state in (2.12) is diagonal and reads

$$\sigma = \begin{pmatrix} (n_T + \frac{1}{2})\, e^{2r} & 0 \\ 0 & (n_T + \frac{1}{2}) e^{-2r} \end{pmatrix} \tag{2.13}$$

with A suitable parametrization for DSTS$_1$ may be obtained using the amplitude of the displacement operator x, the average photon number of the squeezed thermal kernel $\rho(0, r, n_T)$, whose energy is given by

$$N = n_T + n_S + 2 n_T n_S \tag{2.14}$$

where n_T is thermal photon numbers and $n_S = \sinh^2 r$ is the squeezing contribution, and the squeezing fraction $\beta \equiv n_s/N \in [0, 1]$. The total average photon number of DSTS$_1$ or equivalently the total energy is given by $\langle a^\dagger a \rangle \equiv \langle n \rangle = x^2 + N$ and the thermal and squeezing component may be expressed as

$$n_T = \frac{(1-\beta)N}{1 + 2\beta N} \tag{2.15}$$

$$n_S = \beta N\,. \tag{2.16}$$

The fidelity between two single-mode Gaussian states $\rho_k(x_k, r_k, n_{T,k})$ with $k = 1, 2$ may be written as Twamley (1996); Scutaru (1998)

$$\begin{aligned} F_{N\beta x} &= \frac{\exp\{(\mathbf{X_1} - \mathbf{X_2})^{\mathbf{T}} (\sigma_\mathbf{1} + \sigma_\mathbf{2})^{-\mathbf{1}} (\mathbf{X_1} - \mathbf{X_2})\}}{\sqrt{\Delta - \delta} - \sqrt{\delta}} \\ &= \exp\{-(\mathbf{X}_1 - \mathbf{X}_2)^T (\sigma_1 + \sigma_2)^{-1} (\mathbf{X}_1 - \mathbf{X}_2)\} F_{s\mu} \end{aligned} \tag{2.17}$$

where $\mathbf{X_k}$=$(x_k, 0)$ The nonclassical character of a DSTS$_1$ may be detected by mean of the Fano factor defined as the ratio of the variance of photon number over the mean photon number as in Paul (1982)

$$R = \frac{\langle n^2 \rangle - \langle n \rangle^2}{\langle n \rangle}\,. \tag{2.18}$$

One has $R = 1$ for coherent states, while a smaller value is a sufficient condition for nonclassicality, since we cannot find any state endowed with a positive Glauber $P-$function showing a sub-Poissonian statistics. In the left panel of Fig. 2.3 we show the region of sub-Poissonianity as a function of the squeezing factor and the purity, and the displacement of states ρ_G. We also show the balloons of states with fidelity larger than $F_G > 0.97$ to two ρ_G target states: a subPoissonian state corresponding to $\mu = 0.9$, $s = 1.4$, and $x = 0.5$ and a superPoissonian one with $\mu = 0.7$, $s = 1.2$, and $x = 1.5$. Despite the high value of fidelity reached, it is worth noting that fidelity decreases exponentially with the displacement amplitude, both the balloons crosses the Poissonian border, and the parameters of the states may differ considerably from the targeted ones. In the right panel of Fig. 2.3 we show the subPoissonian region as a function of squeezing and displacement for a fixed value of purity $\mu = 0.8$, together with the balloons of states having fidelity larger than $F_G > 0.97$ to a pair of target states: a subPoissonian state with parameters $x = 1.5$ and $s = 1.5$ and a superPoissonian one with $x = 0.8$ and $s = 1.0$. We also show the subregions of states having mean photon number and number fluctuations

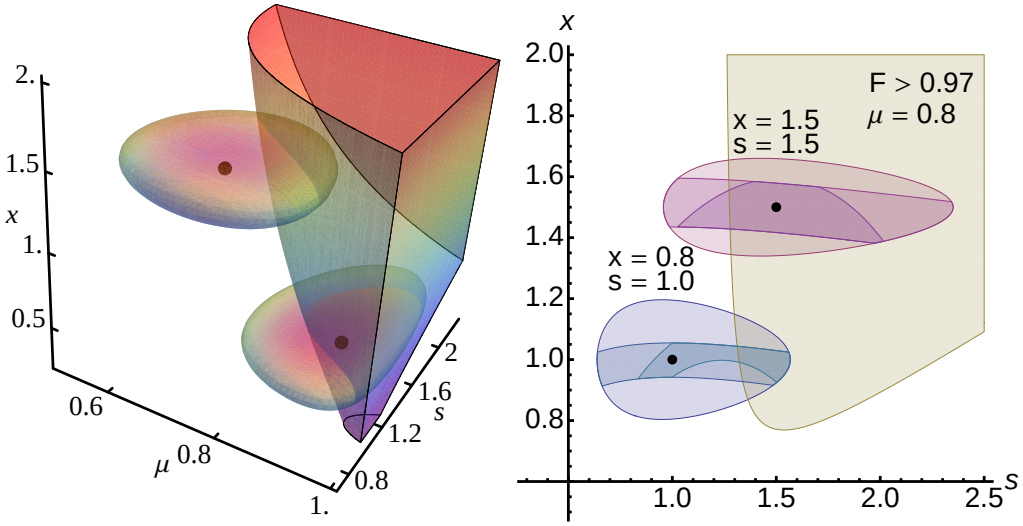

Figure 2.3: (Left): subPoissonian region for ρ_G states as a function of the squeezing s, the purity μ, and the displacement x, together with the balloons of states having fidelity larger than $F_G > 0.97$ to a nonclassical target with $\mu = 0.9$, $s = 1.4$, and $x = 0.5$ and a classical one with $\mu = 0.7$, $s = 1.2$, and $x = 1.5$. (Right): The subPoissonian region for a fixed value of purity $\mu = 0.8$ as a function of squeezing and displacement, together with the balloons of states having fidelity larger than $F_G > 0.97$ to the target states having $x = 1.5$ and $s = 1.5$ (subPoissonian) or $x = 0.8$ and $s = 1.0$ (superPoissonian). We also show the subregions of states having mean photon number and number fluctuations which differ at most 10% from those of the target.

which differ at most 10% from those of the target. We can notice that even restricting attention to states with comparable energy and fluctuations, fidelity is not able to discriminate states having quantum resources or not.

In Fig. 2.4 we show DSTS_1 as points in the space parametrized by N, β and x: the light blue region corresponds to sub-Poissonian states, whereas the red one contains states having fidelity $F_{N\beta x} > 0.99$ to a DSTS_1 with the same value of N and fixed values of $\beta = 0.5$ and $x = 0.5$. As it is apparent from the plot, this set includes both sub-Poissonian and super-Poissonian states, independently on the nature of the target state. Overall, this means that fidelity cannot be used to assess the sub-Poissonian character of DSTS_1 even when we pose a quite strict constraint on the set of considered states.

2.3 Two-mode Gaussian States

Here we focus on a relevant subclass of two-mode Gaussian states: the so-called two-mode squeezed thermal states (STS_2) described by density operators of the form

$$\rho_{N\beta\gamma} = S_2(r)\nu(n_1) \otimes \nu(n_2)S_2^\dagger(r) \tag{2.19}$$

where $S_2(r) = \exp\{r(a^\dagger b^\dagger - ab)\}$ is the two-mode squeezing operator with real parameter r and $\nu(n_k)$, $k = 1, 2$ are thermal states with n_k photon number on average. The class of states $\rho_{N\beta\gamma}$ is fully described by three parameters: the total mean photon number N, the

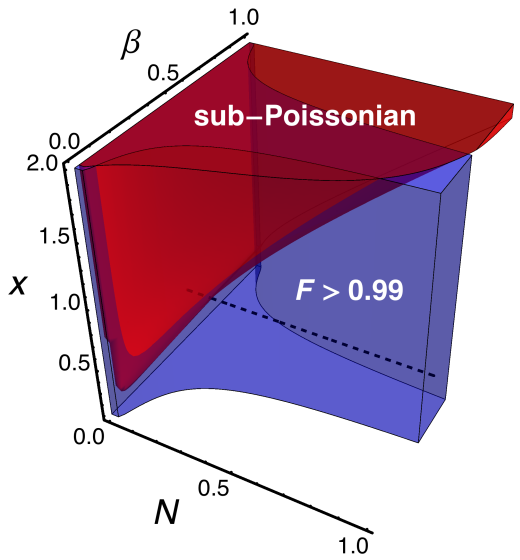

Figure 2.4: Fidelity and sub-Poissonianity. The light blue region contains sub-Poissian DSTS$_1$ whereas the red one contains states having fidelity larger than $F_{N\beta x} > 0.99$ to a DSTS$_1$ with the same value of N and fixed $\beta = 0.5$ and $x = 0.5$.

two-mode squeezing fraction β and the single-mode fraction of thermal photons: γ

$$\begin{aligned} N &= \langle a^\dagger a + b^\dagger b \rangle \\ \beta &= \frac{2\sinh^2 r}{N} \\ \gamma &= \frac{n_1}{n_1 + n_2}. \end{aligned} \tag{2.20}$$

The CM of STS$_2$ may be written in the block form

$$\sigma = \frac{1}{2}\begin{pmatrix} A\,\mathbb{I} & C\,\sigma_z \\ C\,\sigma_z & B\,\mathbb{I} \end{pmatrix} \tag{2.21}$$

with the coefficients parametrized according to (2.20):

$$\begin{aligned} A &= 1 + \frac{2\gamma(1-\beta)N + \beta N(1+N)}{1+\beta N} \\ B &= 1 + \frac{2(1-\gamma)(1-\beta)N + \beta N(1+N)}{1+\beta N} \\ C &= \frac{(1+N)\sqrt{\beta N(2+\beta N)}}{1+\beta N}. \end{aligned} \tag{2.22}$$

A typical quantum resource in two-mode states is the amount of quantum correlation, quantified by entanglement or discord. The entanglement could be attested in terms of positivity of the symplectic eigenvalues of the partial transposed density matrix, which reads Olivares (2012)

$$\tilde{d}_\pm = \sqrt{\frac{\tilde{\Delta}(\sigma) \pm \sqrt{\tilde{\Delta}(\sigma)^2 - 4I_4}}{2}} \tag{2.23}$$

where $I_1 = \det[A\mathbb{I}]$, $I_2 = \det[B\mathbb{I}]$, $I_3 = \det[C\mathbb{I}]$ and $I_4 = \det[\sigma]$ are the local symplectic invariants. A two-mode squeezed thermal state is separable iff $\tilde{d}_- \geq \frac{1}{2}$. The other quantum resource considered is the Gaussian B-discord, i.e. the difference between the mutual information and the maximum amount of classical information obtainable by *local Gaussian* measurements on system B, may be analytically evaluated for STS_2 Giorda & Paris (2010), leading to

$$D(\rho_{N\beta\gamma}) = h(B) - h(d_-) - h(d_+) + h\left(\frac{A - C^2}{B + \frac{1}{2}}\right) \tag{2.24}$$

where we have introduced

$$h(x) = (x + \frac{1}{2})\ln(x + \frac{1}{2}) - (x - \frac{1}{2})\ln(x - \frac{1}{2}) \tag{2.25}$$

known as the binary entropy function. Finally, fidelity between two STS_2 is given by Paraoanu & Scutaru (2000); Marian & Marian (2012); Olivares (2012)

$$F_{N\beta\gamma} = \frac{(\sqrt{X} + \sqrt{X-1})^2}{\sqrt{\det[\sigma_1 + \sigma_2]}} \tag{2.26}$$

where

$$\begin{aligned} X &= 2\sqrt{E_1} + 2\sqrt{E_2} + \frac{1}{2}\,, \\ E_1 &= \frac{\det[\Omega\,\sigma_1\,\Omega\,\sigma_2] - \frac{1}{4}}{\det[\sigma_1 + \sigma_2]}\,, \\ E_2 &= \frac{\det[\sigma_1 + \frac{i}{2}\Omega]\det[\sigma_2 + \frac{i}{2}\Omega]}{\det[\sigma_1 + \sigma_2]}, \end{aligned} \tag{2.27}$$

Ω being the 2-mode symplectic form Olivares (2012)

$$\Omega = \omega \oplus \omega \qquad \omega = \begin{pmatrix} 0 & 1 \\ -1 & 0 \end{pmatrix}.$$

In the left panel of Fig. 2.5 we show the separability region in terms of the three parameters N, β and γ together with the balloons of states having $F_{N\beta\gamma} > 0.99$ with two target states: an entangled STS_2 with parameters $N = 2.5$, $\beta = 0.2$, $\gamma = 0.5$ and a separable one with $N = 1$, $\beta = 0.13$ and $\gamma = 0.5$. As it is apparent from the plot, both balloons cross the separability border and have a considerable overlap to both regions, thus making fidelity of little use to assess entanglement in these kind of systems.

Another phenomenon arising from benchmarking with fidelity is illustrated in the right panel of Fig. 2.5, where we report the region of states having a fidelity in the range $0.95 < F_{N\beta\gamma} < 0.99$ to a *two-mode squeezed vacuum*, i.e. a maximally entangled state with $N = 1$ and $\beta = 1$. The emphasized sector corresponds to states that also have a mean photon number not differing more than 10% from the target, i.e. in the range $0.9 < N < 1.1$. As a matter of fact, the total photon number N and the squeezing fraction β in this region may be considerably different from the targeted one and, in addition, the states with comparable energy are the least entangled in the region. Finally, in Fig. 2.6 we show the range of variation of Gaussian B-discord compatible with high values of fidelity. In the left panel we consider a non-separable target state with discord

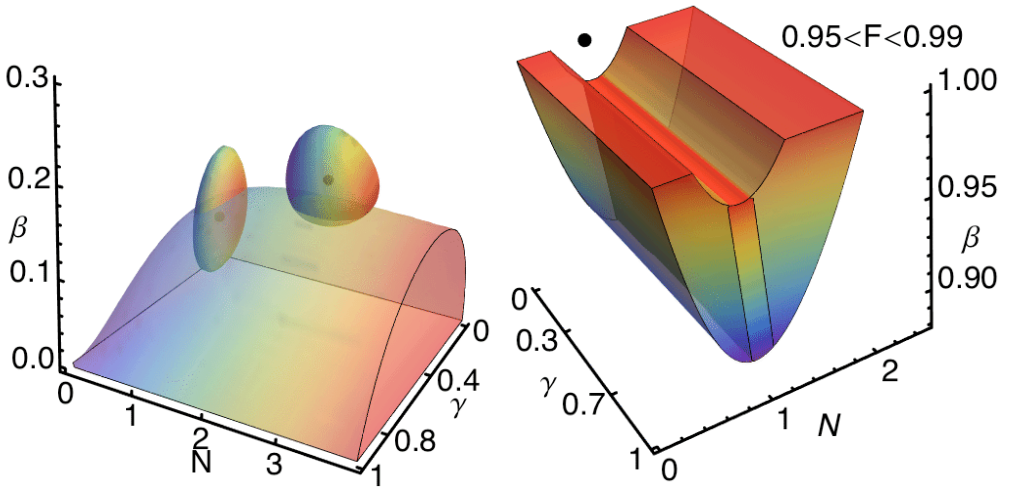

Figure 2.5: (Left): Separability region of STS_2 in terms of the three parameters N, β and γ together with the balloons of states having $F_{N\beta\gamma} > 0.99$ with two target states: an entangled STS_2 with parameters $N = 2.5$, $\beta = 0.2$, $\gamma = 0.5$ and a separable one with $N = 1$, $\beta = 0.13$ and $\gamma = 0.5$. (Right): the region of of states having a fidelity in the range $0.95 < F_{N\beta\gamma} < 0.99$ to a two-mode squeezed vacuum, $N = 1$ and $\beta = 1$. We also show the stripe of states having a mean photon number in the range $0.9 < N < 1.1$.

$D(\rho_{2,0.2,0.5}) = 0.22$ and a region of STS_2 states with fidelity $F_{N\beta\gamma} > 0.95$. The region of separability (green) is crossed by a non negligible set of states and the relative variations of the discord is considerably large, ranging from 0.38 to 1.88. In the right panel of Fig. 2.6 we show again the wide range of variation of Gaussian B-discord for a set of STS_2 states with fidelity $0.95 < F(\rho_{N\beta\gamma}) < 0.99$ to a target two-mode squeezed vacuum state with $N = 2$. The high discrepancy in the relative discord can be only partially limited by constraining the mean photon number N with fluctuations of the 10%. Notice that also in the case of two modes, full Gaussian tomography D'Auria et al. (2009); Blandino et al. (2012) is imposing a suitable set of constraints to make fidelity a meaningful figure of merit to summarize the overall quality of the reconstruction.

In the left panel of Fig. 2.7 we show the separability region in terms of the three parameter N,β,γ and the volume of states having $F_{N\beta\gamma} > 0.99$ with a set of entangled target state with $\beta = 0.2$ and $\gamma = 0.5$. In order to emphasize how the overlap is considerably large in the right panel we have plotted a projection on the plane where it is maximized. The region of separability is crossed by significant fraction of states over all the energy range, thus making fidelity of a little use to asses entanglement in these kind of systems though a severe constraint on the energy of the two states has been provided.

As a final example, let us consider the set of photon-number entangled states (PNES), i.e. two-mode states of the form Allegra et al. (2010, 2011)

$$|\psi\rangle\rangle = \sum_n \psi_n |n, n\rangle\rangle \,,$$

where $|n, n\rangle\rangle \equiv |n\rangle \otimes |n\rangle$. In particular, we focus attention on two specific classes of PNES: the Gaussian two-mode squeezed vacuum states (TWB) $|\psi_T\rangle\rangle = S_2(r)|0\rangle\rangle$ and the non-Gaussian set of states resulting from the process of *photon subtraction* Opatrnỳ et al. (2000); Cochrane et al. (2002); Nha et al. (2012); Paternostro & Kim (2005); Olivares

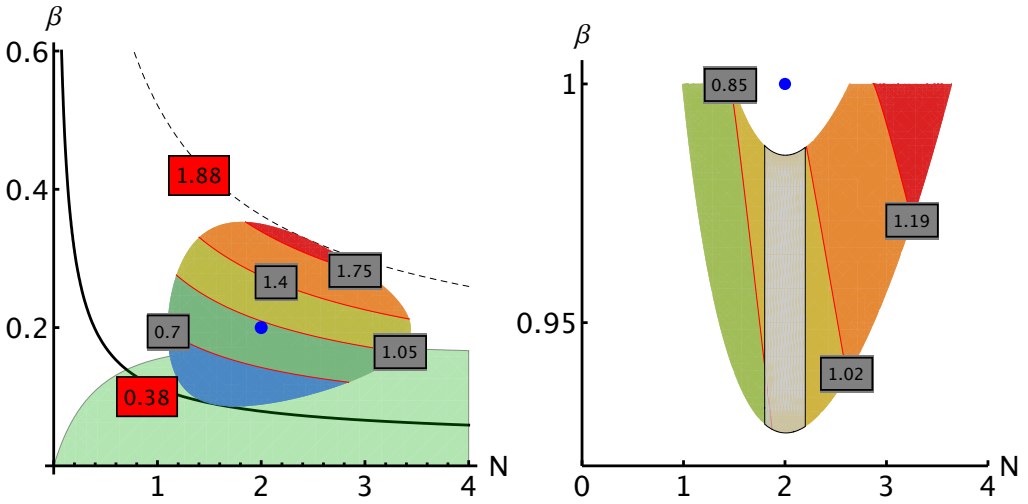

Figure 2.6: (Left): Contour lines of Gaussian B-discord in the region of STS_2 having fidelity $F_{N\beta\gamma} > 0.95$ to an entangled target state with $N = 2, \beta = 0.2$ and $\gamma = 0.5$. The relative discord, rescaled to that of the target state ($D(\rho_{2,0.2,0.5}) = 0.22$), ranges from 0.38 to 1.88. (Right): Variations of the relative Gaussian B-discord in a region of STS_2 with fidelity $0.95 < F_{N\beta\gamma} < 0.99$ to a two-mode squeezed vacuum state ($N = 2$ and $\beta = 1$). In evidence the constrained region of states having the 10% of energy fluctuations around $N = 2$.

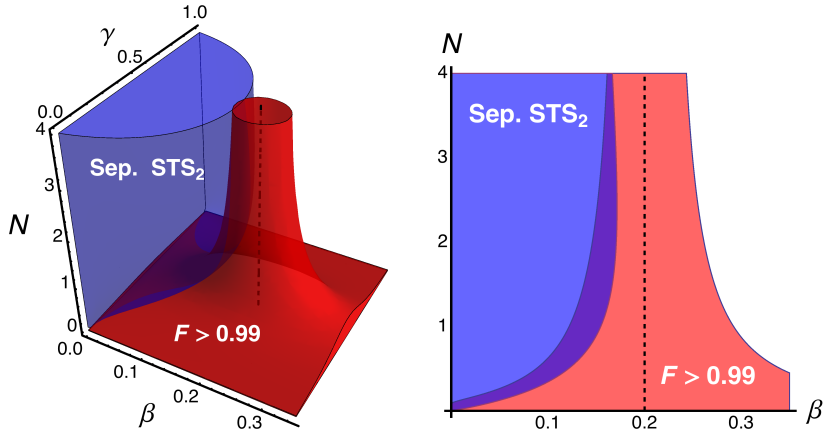

Figure 2.7: (Left): Separability region of STS_2 in terms of the energy parameter N, β and γ on the left together with the volume of states having $F_{N\beta\gamma} > 0.99$ to a set of entangled target STS_2 states (black line) having same energy N and parameter $\beta = 0.2$, $\gamma = 0.5$. (Right): Projection of the separability region of STS_2 in terms of the energy parameter N, β with the area of states having $F_{N\beta\gamma} > 0.99$ over the plane $\gamma = 0.5$.

& Paris (2005); Kloskowska (2008); Kim et al. (2005); Wenger et al. (2004); Huang et al. (2014) applied to $|\psi_T\rangle\rangle$, i.e. $|\psi_S\rangle\rangle \propto \hat{a} \otimes \hat{b}|\psi_T\rangle\rangle$ (PSSV), where $\hat{a}$ and $\hat{b}$ are the annihilation

field operators. In terms of the parameter $y = \tanh r$ we have

$$\psi_n^T = \sqrt{1-y^2}\, y^n \qquad \psi_n^S = \sqrt{\frac{(1-y^2)^3}{1+y^2}}\,(1+n)\, y^n\,, \tag{2.28}$$

such that the average numbers of photons are given by

$$N_T = \frac{y^2}{1-y^2} \qquad N_S = \frac{2y^2(y^2+2)}{1-y^4}\,. \tag{2.29}$$

In the left panel of Fig. 2.8 we show some region plots of the fidelity between a generic TWB and a generic PSSV

$$F_{ST} = |\langle\langle \psi_S|\psi_T\rangle\rangle|^2 = \left(\sum_n \psi_n^T\, \psi_n^S\right)^2\,,$$

as a function of their average number of photons. As it is apparent from the plot, large values of fidelity, e.g. $F_{ST} > 0.9$, are compatible with a relatively large range of energies, corresponding to considerably different physical properties (see below). Notice that for $N_T = N_S \equiv N$ we have $F_{ST} > 27/32 \approx 0.84\ \forall N$: the inset shows the behaviour of F_{ST} as a function of N.

A striking example of a property which cannot be assessed using fidelity is obtained by considering the non-Gaussianity of PSSV. For pure states the non-Gaussian character (quantum negentropy) of a CV states may be quantified by the Von-Neumann entropy of its *reference* Gaussian state, i.e. a Gaussian state with the same CM Genoni et al. (2008); Genoni & Paris (2010); Genoni et al. (2011). For PNES the non-Gaussianity $\delta[\psi]$ reduces to

$$\delta[\psi] = 2h(d_-) \tag{2.30}$$

where

$$h(x) = \left(x+\frac{1}{2}\right)\log\left(x+\frac{1}{2}\right) - \left(x-\frac{1}{2}\right)\log\left(x-\frac{1}{2}\right) \tag{2.31}$$

$$d_- = \sqrt{(N+\frac{1}{2})^2 - C^2}, \tag{2.32}$$

with $C = \sum_n (1+n)\,\psi_n\,\psi_{1+n}$. The non-Gaussianity of PSSV is an increasing function of the energy. In the right panel of Fig. 2.8 we show the non-Gaussianity $\delta_R[\psi_S]$ of PSSV, renormalized to its asymptotic value (such that $0 \leq \delta_R[\psi] \leq 1$) as a function of the fidelity F_{ST} of the same PSSV with a TWB with the same energy. As it is apparent from the plot, very large values of fidelity to a Gaussian states are compatible with a broad range of non-Gaussianity values. The inset shows the behaviour of $\delta_R[\psi_S]$ as a function of N.

As we have previously noted in the continuous variable case, we conclude that also for two-mode states, fidelity should be used with caution in order to assess quantum properties and that this is is true also when one imposes additional constraints on the energy or the squeezing fraction of the states. Notice that also in the case of two modes, full tomography D'Auria et al. (2009); Buono et al. (2010); Blandino et al. (2012) is imposing a suitable set of constraints to make fidelity a meaningful figure of merit to summarize the overall quality of the reconstruction.

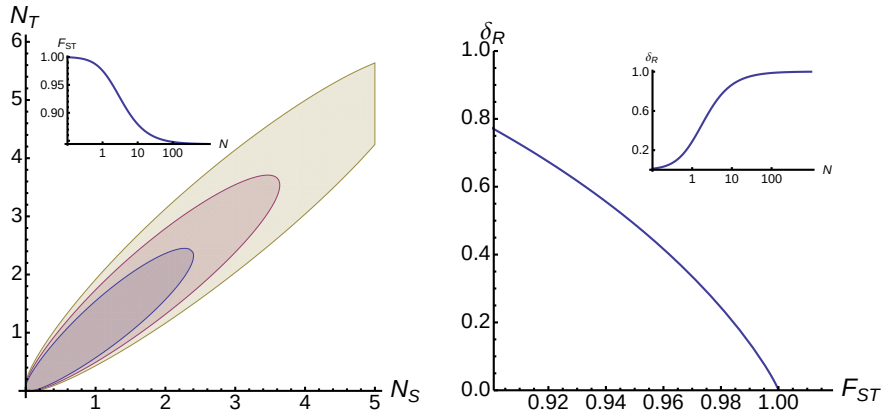

Figure 2.8: (Left): Regions of states having fidelity larger than 0.94, 0.92, 0.9 between a TWB and a PSSV in yellow, red and blue, respectively; in the inset the logarithmic plot of fidelity F_{ST} in function of the energy, with $N = N_S = N_T$, which reaches the value of $27/32$ in the limit $N \to \infty$. (Right): Non-Gaussianity δ_R of PSSV as a function of the F_{ST} to a TWB with same energy N; in the inset the logarithmic plot of δ_R in function of N.

2.4 Two qubit systems

Now we move to states defined in a finite dimensional space, in particular the Hilbert space is $\mathcal{H} = \mathcal{H}_A \otimes \mathcal{H}_B$ with $\dim\mathcal{H}_A = \dim\mathcal{H}_B = 2$. The particular class of states is a subset of *Pauli diagonal* two-qubit states

$$\rho = \frac{1}{4}\left(\mathbb{I}\otimes\mathbb{I} + \sum_{j=1}^{3} c_j \sigma_j \otimes \sigma_j\right) \tag{2.33}$$

where c_j are real constants, $\mathbb{I}$ is the identity operator and σ_j are Pauli matrices. The corresponding eigenvalues are

$$\begin{aligned}
\lambda_0 &= \frac{1}{4}(1 - c_1 - c_2 - c_3)\\
\lambda_1 &= \frac{1}{4}(1 - c_1 + c_2 + c_3)\\
\lambda_2 &= \frac{1}{4}(1 + c_1 - c_2 + c_3)\\
\lambda_3 &= \frac{1}{4}(1 + c_1 + c_2 - c_3)
\end{aligned} \tag{2.34}$$

whose positivity implies constraints on coefficients c_j for ρ to describe a physical state. PD states in Eq. (2.33) have maximally mixed marginals (partial traces) $\rho^A = \rho^B = \mathbb{I}/2$, A and B denoting the two subsystems. The choice of this subset stems from the fact that an analytic expression of the quantum discord is available Luo (2008), so we can compare quantum discord and entanglement of states within the Pauli diagonal class for fixed values of fidelity. The fidelity between two Pauli diagonal states may be expressed in terms of the eigenvalues in Eq. (2.34) as follows

$$F(\rho_1, \rho_2) = \left(\sum_{k=0}^{3} \sqrt{\lambda_{k,1}\lambda_{k_2}}\right)^2, \tag{2.35}$$

whereas entanglement, quantified by negativity, is given by

$$N(\rho) = -2\sum_i \eta_i(\rho^{\tau_A}), \tag{2.36}$$

where $\eta_i(\rho^{\tau_A})$ are the negative eigenvalues of the partial transpose ρ^{τ_A} with respect to the subsystem A Miranowicz & Grudka (2004). The quantum discord for Pauli diagonal states has been evaluated in Luo (2008), and it is given by

$$D(\rho) = I(\rho) - \frac{1}{2}(1-c)\log_2(1-c) - \frac{1}{2}(1+c)\log_2(1+c) \tag{2.37}$$

where $I(\rho) = 2 + \sum_{i=0}^{3} \lambda_i \log_2 \lambda_i$ is the mutual information and the other terms are the result of the maximization of the classical information. The quantity c denotes the maximum $c \equiv \max\{|c_1|, |c_2|, |c_3|\}$.

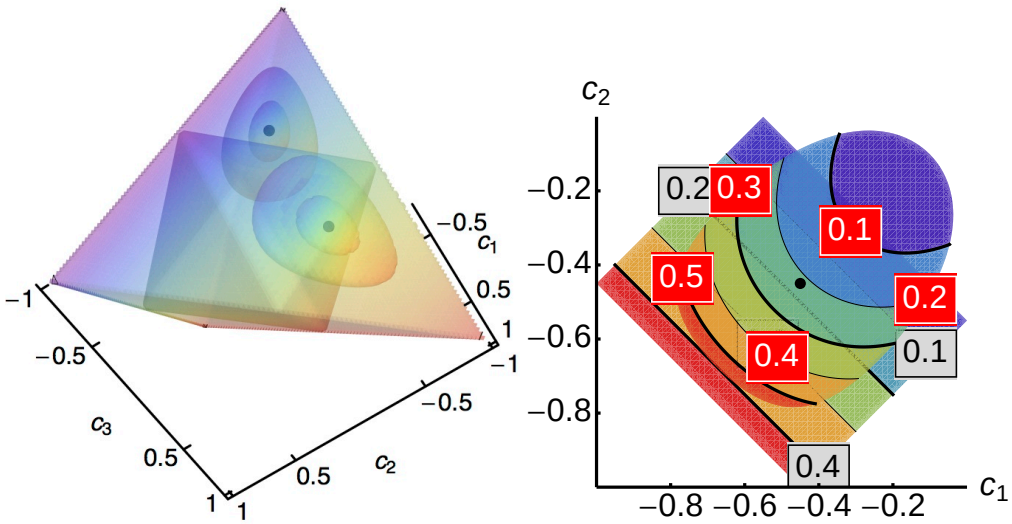

Figure 2.9: (Left panel): The tetrahedron represents the region of all physical Pauli diagonal states, whereas the inner octahedron contains the separable ones. The balloons centered in $c_1 = c_2 = c_3 = -0.45$ (on the right of the panel) contain Pauli diagonal states having fidelity $F > 0.95$ and $F > 0.99$ to the target Werner (entangled) state.The balloons on the left of the panel describe states having fidelity $F > 0.95$ and $F > 0.99$ to the separable Pauli diagonal state with $c_1 = 0.3$, $c_2 = -0.3$, and $c_3 = 0.1$. (Right panel): the plot describes Pauli diagonal states with fixed $c_3 = -0.45$ and varying $\{c1, c2\}$. We show the ovoidal slice containing states having fidelity $F > 0.95$ to the target Werner state with $c_1 = c_2 = c_3 = -0.45$ and the corresponding rectangular region of entangled states. Contour lines refer to entanglement negativity (gray) and quantum discord (red).

Let us now consider a situation where the target state of, say, a preparation scheme, is a Werner state

$$\rho_W = \frac{1-c}{4}\mathbb{I}\otimes\mathbb{I} + c|\Psi^-\rangle\langle\Psi^-|\,,$$

i.e. a Pauli diagonal state with $c_1 = c_2 = c_3 = -c$ and $c \in [0,1]$ and where $|\Psi^-\rangle = (|01\rangle - |10\rangle)/\sqrt{2}$ is one of the Bell states. The Werner state ρ_W is entangled for $c > \frac{1}{3}$ and separable otherwise. In particular, let us choose a target state with $c = 0.45$ and

address the properties of Pauli diagonal states having fidelity larger than a threshold, say $F > 0.95$ or $F > 0.99$ to this target. Results are reported in the left panel of Fig. 2.9, where the tetrahedral region is the region of physical two-qubit Pauli diagonal states and the separable states are confined to the inner octahedron. The ovoidal regions (from now on the *balloons*) contain the Pauli diagonal states with fidelity $F > 0.95$ and $F > 0.99$ to our target Werner state. As it is apparent from the plot, both the balloons cross the separability border, thus showing that a "high" value of fidelity to the target should not be used as a benchmark for creation of entanglement, even assuming that the generated state belongs to the class of Pauli diagonal states. The same phenomenon may lead one to waste entanglement, i.e. to erroneously recognize an entangled state as separable on the basis of a high fidelity to a separable state, as it may happen to an initially maximally entangled state driven towards the separability threshold by the environmental noise. As an example, we show in the left panel of Fig. 2.9 the balloons of states with fidelity $F > 0.95$ and $F > 0.99$ to a separable Pauli diagonal state with $c_1 = 0.3$, $c_2 = -0.3$, and $c_3 = 0.1$.

In the right panel of Fig. 2.9 we show the "slice" of Pauli diagonal states with $c_3 = -0.45$ and fidelity $F > 0.95$ to the Werner target, together with the corresponding region of entangled states, and the contour lines of entanglement negativity and quantum discord. This plot clearly shows that high values of fidelity are compatible with large range of variation for both entanglement and discord.

The fact that neighboring states may have quite different physical properties has been recently investigated for quantum optical polarization qubits Benedetti et al. (2013). In particular in that paper the discord of several two-qubit states has been experimentally determined using partial and full polarization tomography. Despite the reconstructed states had high fidelity to depolarized or phase-damped states, their discord has been found to be largely different from the values predicted for these classes of states, such that no reliable estimation procedure beyond tomography may be effectively implemented, and thus questioning the use of fidelity as a figure of merit to assess quantum correlations. Indeed, when full tomography is performed, fidelity is used only to summarize the overall quality of the reconstruction as in Roos et al. (2004); Fulconis et al. (2007a); Riste et al. (2013); Fulconis et al. (2007b) and thus correctly convey also the information obtained about quantum resources.

2.5 Experimental setup for continuous variable system

Now we will consider the generation of the first class of state we are interested in single-mode CV systems with Gaussian state preparations of the form $\rho_{s\mu} = S(r)\nu(N)S^{\dagger}(r)$ i.e. single-mode squeezed thermal states with real squeezing, $S(r) = \exp\{\frac{1}{2}r(a^{\dagger 2} - a^2)\}$ and N thermal photons, $\nu(N) = N^{a^{\dagger}a}/(1+N)^{a^{\dagger}a+1}$. This class of states have zero mean and covariance matrix (CM) given by Eq.(2.5)

In order to generate them we employed the experimental setup schematically depicted in Fig. 2.10 (a). It consists of three stage: Laser, signal generator (SG) and Homodyne detector (HD). Our source is a home-made internally frequency doubled Nd:YAG laser. It is based on a 4 mirrors ring cavity and the active medium is a cylindrical Nd:YAG crystal (diameter 2 mm and length 60 mm) radially pumped by three array of water-cooled laser diodes @ 808 nm. The crystal for the frequency doubling is a periodically poled MgO:$LiNbO_3$ (PPLN) of 10 mm thermally stabilized ($\sim$70 °C). Inside the cavity is placed a light diode that consist of a half-wave-plate (HWP), a Farady rotator (15 °C) and a Brewster plate (BP) in order to obtain the single mode operation.

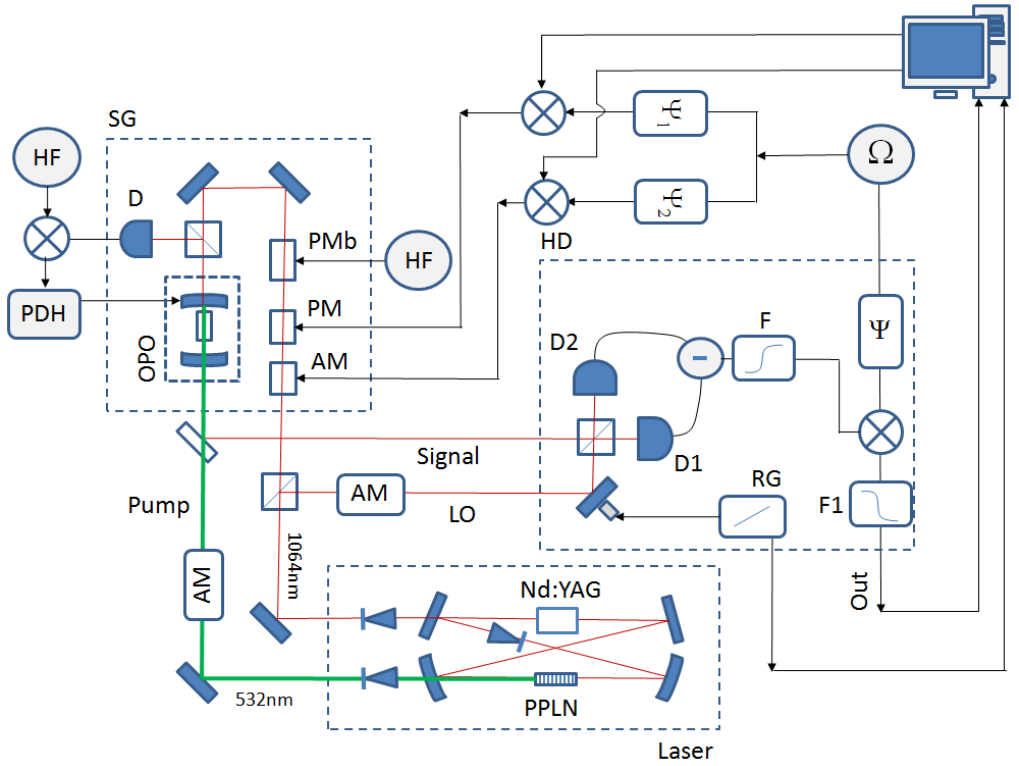

(a)

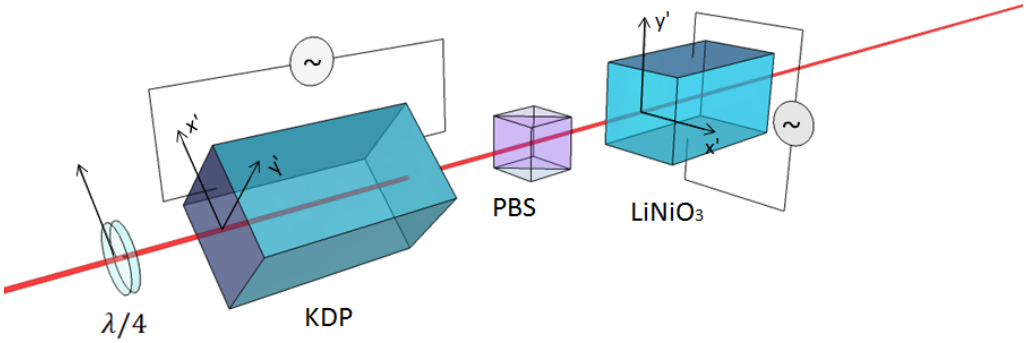

(b)

Figure 2.10: Schematic diagram of the experimental setup. See the text for details.

The laser output at 532 nm is used as the pump for a optical parametric oscillator (OPO) while the output at 1064nm is split into two beams by using a polarizing beam splitter (PBS): one is used as the local oscillator (LO) for the homodyne detector and the other as the input for the OPO. The OPO cavity is linear with a free spectral range (FSR) of 3300MHz, the output mirror has a reflectivity of 92% and the rear mirror 99%. The OPO cavity is actively stabilised with The Pound-Drever-Hall (PDH) technique Drever et al. (1983): the reflected beam from cavity is detected (D) and used to generate the error signal of PDH apparatus. This signal error drive a piezo connected to the rear mirror to actively control the length of the OPO cavity.

The sidebands used for the active stabilization of the OPO cavity are generated by a phase modulator (PMb in Fig. 2.10 (a)) at frequency HF=110 MHz while the sidebands used as input for the OPO are generated at frequency Ω=3 MHz. The linewidth of OPO cavity is 55 MHz, thus the OPO stabilization frequency HF is well above the OPO linewidth while the frequency Ω is well inside. The OPO input sidebands state are generated and manipulated by matching a amplitude modulator (AM) and a phase modulator(PM).

The Homodyne detector (HD) consists of a 50:50 beam splitter, two low noise detector and a differential amplifier based on a LMH6624 operational amplifier. The visibility of the interferometer is about 98%. To remove the low frequency signal we use an high-pass filter @ 500kHz and than the signal is sent to the demodulation apparatus. To extract the information about the signal (that is @ frequency Ω) we use a electronic apparatus which consists of a phase shifter a mixer and a low pass filter @ 300kHz. The LO oscillator phase is spanned between 0 and 360° thanks to a piezo-mounted mirror linearly driven by a ramp generator (RG).

The generation stage of the OPO input states is sketched in more detail in Fig. 2.10 (b). Amplitude modulation is achieved by using a quarter-wave-plate ($\lambda/4$), a KDP crystal and a PBS. The optical field is prepared with circular polarisation by setting the fast axis of $\lambda/4$ at 45 degree angle with respect to the incident *p*-polarisation, and then is passed through a KDP crystal whose axis are oriented at 45°. Selecting only the horizontal component of output beam with a PBS results in purely amplitude modulated field. Finally the beam is sent in a $LiNiO_3$ crystal which perform the phase modulation. This states generation stage is controlled by two identical electronic circuits that consist of a phase shifter and a mixer (see Fig. 2.10 (a)). The phase shifters are set to ensure zero phase shift between the two signals applied to the modulators and the mixers are used to control the voltage applied to the modulators via pc. To generate an arbitrary sidebands state, the Pc send two simultaneous trains of voltage values to the modulators with a DAQ board driven by LabVIEW programming environment, in a time window of 70 ms with a repetition rate of 100 kHz. Generation and acquisition operations are synchronized and therefore we collect 7000 homodyne data points in the same time window at the same sampling rate.

The sampling is triggered by a signal generated by RG to ensure the synchronization between the acquisition process and the scanning of LO from 0° to 360 °.

2.6 Fidelity and tomographic reconstruction for single mode gaussian states

Once the data have been acquired the covariance matrix (CM) of the matrix is reconstructed by homodyne tomograpy. This technique allows to obtain the expectaton value of an observable $\hat{O}$ given a state ρ and its homodyne data sampling $\{\theta_k, x_k\}$ with $k =$

$1, ..., 7000$ and x_k being the outcome from the observation of the quadrature $\hat{x}_{\theta_k} = \hat{a}e^{-i\theta_k} + \hat{a}^\dagger e^{i\theta_k}$ for further details D'Ariano et al. (2003).

Applying the Glauber formula the mean value of the considered observable is

$$\langle \hat{O} \rangle = \int_0^\pi \frac{d\theta}{\pi} \int_{-\infty}^{+\infty} dx p(x,\theta) \mathcal{R}[\hat{O}](x,\theta) \tag{2.38}$$

where $p(x,\theta) = \langle x_\theta | \rho | x_\theta \rangle$ is the probability distribution of quadratures outcome and

$$\mathcal{R}[\hat{O}](x,\theta) = \int_{-\infty}^{+\infty} dy |y| \mathrm{Tr}[\hat{O} e^{iy(\hat{x}_\theta - x)}] \tag{2.39}$$

is the estimator of the operator ensemble average $\langle \hat{O} \rangle$. Since the CM contains the full information only for Gaussian states, a check on the Gaussian hypothesis is necessary in order to validate the approach, we have performed the Shapiro-Wilk test and then we checked if the terms out of the diagonal in the CM are zero within the experimental error, $\langle \hat{x}_{\frac{\pi}{4}} \rangle^2 - \langle \hat{x}_{-\frac{\pi}{4}} \rangle^2 = 0$. This ensure us that they are single mode Gaussian state. It is now possible to treat the states experimentally generated as squeezed thermal. The covariance matrix of this class of states is

$$\sigma = \begin{pmatrix} \Delta\hat{x}^2 & 0 \\ 0 & \Delta\hat{p}^2 \end{pmatrix} = \frac{1}{\mu} \begin{pmatrix} s & 0 \\ 0 & 1/s \end{pmatrix} \tag{2.40}$$

where as usual notation $\hat{x}_0 = \hat{x}$, $\hat{x}_{\frac{\pi}{2}} = \hat{p}$ In Fig.2.11 the behaviour of the two qadratures defining the covariance matrices of the 14 esperimentally generated states is reported. It is clear from the plot that the 8 states with the squeezed variances above the shot-noise limit have non classical properties. Introducing a suitable parametrization for the total energy of the states $N_{Tot} = N + n_s + 2Nn_s$ where $n_s = \sinh^2(r)$ is the number of squeezing photons it is possile to find a linear fit

$$\Delta\hat{x}^2 = \left(1 + 2\frac{N_T - n_s}{2n_s + 1}\right)(1 + 2n_s - 2\sqrt{n_s + n_s^2}) \tag{2.41}$$

$$\Delta\hat{p}^2 = \left(1 + 2\frac{N_T - n_s}{2n_s + 1}\right)\frac{1}{(1 + 2n_s - 2\sqrt{n_s + n_s^2})} \tag{2.42}$$

Then we have random generated 1000 data set starting from a Gaussian distributions with zero mean and standard deviation obtnined from the tomographic reconstruction of each state and we iterated the homodyne tomography procedure for every sampleBIPM et al. (2008). In Fig.2.12 we report the states generated by a Monte Carlo simultation starting from the experimental data of half the whole set of real states. In addition how it is clear from the plot these distribute around the original one, here after the target state, and the energy of a gross part of them relys in the region of one standard deviation from the mean energy of state.

When dealing with gaussian continuous variable systems it is more convenient to skip from the description in terms of density matrix to that provided by the covariance matrix. Hence the fidelity in Eq.2.1 could be restated in terms of the CMs of the 2 states

$$F(\sigma_1, \sigma_2) = \frac{1}{\sqrt{\Delta + \delta} - \sqrt{\delta}} \tag{2.43}$$

where $\Delta = \frac{1}{4}\det[\sigma_1 + \sigma_2]$ and $\delta = \frac{1}{4}\prod_{i=1,2}(\det\sigma_i - 1)$.

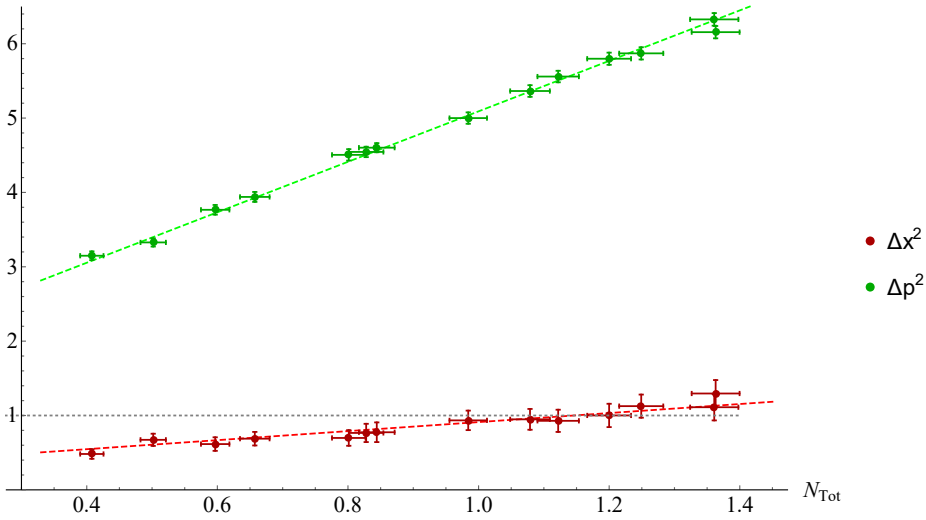

Figure 2.11: We report the variances of squeezed quadrature $\hat{x}$ (red dots) and of the antisqueezed one $\hat{p}$ (green dots) in function of the number of total photons in the state. The dashed lines are linear fits for experimental data with $n_s = 0.197$, while the gray dotted line is the shot-noise limit.

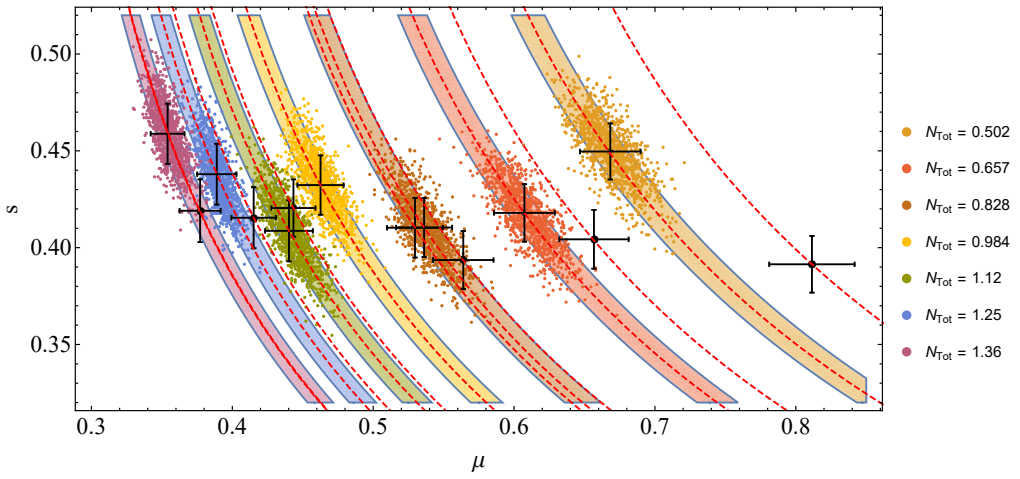

Figure 2.12: The distribution of the random generated states around the corresponding 7 experimental ones in the parameter space identified by the parity μ and the squeezing factor s. The stripes refer to the region where the mean energy of each states varies at most of one standard deviation, while the red dashed lines are isoenergetic curves.

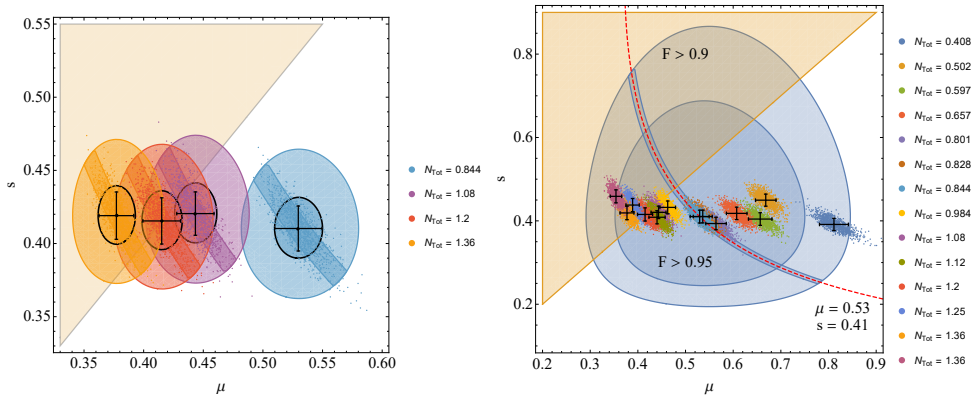

(a) (b)

Figure 2.13: In the left panel: We show the classicality region (orange triangular like), and the baloons of fidelity $F > 0.9$ and $F > 0.95$ with a target state of parameter $\mu = 0.53$ and $s = 0.41$. The red dashed line is $N_{Tot} = 0.844$ In the right panel: From the left to the right we show a classical state, a state on the border of the classicality region (lilac region) and two quantum states with their replicas. The bigger baloon around each of them is the region where $F > 0.997$, while the stripes inside limit the energy range to be in a standard deviation. The black solid bar are the experimental error in the tomographic estimation of the parameter μ and s and circular like lines delimits regions where the states have $F > 0.9995$, roughly coincide with the region where it is possible to remain consistent within the experimental errors.

Thereafter we have computed the regions where we can find states having a fidelity larger than 0.997 or 0.9995 with the target states and the region where they show a singular Glauber P-function, $s < \mu$ or $s > 1/\mu$ as signature of non-classical behaviour. In the left panel of Fig.2.13 we show two classical and two quantum states, as it is clear from the plot the even considering a high value of fidelity. i.e $F > 0.997$ some replicas of the same experiment could lead to state with opposite behaviour. Moreover if we would like to have states belonging to the region individuated by the accuracy of our experimental setup we have to reach $F > 0.9995$

It is clear from that we are dealing with very high values of fidelity but this is still not a sufficient condition in order to be able to certify quantum resources. A more dramatic situation arises when considering usual values of fidelity considered to be high, i.e. 0.9 and 0.95. This is well pointed out in the right panel of Fig.2.13, where considering those value of fidelity could not allow to distinguish among none (or almost none)of the remaining experimental state.

Our purpose is to generate the Werner state

$$\rho_W = p|\Psi^-\rangle\langle\Psi^-| + \frac{1-p}{4}\mathbf{I_4} \tag{2.44}$$

whose density matrix, expressed in the $|HH\rangle$, $|HV\rangle$, $|VH\rangle$, $|VV\rangle$ basis can be written as

$$\rho_W = \begin{pmatrix} \frac{1-p}{4} & 0 & 0 & 0 \\ 0 & \frac{1+p}{4} & -\frac{p}{2} & 0 \\ 0 & -\frac{p}{2} & \frac{1+p}{4} & 0 \\ 0 & 0 & 0 & \frac{1-p}{4} \end{pmatrix} \tag{2.45}$$

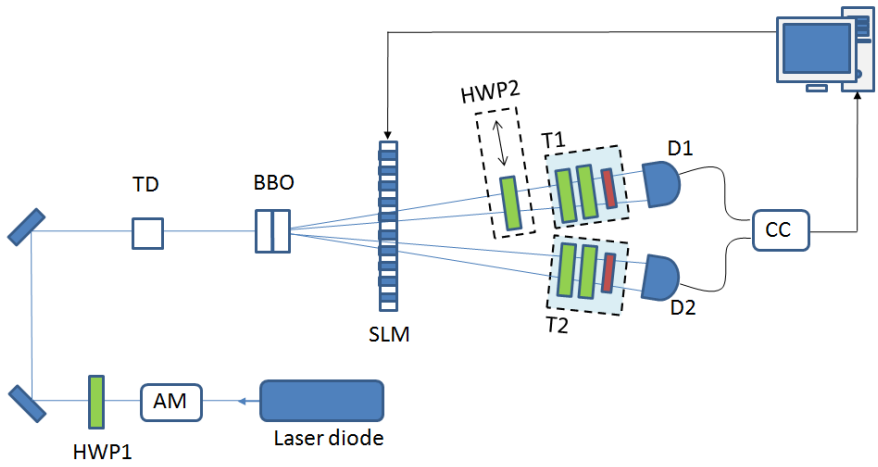

Figure 2.14: Schematic diagram of experimental setup. A linearly polarized cw laser diode at 405 nm pumps a couple of BBO crystals cut for type-I downconversion. The horizontal and vertical amplitudes of the photon pairs are balanced by a half-wave plate set along the pump path (HWP1), whereas an additional BBO crystal (TD) is placed on the pump path to compensate the temporal delay. The amplitude modulator (AM) consists of a half-wave-plate and polariser-beam-splitter. Signal and idler beams travel through the SLM, which provides purification of the generated states. A half-wave plate (HWP2) is inserted on signal path in order to generate the state ρ_V (see the text), whereas a quarter-wave plate, a half-wave plate, and a polarizer (sectors T1 and T2) are used for the tomographic reconstruction. Finally the beams are detected by detectors D1 and D2 ad sent to single-photon counting modules (CC)

It consist of a mixture of a pure state $\Psi^- = \frac{1}{\sqrt{2}}[|HV\rangle - |VH\rangle]$ and a fully mixed state expressed by the unit operator $\mathbf{I_4}$ defined in the 4-dimensional Hilbert space. Depending on the weight p, Werner states may be entangled ($p > 1/3$) or separable ($p \leq 1/3$).

With our experimental apparatus, we can generate two kinds of states: the polarization entangled states $\rho_V = V|\Psi^-\rangle\langle\Psi^-| + (1-V)\rho_{\text{mix}}$, where $\rho_{\text{mix}} = \frac{1}{2}[|HV\rangle\langle HV| + |VH\rangle\langle VH|]$, and the mixture states $\rho = \frac{1}{2}(|HH\rangle\langle HH| + |VV\rangle\langle VV|)$ Cialdi et al. (2008)Cialdi et al. (2011).

Therefore it is possible to realize the Werner state ρ_W upon considering the mixture

$$\rho_W = f_1\rho_V + f_2\rho$$

where $f_1 = \frac{1+p}{2}$, $f_2 = \frac{1-p}{2}$ and $V = 2\left(\frac{1+3p}{2(1+p)}\right) - 1$.

2.7 Experimental setup for qubit generation

A schematic diagram of experimental setup is sketched in Fig. 2.14. The state ρ_V is generated by type-I downconversion from a couple of crystals [beta barium borate (BBO)] in a non-collinear configuration pumped with a linearly polarized cw 405 nm laser diode whose effective power on the generating crystals is about 10 mW.

With respect to experimental technique already described in more detail in Refs Cialdi et al. (2008) Cialdi et al. (2009) , a half-wave plate (HWP2 in Fig. 2.14) inserted in front of detector D1 performs the $|\Phi^-\rangle = \frac{1}{\sqrt{2}}\{|HH\rangle - |VV\rangle\} \rightarrow |\Psi^-\rangle$ transformation.

A programmable one-dimensional spatial light modulator (SLM) is placed on the path of signal and idler in order to control the visibility of the generated states. The SLM makes our system greatly flexible allowing to set the visibility of generated states as we want Cialdi et al. (2010) Cialdi et al. (2012).

Finally, photons are focused in two multimode fibers and sent to single-photon counting modules (CC).

In order to generate the mixed state ρ, we use the same scheme (see Fig. 2.14) by removing the HWP2 from the signal path and setting SLM in order to get $V \simeq 0$. The frequencies f_1 and f_2 are set by changing the power of the pump beam with an amplitude modulator (AM).

The tomographic measurements of generated states are obtained by inserting a quarter-wave plate, a half-wave plate, and a polariser (sectors T1 and T2 in Fig. 2.14: in order to reconstruct the density matrix ρ_W we have performed 16 measures and, for each tomographic apparatus setting, we have taken 30 acquisitions of 1 s. The quorum of observable for the reconstruction of the density matrix is the set of independent projectors in the two-qubit space $P_\nu = |\psi_\nu\rangle\langle\psi_\nu|$ with $\nu = 1...16$; once these P_ν have been measured it is possible to compute the probabilities $p_\nu = \langle\psi_\nu| \rho_\nu |\psi_\nu\rangle$ from the number of counts n_ν. The reconstruted density matrix is obtained by a maximum likelihood method and its positivity is ensured by the Choleski decomposition that states it is always possible to write any non negative matrix as product of a complex lower triangular T with its hermitian adjoint, $\rho = T^\dagger T / \mathrm{Tr}[T^\dagger T]$. The problem is to determine 16 real variable t_j on which the density matrix depends, i.e. $\rho(t_1, t_2, ..., t_{16})$. Hence the likelihood method allows to recontruct the matrix best fitting the experimental data, in order to do this the likelihood functional should be introduced or with with its natural logarithm because is easier to deal with when performing numerical analysis

$$\mathcal{L}(T) = \sum_{\nu=1}^{16} \ln \mathrm{Tr}[T^\dagger T P_\nu] - \lambda \mathrm{Tr}[T^\dagger T]$$

where λ is a Lagrangian multiplier accounting for the normalization of ρ. In the Gaussian approximation and for a given data count set $\{n_\nu\}_{\nu=1}^{16}$ of a density matrix of a $2-$qubit states, the log-likelihood function , depending on the coefficients t_ν and on the probabilities p_ν (through the counts n_ν) is given by

$$\mathcal{L}(T) = N_T \sum_{\nu=1}^{16} \frac{[\langle\psi_\nu| \rho(t_1, t_2, ..., t_{16}) |\psi_\nu\rangle - n_\nu]^2}{2 \langle\psi_\nu| \rho(t_1, t_2, ..., t_{16}) |\psi_\nu\rangle} \tag{2.46}$$

where $N_T = \sum_{\nu=1}^{16} n_\nu$ is a constant proportional to the total number of acquisitions. By numerically maximizing over the variables t_ν is possible to reconstruct the Maximum Likelihood matrix. Then we have Monte Carlo sampled counts from a Gaussian distribution with mean and standard deviation equal to the experimental recorded data, and we iterated the maximum likelihood procedure for each of those numerically generated samples.

2.8 Fidelity and tomography in qubit systems

At this stage we have a simulation of an experiment involving a 2-qubit Werner state, we suppose that the 1000 Monte Carlo (MC) generated states are in the neighborhood of the expected Werner state of parameter p. We suppose that the target state is the Werner state, $\bar{\rho}_W(p)$, maximizing the fidelity with the mean state $\bar{\rho}^k = \sum_1^{N_s} \rho_i^k / N_s$ with $k = 1, ..., 5$ and $N_s = 1000$ the number of MC simulations. The process of the optimization leads to the following values of p : $p_1 = 0.312$, $p_2 = 0.346$, $p_3 = 0.345$, $p_4 = 0.276$, $p_5 = 0.432$. 7 Now it is possible to study the amount of correlation of each of the 1000 states in terms of the fidelity it shares with the corresponding Werner target state. The first figure of merit to quantify quantum correlations, is an entagled measure known negativity Miranowicz & Grudka (2004), is given by

$$N(\rho) = -2 \sum_i \eta_i(\rho^{\tau_A}), \tag{2.47}$$

where $\eta_i(\rho^{\tau_A})$ are the negative eigenvalues of the partial transpose ρ^{τ_A} with respect to the subsystem A Miranowicz & Grudka (2004). In Fig. 2.15 we plot the least eigenvalue, instead of the negativity, of the density matrix in function of the fidelity. It is clear form the definition of negativity that states with all the eigenvalues of the partial transpose positive are separable while when at leat one of its eigenvalues is negative the 2-qubit state is entangled. In Fig.2.15(a) we show the results obtained for $\bar{\rho}_W(p_1)$ and $\bar{\rho}_W(p_2)$; they both live near the border of separability region but the first is separable while the second is entangled. It is clear from the plot that even if the fidelity between any of the reconstructed density matrix and the corresponding Werner state is larger than 0.9 there is no way to avoid high values of fidelity between pair of states with opposite physical property. In Fig.2.15(b) the behaviour of the least eigenvalues of the MC sampled states in function of the fidelity with $\bar{\rho}_W(p_1)$, $\bar{\rho}_W(p_4)$ and $\bar{\rho}_W(p_5)$.

Another widely adopted measure of the amount of quantum correlation in a state ρ is the quantum discord defined as the difference between two classical equivalent definition of the total amount of correlation in a state, viz. the mutual information, that are different in the quantum domain.

In fact given a bipartite quantum state, the amount of residual information once a measurement is performed upon one part is

$$D_B(\rho) = \mathcal{I}(\rho) - \mathcal{J}(\rho) = S(\rho_B) + \min \sum_k p_k S(\rho_{A|k}) - S(\rho) \tag{2.48}$$

where $S(\rho)$ denotes von Neumann entropy and $\rho_{A|k} = \mathrm{Tr}_B[\Pi_k \rho \Pi_k]/p_k$ is the conditional state of the system A after obtaining outcome k on B, $\{\Pi_k\}$ is a set of projectors acting on B and $p_k = \mathrm{Tr}[\Pi_k \rho \Pi_k]$ is the probability of obtaining the outcome k. In Fig. 2.16 we show how the discord of the MC matrices distrutes in function of the fidelity with their corresponding target state. It is possible to see that in comparison with the results in Fig.2.16, highest values of discord correspond to the more entangled states.

In the left panel of Fig.2.16 we show the results obtained for $\bar{\rho}_W(p_1)$ and $\bar{\rho}_W(p_2)$, while in the right panel of Fig.2.16 the behaviour of the least eigenvalues of the MC sampled states in function of the fidelity with $\bar{\rho}_W(p_1)$, $\bar{\rho}_W(p_4)$ and $\bar{\rho}_W(p_5)$. Another anomalous feature we would like to point out when trying to benchmark with fidelity is outlined in the histogram in Fig.2.17. We have computed the fidelity each realization ρ_i^4, i.e. states generated starting from the separable state most distant from the critical value $p = 1/3$, has with ρ_{Ave}^5, i.e.the mean of the states generated starting from the most entangled state. It is $F = 0.959 \pm 0.013$

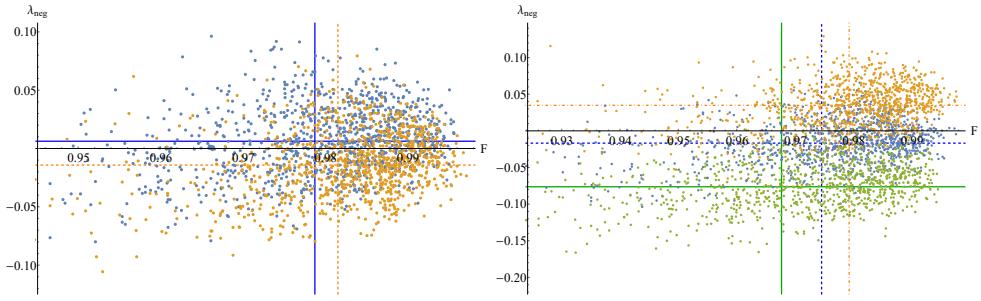

Figure 2.15: We report the least eigenvalue of the partial transpose matrix versus the fidelity each states sheres with the closest Werner state to the mean state of them.
In the upper panel the results are for $\bar{\rho}_W(p_1)$ (blue dots) and $\overline{\rho}_W(p_2)$ (orange dots). The lines refer to the average fidelity and to the average of the least eigenvalues: $F(\overline{\rho}_W(p_1), \overline{\rho}^1) = 0.978 \pm 0.012$ (vertical blue solid line), $F(\overline{\rho}_W(p2), \overline{\rho}^2) = 0.982 \pm 0.013$ (vertical orange dashed line), $\overline{\lambda}(\overline{\rho}^1) = 0.006 \pm 0.030$ (horizontal blue solid line), $\overline{\lambda}(\overline{\rho}^2) = -0.014 \pm 0.028$ (horizontal orange dashed line). In the lower panel the results are for $\bar{\rho}_W(p_3)$ (blue dots), $\overline{\rho}_W(p_4)$ (orange dots) and $\overline{\rho}_W(p_5)$ (green dots). As in the previous plot the lines refer to: $F(\overline{\rho}_W(p_3), \overline{\rho}^3) = 0.975 \pm 0.018$ (vertical blue dashed line), $F(\overline{\rho}_W(p4), \overline{\rho}^4) = 0.979 \pm 0.012$ (vertical orange dotdashed line), $F(\overline{\rho}_W(p5), \overline{\rho}5) = 0.9682 \pm 0.025$ (vertical green solid line), $\overline{\lambda}(\overline{\rho}^3) = -0.017 \pm 0.029$ (horizontal blue dashed line), $\overline{\lambda}(\overline{\rho}^4) = 0.034 \pm 0.020$ (horizontal orange dotdashed line), $\overline{\lambda}(\overline{\rho}^5) = -0.007 \pm 0.030$ (horizontal orange dashed line)

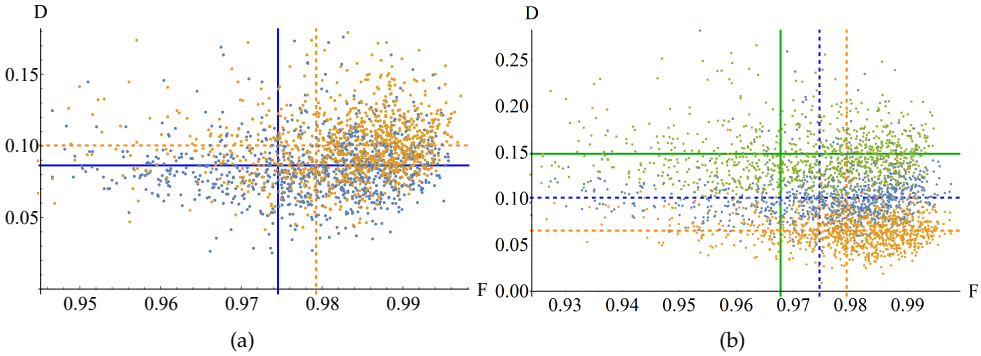

Figure 2.16: We report the least eigenvalue of the partial transpose matrix versus the fidelity each states shares with the closest Werner state to the mean state of them.
In the upper panel the results are for $\bar{\rho}_W(p_1)$ (blue dots) and $\overline{\rho}_W(p_2)$ (orange dots). The lines refer to the average fidelity and to the average of the least eigenvalues: $F(\overline{\rho}_W(p_1), \overline{\rho}^1) = 0.978 \pm 0.012$ (vertical blue solid line), $F(\overline{\rho}_W(p2), \overline{\rho}^2) = 0.982 \pm 0.013$ (vertical orange dashed line), $D(\overline{\rho}^1) = 0.086 \pm 0.024$ (horizontal blue solid line), $D(\overline{\rho}^2) = 0.100 \pm 0.033$ (horizontal orange dashed line). In the lower panel the results are for $\bar{\rho}_W(p_3)$ (blue dots), $\overline{\rho}_W(p_4)$ (orange dots) and $\overline{\rho}_W(p_5)$ (green dots). As in the previous plot the lines refer to: $F(\overline{\rho}_W(p_3), \overline{\rho}^3) = 0.975 \pm 0.018$ (vertical blue dashed line), $F(\overline{\rho}_W(p4), \overline{\rho}^4) = 0.979 \pm 0.012$ (vertical orange dotdashed line), $F(\overline{\rho}_W(p5), \overline{\rho}5) = 0.9682 \pm 0.025$ (vertical green solid line), $D(\overline{\rho}^3) = 0.101 \pm 0.034$ (horizontal blue dashed line), $D(\overline{\rho}^4) = 0.066 \pm 0.009$ (horizontal orange dotdashed line), $D(\overline{\rho}^5) = 0.007 \pm 0.005$ (horizontal orange dashed line)

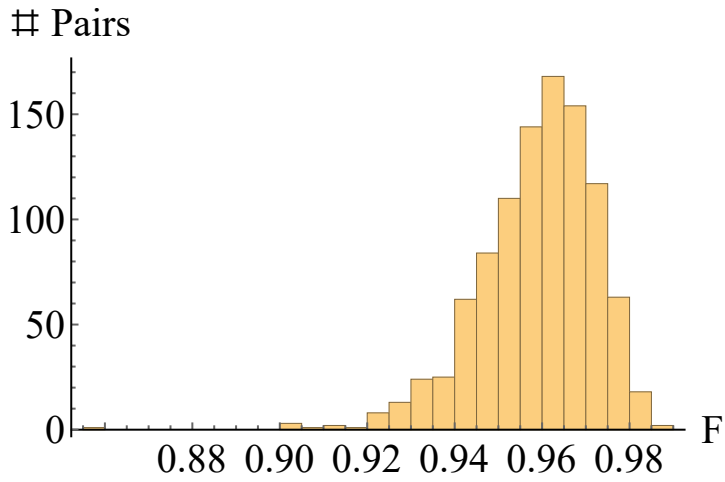

Figure 2.17: Histogram showing the distribution of fidelities between pairs of state composed by a realization of a separable state and an entangled one, $F(\rho_i^4, \rho_{Ave}^5)$.

2.9 Conclusion

We have exploited the use of Uhlmann fidelity when used in order to assess quantum resources. We have firstly considered the trivial assumption that couples of states with a high value of fidelity should share almost the same physical properties, therefore we have shown several example where this statement is not confirmed. We have considered continuous variable states, in particular single mode and two mode gaussian states: for the former class of states we have tried to assess their quantumness by means of the negativity of the Glauber-Surdashan P-function and of the Fano factor, whilst for the latter class we have explored the behaviour of the quantum correlation between the two modes of a pair of states in function of the fidelity. We have examined also how fidelity could be employed to assess the quantum resources, such us entanglement and discord, in two qubit systems. The results adduce a strong theoretical evidence against the common sense assumption, in fact states with high value of fidelity could show opposite character. To ensure that the statement is bad posed we have imposed some physical constraint, even if it reduces the volume of states with high fidelity it does not avoid the effect.

Finally we have tested our evidence in an experimental framework. This has also given the ability to compare fidelity among two states and the tomographic reconstruction. What we have found is that fidelity by itself does not give any quantitative information about the physics of a quantum states. In particular all the features required in the speed-up of certain quantum technologies protocols are very badly benchmarked by fidelity. In contrast the tomographic reconstruction of a states is the only technique, although it is a bit tedious, capable to give the exact information on a state.

CHAPTER 3

Quantum metrology in Lipkin-Meshkov-Glick critical systems

We first consider the characterization of LMG systems, i.e. the estimation of anisotropy, and show how criticality may be exploited to improve precision. To this aim we evaluate exactly the quantum Fisher information of small-size LMG chains made of $N = 2, 3$ and 4 lattice sites and also address the thermodynamical limit by a zero-th order approximation of the system Hamiltonian. Our results show that the maxima of the quantum Fisher information are obtained on the critical lines in the parameter space, i.e. where the ground state of the system is degenerate. We also show that the ultimate bounds to precision may be achieved in practice by tuning the external field and by measuring the total magnetization of the system. We also address the use of LMG systems as quantum thermometers, i.e. we consider a LMG chain in thermal equilibrium with its environment and analyze the estimation of temperature by quantum-limited measurements on the sole LMG system. We show that the precision is governed by the gap between the lowest energy levels of the systems, such that the field-dependent level crossing provides a metrological resource to extend the operating range of the quantum thermometer.

3.1 Spin system in quantum information theory

During the last decade a plentiful contamination between condensed matter physics and quantum information theory has been exploited. On the one hand, many body systems exhibiting quantum phase transitions (QPTs), usually studied in terms of order parameters, correlation lengths and symmetry breaking Sachdev (1999) have been fruitully analyzed in terms of quantum information based tools, such as dynamics of correlation in the ground state (GS) of the systems Amico et al. (2008) and quantum information geometry Zanardi & Paunković (2006); Zanardi et al. (2007a); Cozzini et al. (2007); Zanardi et al. (2007b); Prokopenko et al. (2011). On the other hand, quantum critical systems have been shown to provide a resource for quantum estimation and metrology, offering superextensive precision in the characterization of coupling parameters and thermometry Zanardi et al. (2008); Invernizzi et al. (2008); Invernizzi & Paris (2010).

A previously mentioned the pillar of quantum estimation theory resides in the quantum Fisher Information Helstrom (1976); Paris (2009). The tools provided by this statical approach to the geometry of quantum states has been employed in the context of the theory of quantum phase transition.

Indeed, the geometrical approach to QPT has shown how to improve estimation strategies for experimental inaccessible parameter by driving the system towards critical points, where a sudden change in the ground state structure takes place Venuti & Zanardi (2007); Zanardi et al. (2008). In particular this behaviour has been tested in

models where the interaction is restricted to first neighbors Invernizzi et al. (2008); Invernizzi & Paris (2010); Garnerone et al. (2009), e.g. quantum Ising and X-Y models in an external field, in order to precisely estimate the parameters of the system and to provide useful information about the phase diagram. In view of the attention paid to systems with more sophisticated interaction among lattice sites Zhong & Castleman Jr (2003); Tsomokos et al. (2008); Gatteschi et al. (2006); Troiani & Zanardi (2013) a question thus naturally arises on whether criticality may be exploited to enhance metrology in systems with interaction beyond the first-neighbor approximation.

In this framework, systems described by the Lipkin-Meshkov-Glick (LMG) model provide non trivial examples to assess quantum criticality as a resource for quantum estimation. LMG was first proposed as a simple test for many-body problems approximations Lipkin et al. (1965); Meshkov et al. (1965); Glick et al. (1965) and since then it has been used to describe the magnetic properties of several molecules, remarkably $Mn_{12}Ac$ Garanin et al. (1998). It also found applications in several different fields, leading to a variety of results in terms of entanglement properties of its ground state Dusuel & Vidal (2004, 2005); Wichterich et al. (2010) and spin squeezing Ma & Wang (2009). For finite size chains LMG have been characterized in terms of fidelity susceptibility Kwok et al. (2008); Ma et al. (2009); Castaños et al. (2012) and adiabatic dynamics Caneva et al. (2008, 2009); Solinas et al. (2008). Although the LMG model cannot be solved analytically for a generic chain size, some of its extensions are amenable to an exact solution Fuentes-Schuller & Barberis-Blostein (2007). We also mention that the LMG model received attention not only theoretically: experimental implementations have been proposed using condensate systems in a double well potential Micheli et al. (2003) or in cavities Chen et al. (2009); Morrison & Parkins (2008). It has been also shown that is possible to map the dynamics of such model on circuit QED Larson (2010) and ion traps Unanyan & Fleischhauer (2003) systems.

In the context of metrology the crucial feature of the LMG model is that its Hamiltonian depends on two parameters: the anisotropy parameter, that ... the interaction between spins in the x-direction from the interaction in the y-direction and it is not accessible to the experimenter, while the other is the external magnetic field, an experimentally tunable parameter and the one that could be used, in some extent, to drive the system towards a critical behaviour.

3.2 The LMG model

In this section we review the main features of the Lipskin-Meshkov-Glick model. As a matter of fact, the model has been widely studied in many branches of science and it is known in several equivalent forms. We present the most relevant ones, with emphasis on the symmetries of the system.

The original formulation Lipkin et al. (1965); Meshkov et al. (1965); Glick et al. (1965) were introduced in the framework of the nuclear physics in order to describe a system composed of N fermions occupying two N-fold degenerated levels separated by an energy gap ϵ. Labelling the two levels by the index $s = -1, 1$ and the letting $p = 1, ...N$ be an index exploring the degeneracy of the levels, we can consider a fermion algebra spanned by

$$\left\{\alpha_{ps}, \alpha^{\dagger}_{p's'}\right\} = \delta_{pp'}\delta_{ss'} \tag{3.1}$$

with α_{ps} ($\alpha^{\dagger}_{ps}$) the annihilation (creation) operator of a fermion in the $p-$th degenerated

state of the s level. This definition allows us to write LMG Hamiltonian

$$H = \frac{\epsilon}{2}\sum_{ps} s\alpha^{\dagger}_{ps}\alpha_{ps} + \frac{\mu}{2}\sum_{pp's}\alpha^{\dagger}_{ps}\alpha^{\dagger}_{p's}\alpha_{p'-s}\alpha_{p-s} + \frac{\nu}{2}\sum_{pp's}\alpha^{\dagger}_{ps}\alpha^{\dagger}_{p'-s}\alpha_{p's}\alpha_{p-s}. \tag{3.2}$$

The first term is the sum of single-particle energies, the second term account for the energy contribution due to the scattering between couples of particles in the same level while the third term describes a level swapping for a couple of particles with different s. The model is a naive example of a full connected graph, it is enough simple to be solved exactly for small N or numerically for large N, in fact thanks to the symmetries of the system allows one to reduce the size of the largest matrix to be diagonalized, but at the same time and allows one to test the goodness of many approximations techniques Pan & Draayer (1999); Rosensteel et al. (2008) tested accurately for first-neighbors model, as well could serve as test to analyze analogies and difference between classical and quantum phase transitions Castaños et al. (2006).

The Hamiltonian in Eq.(3.2) may be rewritten in terms of collective angular momentum operators defined by

$$\begin{aligned} S_z &= \frac{1}{2}\sum_{ps} s\,\alpha^{\dagger}_{ps}\alpha_{ps} \\ S_+ &= \sum_{p}^{N}\alpha^{\dagger}_{p+1}\alpha_{p-1} \qquad S_- = S^{\dagger}_+ \end{aligned} \tag{3.3}$$

and introducing new parameters, more common in condensed matter physics,

$$\begin{aligned} \nu &= -\frac{1}{N}(1+\gamma) \\ \mu &= \frac{1}{N}(1-\gamma) \\ \epsilon &= -2h \end{aligned} \tag{3.4}$$

leading to Ulyanov & Zaslavskii (1992)

$$\begin{aligned} H = &-\frac{1}{N}(1+\gamma)(S^2 - S_z^2 - \frac{N}{2}) \\ &-\frac{1}{2N}(1-\gamma)(S_+^2 + S_-^2) - 2h\,S_z\,. \end{aligned} \tag{3.5}$$

For clarity we have to specify that a constant irrelevant energy shift has been omitted, but this will not modify the results that we will derive. Finally, upon writing the collective spin operators S ads a sum of single spin operators

$$S_\alpha \equiv \frac{1}{2}\sum_{k=1}^{N}\sigma_\alpha^k\,, \tag{3.6}$$

we may rewrite the LMG Hamiltonian

$$H = -\frac{1}{N}\sum_{j<k}(\sigma_x^j\sigma_x^k + \gamma\sigma_y^j\sigma_y^k) - h\sum_{k}^{N}\sigma_z^k \tag{3.7}$$

where σ_α^k is the Pauli matrix associated to the direction $\alpha = x, y, z$ of the k-th spin. Having written the Hamiltonian in this new fashion we can instantaneously recognize that it belongs to the class of Hamiltonian acting on the space of N interacting spin $\frac{1}{2}$ systems in an external magnetic field. The sum is extended over all the spins, thus describing a system where the interaction is not limited to first neighbors. The first term in Eq.(3.7) introduces a spin-spin interaction whose strength is made anisotropic in the xy plane by the γ parameter, which could be thought as the ratio between the coupling energies in these directions, the isotropic case is recovered imposing $\gamma = 1$ means no anisotropy. Finally the parameter h describes the strength of the interaction among each spin and the external field.

Let us now focuse on some interesting symmetries of the system. At first we notice that the swap $h \to -h$ modifies the Hamiltonian as the (unitary) operations of describing *spin flip*, i.e. $U = \bigotimes_{k=1}^{N} \sigma_x^k$

$$H(\gamma, h) = U^\dagger H(\gamma, -h) U \tag{3.8}$$

so that we can analyze only the $h < 0$ semi-plane, since the eigenvalues here are the same as in the $h > 0$ case, and the eigenvectors are related by the transformation matrix U. Similarly, the γ parameter may be taken in the range $[-1, 1]$ since any map sending this range into $(-\infty, -1] \bigcup [1, \infty]$ modifies the Hamiltonian as a $\pi/2$ rotation around the axis parallel to the magnetic field, i.e. as the unitary $V = \bigotimes_{k=1}^{N} \sigma_z^k$ together with a rescaling of the field

$$H(\frac{1}{\gamma}, h) = V^\dagger \, H(\gamma, h\gamma) \, V \, . \tag{3.9}$$

The parameter space is therefore restricted to $(\gamma, h) \in [-1, 1] \times [0, \infty)$.

The LMG model spectrum has been extensively studied in the thermodynamic limit Dusuel & Vidal (2004, 2005); Wichterich et al. (2010); Ribeiro et al. (2007, 2008); Botet et al. (1982); Botet & Jullien (1983). Following the method suggested in Dusuel & Vidal (2004) the spectrum of H in the large N limit is computed using first a Holstein-Primakoff bosonization

$$\begin{aligned} S_+ &= N^{1/2}(1 - a^\dagger a/N)^{1/2} a \quad S_- = S_+^\dagger \\ S_z &= N/2 - a^\dagger a, \end{aligned} \tag{3.10}$$

and considering at most term in $(1/N)^0$ in the expansion of the square root. Subsequently in order to diagonalize H a Bogoliubov transformation is performed

$$a = \cosh\Theta \, b + \sinh\Theta \, b^\dagger \tag{3.11}$$

where $\Theta \equiv \Theta(\gamma, h)$ is chosen such that the Hamiltonian reads (neglecting a constant energy shift)

$$H \overset{N \gg 1}{=} \Delta(\gamma, h) \, b^\dagger b. \tag{3.12}$$

The study of the ground state reveals two phases in the parameter space: for $h \geq 1$ the system shows an ordered phase with

$$\Delta(\gamma, h) = 2 \left[(h-1)(h-\gamma) \right]^{1/2}$$

while for $0 \leq h < 1$ we have a disordered (broken) phase with an energy spacing among levels given by

$$\Delta(\gamma, h) = 2 \left[(1-h^2)(1-\gamma) \right]^{1/2} .$$

3.3 Estimation of anisotropy

As fore mentioned the interaction described by the LMG model depends on two relevant parameters: the anisotropy γ and the external field h. When we allow the interaction and consequently energy exchange of the spin system with its surrounding environment the temperature adds to the previous two. Among these parameters, the external field may be tuned by the experimenter and represents a tool that allows ones to exploit the systems criticality as a resource to reliably estimate the remaining less controllable parameters.

The anisotropy is a typical quantum parameter, because varying it we modify either the eigenvalues and the eigenvectors of the system. Anisotropy is not tunable by the experimenter, since it is part of the intrinsic coupling among spins and represents a specific characteristic of the system.

However anisotropy *is not* an observable, hence we cannot construct an operator corresponding to it. Its characterization may be addressed only by the metrological tools and the quantum estimation theory.

We consider chains in thermal equilibrium with their environment so the map from parameters space to quantum states is thus given without any costs by the canonical Gibbs density matrix

$$\rho(\gamma,h,\beta)=\frac{e^{-\beta H(\gamma,h)}}{Z(\gamma,h,\beta)}=\sum_n \frac{e^{-\beta E_n(\gamma,h)}}{Z(\gamma,h,\beta)}\,|n\rangle\langle n|\,, \tag{3.13}$$

where $Z(\gamma,h,\beta)=\mathrm{Tr}[e^{-\beta H}]$ is the canonical partition function, $E_n(\gamma,h)$ the n-th eigenvalue of the Hamiltonian, and $|n\rangle$ a basis where H is diagonal. The density matrix $\rho(\gamma,h,\beta)$ obtained has eigenvalues equal to the Boltzmann weights

$$B_n\equiv B_n(\gamma,h,\beta)=\frac{e^{-\beta E_n(\gamma,h)}}{Z(\gamma,h,\beta)} \tag{3.14}$$

In order to evaluate the quantum Fisher information for γ, which will give us the bounds to precision in its estimation, we have to find its eigenvalues and eigenvectors as a function of γ and h and insert them in Eq. (1.68). To gain some insight into the role of the chain size while maintaining the approach analytic, we will start analyzing in details the cases $N=2,3,4$ and then we will address the complementary thermodynamic limit $N\to\infty$ in Sec.3.8.

Using the results obtained in sec.1.3 and the eigenvalues and eigenvectors computed (for the results of the diagonalization see Appendix A), we can derive the Quantum Fisher Information $G_\gamma\equiv G_\gamma(\gamma,h,\beta)$. For a dimer constitute of $N=2$ spins an explicit expression is easily derivable and it is given by

$$G_\gamma=\frac{1}{r^2}\left[\beta^2\,\frac{\kappa_1}{2\kappa_2}+\frac{16h^2}{r^2}\frac{(1-e^{\beta r})^2}{(1+e^{\beta r})\sqrt{\kappa_2}}\right], \tag{3.15}$$

where

$$\begin{aligned}\kappa_1=&e^{-\frac{1}{2}\beta(v-r)}\Big[\frac{1}{2}(u-r)^2+4(8h^2+u^2)e^{\frac{1}{2}\beta(v+r)}\\&+\frac{1}{2}(u-r)^2e^{\beta(v+r)}+\frac{1}{2}(u+r)^2e^{\beta r}+\frac{1}{2}(u+r)^2e^{v\beta}\Big]\\ \kappa_2=&\left[1+e^{\beta r}+e^{\frac{1}{2}\beta(v+r)}+e^{-\frac{1}{2}\beta(v-r)}\right]^2\end{aligned}$$

having imposed $u = \gamma - 1$, $v = \gamma + 1$ and $r = \sqrt{u^2 + 16h^2}$. In contrast the analytical expression for the $N = 3$ and $N = 4$ cases are quite cumbersome and we do not report them.

When the temperature is fixed the optimal estimation of the anisotropy is achieved by tuning appropriately the external filed h, what we have to do is to maximize the Quantum Fisher Information over the external field h. the maximization procedure leads to optimal values of the field corresponding to the *critical lines* of the model, i.e. expression $h(\gamma)$ of the magnetic field in function of the anisotropy parameter. They correspond to region where the ground state and the first excited state are degenere. The expression for the finite site chains are:

$$N = 2 \to h_c = \frac{\sqrt{\gamma}}{2} \tag{3.16}$$

$$N = 3 \to h_c = \frac{2\sqrt{\gamma}}{3} \text{ and } h_c = 0 \tag{3.17}$$

$$N = 4 \to h_c = \frac{\sqrt{\gamma}}{4} \text{ and } h_c = \frac{3\sqrt{\gamma}}{4}\,. \tag{3.18}$$

For $N = 2$ the maximized Quantum Fisher Information $G_\gamma(\gamma, \frac{1}{2}\sqrt{\gamma}, \beta)$ is given by

$$G_\gamma^{\text{opt}} = \frac{8\gamma + \kappa^2 + \gamma(\gamma\kappa^2 - 8)\,\text{sech}^2\frac{1}{2}\kappa}{4(1+\gamma)^4} \tag{3.19}$$

where $\kappa = \beta(1+\gamma)$. In the low temperature regime, i.e. $\beta \gg 1$ we may write

$$G_\gamma^{\text{opt}} \simeq \beta^2 \frac{(u+r)^2}{8r^2} \begin{cases} e^{\frac{1}{2}\beta(v-r)} & h \geq \sqrt{\gamma}/2 \\ e^{-\frac{1}{2}\beta(v-r)} & h < \sqrt{\gamma}/2 \end{cases}\,. \tag{3.20}$$

We notice now that the exponent is equal to the energy gap between the two lowest energy eigenvalues and obviously it vanishes on the degeneracy line. For $N = 4$ the absolute maximum corresponds to $h_c = \frac{3\sqrt{\gamma}}{4}$ while for $N = 3$ also the condition $h = 0$ individuates a degenerated GS, but this does not correspond to a maxima of the Quantum Fisher Information for some reasons that we will clarify in the following section.

The role of criticality is illustrated in details in Fig. 3.1 for the 2 qubit case and Fig. 3.2,Fig. 3.3 for the 3 and 4 spins cases respectively, where we show G_γ as a function of γ and h for different values of the inverse temperature β. As it is apparent from the plots, when we decrease the temperature G_γ diverges as β^2 along the critical lines, whereas in any other point of the parameter space it maintains a finite value. To summarize what is shown in the plot, for any value $\gamma \geq 0$ it is always possible to find a value of the external field, as stated before an optimal value, which drives the system into the degeneracy lines, i.e. into critical points. In this way, one maximizes the Quantum Fisher Information and, in turn, optimize the estimation of γ. This results confirm that a systems guided into a critical region is in general a resource for metrological procedures. We remark here that the degeneracy line at $h = 0$ line for $N = 3$ is an exception, in fact there is no gain in precision even if a crossing between the two lowest energy states is present. We will address this issue and clarify the point in the following subsection.

3.4 A two-level approximation to assess estimation of anisotropy in the low temperature regime

An intuitive understanding of our results may be achieved approximating the Gibbs states to the Landau-Zener scheme, viz. considering only the two lowest levels of the

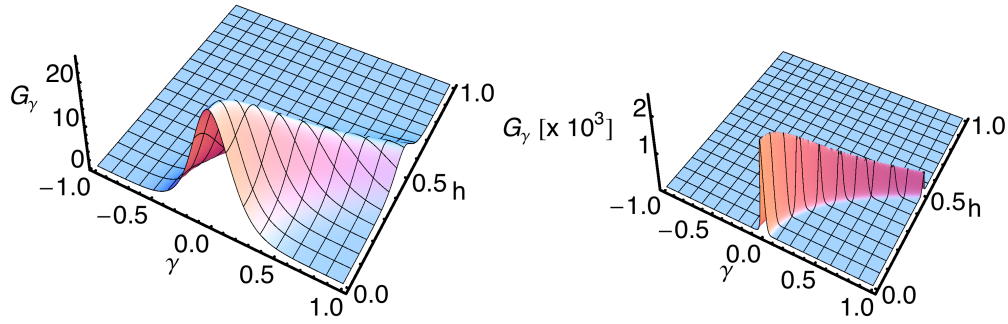

Figure 3.1: Estimation of anisotropy in the LMG model with $N = 2$ sites. The plots show the Quantum Fisher Information G_γ for the anisotropy as a function of the anisotropy parameter γ itself and of the magnetic field h for two values of β. The panels of the left refer to $\beta = 10$ while those on the right to $\beta = 100$. Comparing the two plots it is clear that G_γ reaches its maximum along the critical lines of the system as β^2, with such divergence modulated also by a non trivial function of γ.

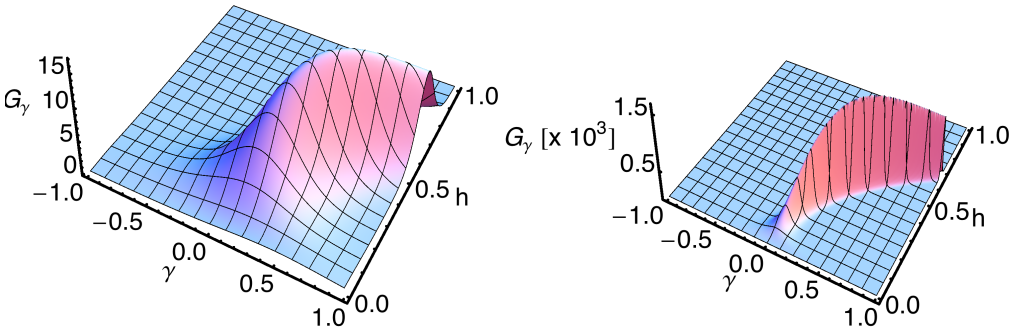

Figure 3.2: Estimation of anisotropy in the LMG model with $N = 3$ sites. The plots show the Quantum Fisher Information G_γ for the anisotropy as a function of the anisotropy parameter γ itself and of the magnetic field h for two values of β. The panels of the left refer to $\beta = 10$ while those on the right to $\beta = 100$. Note the peculiar absence of divergence in the N=3 case for h=0.

system

$$\rho(\gamma, h, \beta) \propto e^{-\beta E_0}|0\rangle\langle 0| + e^{-\beta E_1}|1\rangle\langle 1| \tag{3.21}$$

with $E_{0,1}$ the lowest energy level of the Hamiltonian.

For the values of N considered above, the energy spectra of the Hamiltonians have a common structure: the two lowest eigenvalues, the ground state and the first excited level, cross each other but never cross with the other upper levels for any value of γ and h. This implies that for low temperature, or equivalently for β large enough, the Boltzmann weights corresponding to the smallest eigenvalues are the two leading contributions in the sum in Eq.(3.13) and the density matrix is well be approximated by the expression in Eq. (3.21). This approximation is more and more justified as far as the temperature decreases. We now proceed by noticing that for the two level states of (3.21), the contribution of the eigenvectors to $G(\gamma)$ does not contain any divergent term in γ, h or β , because they are smooth functions of the parameters and hence hence their derivative respect any of those parameters is a smooth function too. Actually, this is the

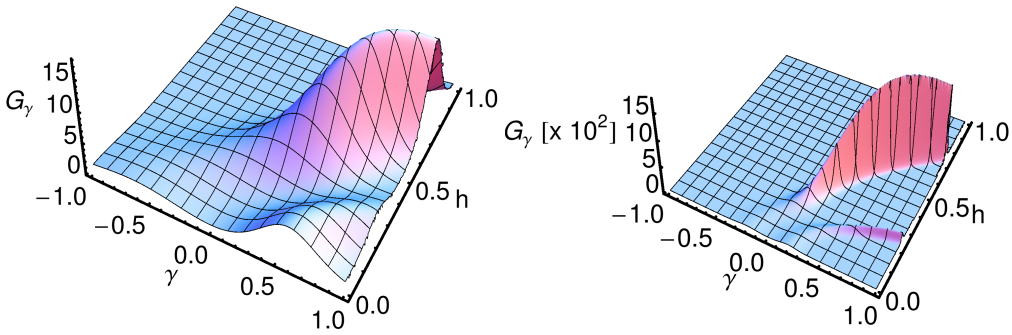

Figure 3.3: Estimation of anisotropy in the LMG model with $N = 4$ sites. The plots show the Quantum Fisher Information G_γ for the anisotropy as a function of the anisotropy parameter γ itself and of the magnetic field h for two values of β. The plot on the left side refer to $\beta = 10$ while those on the right to $\beta = 100$.

case also for other first-neighbour models Zanardi et al. (2008); Invernizzi et al. (2008), so that the approximation here described may apply to other models. In order to analyse the contribution due to the eigenvalues we introduce a general notation.

Let us consider a qubit whose eigenenergies are $f(a,b)$ and $g(a,b) = f(a,b) + x(a,b)$, depending on the parameters a and b (b may also be a *set* of parameters). Constructing as usual the thermal state, the Quantum Fisher Information for the parameter a rewrites

$$G_a(a,b,\beta) = \beta^2 \frac{e^{\beta x(a,b)}}{\left[1+e^{\beta x(a,b)}\right]^2} \left[\partial_a x(a,b)\right]^2 \tag{3.22}$$

It is easy to see that $G_a(a,b,\beta)$ diverges only in those points a_0 and b_0 such that $f(a_0,b_0) = g(a_0,b_0)$ and $\partial_a f(a_0,b_0) \neq \partial_a g(a_0,b_0)$. When this happens, Quantum Fisher Information is proportional to β^2. The two conditions are indeed satisfied on the degeneracy lines in eq.3.18, except for the case $N = 3$ and $h = 0$, where the partial derivatives of the eigenvalues are equal, this pure algebraic condition prevent the appearance of a divergence in the behaviour of the Quantum Fisher Information.

3.5 Achieving the ultimate bound to precision using feasible measurements

We have learned until now that the ultimate bound to precision for the estimation of anisotropy is set when the system is driven by the magnetic field in critical region. In order to reliably exploit this *quantum critical* enhancement we have to provide in principle an experimentally implementation of the measurement depicted by the symmetric logarithmic derivative. Since this control on a quantum state in quite unfair and since that any POVMs does not be related to a physical measurable quantity, generally the estimation procedure is based on realistic observables. This task is achieved evaluating the Fisher Information of the probability distribution of the measurement outcomes and to compare this function with the Quantum Fisher Information.

Dealing with a magnetic system, the natural choice for an observable is the total magnetization of the LMG system. We compute the corresponding Fisher information and we will compare it with its quantum counterpart. This two quantities become as similar

as approaching the critical region, thus showing that quantum critical enhancement of precision is indeed achievable in an an experimentally accessible scenario.

Given a basis $\otimes_{k=1}^{N} |m_z\rangle_k$ where $m_z \in 1, -1$ and $|x\rangle_k$ denotes the eigenvectors of the z spin component of the k-th spin, the total magnetization is diagonal in this basis. The corresponding eigenvalue is simply $\sum_{k=1}^{N} i = 2N_z - N$, where N_z is the number of spins up for a given basis element and the probability distribution of such measurement outcome, with the notation of Eq.(1.45), is given by

$$p(2N_z - N, \lambda) = \frac{\mathrm{Tr}\left[P_{N_z} \exp -\beta H\right]}{Z}, \tag{3.23}$$

where P_{N_z} denotes the projector onto the subspace spanned by the basis elements with N_z spins up. Finally, we substitute these probabilities in Eq. (1.45) computing the corresponding Fisher Information F_γ.

The explicit formulas for the F_γ are quite unhandy, so we do not report them. Rather, we will use the two level approximation which allows us to reproduce its main features. We anticipate that F_γ shares with the Quantum Fisher Information the nice behaviour in the critical region, i.e. it diverges as β^2 on the degeneracy lines, except for the case $h = 0$ line for $N = 3$.

Let us consider a two-dimensional system prepared in the mixed state

$$\rho(\lambda) = p|0\rangle\langle 0| + (1-p)|1\rangle\langle 1| \tag{3.24}$$

where both the eigenvalue p and the eigenvectors are functions of a parameter λ to be estimated. If a measurement of an observable $A = x_1|x_1\rangle\langle x_1| + x_2|x_2\rangle\langle x_2|$ is performed, the outcomes are distributed according to

$$P(x_i) = \mathrm{Tr}[\rho|x_i\rangle\langle x_i|] = p|\langle 0|\ x_i\rangle|^2 + (1-p)|\langle 1|\ x_i\rangle|^2, \tag{3.25}$$

where taking into account the normalization of the basis involved, we have the following relations

$$q = |\langle 0|\ x_1\rangle|^2 = |\langle 1|\ x_2\rangle|^2 \tag{3.26}$$

$$1 - q = |\langle 0|\ x_2\rangle|^2 = |\langle 1|\ x_1\rangle|^2 \tag{3.27}$$

We will also introduce the difference between the two transition amplitude

$$\delta q = q - (1-q) \tag{3.28}$$

$$\delta p = p - (1-p). \tag{3.29}$$

With this notation the FI for the generic observable A is rewritten in a compact form as

$$\mathrm{F}(\lambda) = \frac{(\partial_\lambda p\ \delta q + \partial_\lambda q\ \delta p)^2}{(p\ \delta q - q)(p\ \delta q + 1 - q)} \tag{3.30}$$

In the case of our interest the population of the density matrix are the Boltzmann weights

$$1 - p = \exp(-\beta\epsilon)/Z \tag{3.31}$$

where $\epsilon = \epsilon(\gamma, h)$ denotes the energy of the first excited level. Without lost of generality we can assume the energy of the ground state is set to be zero, we thus arrive at

$$\partial_\gamma p = \frac{\beta\, e^{\beta\epsilon}}{\left[1 + e^{\beta\epsilon}\right]^2} \partial_\gamma \epsilon\,. \tag{3.32}$$

Eq. (3.32) implies that the FI F_γ of any observable of the form $A = x_1|x_1\rangle\langle x_1| + x_2|x_2\rangle\langle x_2|$ diverges as β^2 in the large β limit, provided that $\delta q \neq 0$. This in terms of statical distinguishability of quantum states means that this kind of measurement may discriminate the two eigenstates and $\partial_\gamma \epsilon \neq 0$, in a similar way we found for the Quantum Fisher Information and that $\epsilon = 0$, i.e. that we are at a critical point.

The above model is basically the same we used to explain the results obtained for the Quantum Fisher Information and it is valid to discuss the estimation performances of the total magnetization, but cannot be used to approximate the FI of *any* observable A of the LMG model in the limit of low temperature. Even though the state of the system may be always approximated by a qubit, there is no evidence for which a general observable may be reduced to an operator acting on smaller Hilbert space.

3.6 LMG critical systems as quantum thermometers

Looking at Eq. (3.13) one can easily notice that temperature influences only the eigenvalues of the density matrix, but it does not affect the behaviour of its eigenvectors. For this motivation only the classical contribution to the Quantum Fisher Information $G(\beta)$ survives, i.e. the sum depending on the Boltzmann weights in the general expression for Quantum Fisher Information of Eqs.(1.65). We thus can calculate

$$G_\beta(\gamma, h, \beta) = \sum_{n=1}^{d} \frac{(\partial_\beta B_n)^2}{B_n}, \tag{3.33}$$

where B_n denotes the n-th Boltzmann weight. It is worth underlining that $G_\beta(\gamma, h, \beta)$ is equal to the energy fluctuations mean value over the ensemble, infact

$$\begin{aligned} G_\beta(\gamma, h, \beta) &= \sum_{n=1}^{d} \frac{(\partial_\beta B_n)^2}{B_n} = \\ &= \sum_{n=1}^{d} B_n (E_n^2 + (\partial_\beta \ln Z)^2 + E_n \partial_\beta \ln Z) = \\ &= \overline{E^2} - \overline{E}^2 = \overline{\Delta E^2} \end{aligned} \tag{3.34}$$

Our interest now is to assess how chains with $N = 2, 3, 4$ described by a Lipkin Meshkov Glick hamiltonians could be used as quantum thermometers. In order to accomplish to this task we evaluate the Quantum Fisher Information for the inverse temperature β and maximize its value by tuning the external field. The optimal values of the field maximizing the Quantum Fisher Information are shown in Figs. 3.4,3.5 and 3.6 as a function of the anisotropy for different values of β and for the different sizes of the chain. In this case we report a different situation in comparison to what happened for the estimation of the anisotropy. In fact the optimal values of the field h^* do not correspond to the critical ones, but a clear connection between optimal and critical lines exists. Several *optimal* lines are present for each *critical* line, correspondingly to slightly larger or smaller values of the field. As the inverse temperature is increased, the optimal lines are deformed, converging to the corresponding critical one either above or below. This link between critical and optimal lines will be examined in more details later in this section.

The optimal values of the field maximizing the Quantum Fisher Information are shown in Fig. 3.4 for the dimer while in Fig.3.5 for the trimer and in Fig.3.6 for the

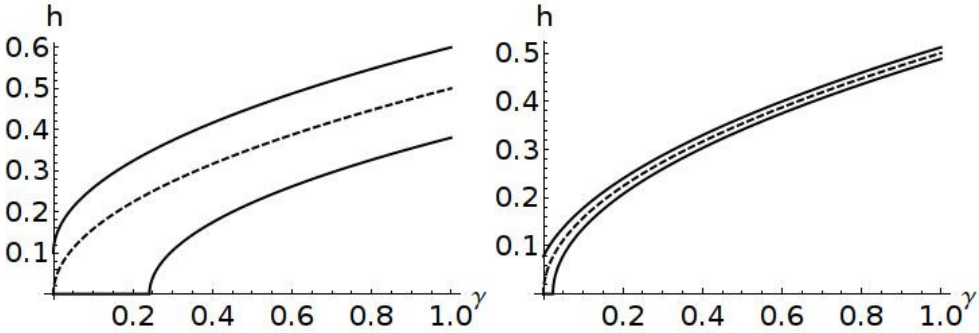

Figure 3.4: Quantum thermometry using LMG systems for $N = 2$. The plots show the optimal field h^*, maximizing the Quantum Fisher Information G_β, as a function of the anisotropy of the system for different values of β and for different lengths of the LMG chain. The two left column correspond to $\beta = 10$ whilst the right to $\beta = 100$. The optimal values of the field are the solid lines whereas the dashed lines are the critical lines h_c of Eq. (3.18).

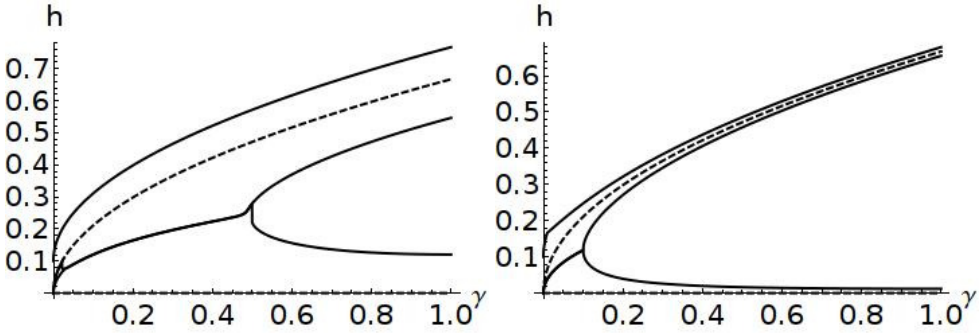

Figure 3.5: Quantum thermometry using LMG systems for $N = 3$. The plots show the optimal field h^*, maximizing the Quantum Fisher Information G_β, as a function of the anisotropy of the system for different values of β and for different lengths of the LMG chain. The two left column correspond to $\beta = 10$ whilst the right to $\beta = 100$. The optimal values of the field are the solid lines whereas the dashed lines are the critical lines h_c of Eq. (3.18).

4 qubit case as a function of the anisotropy for different values of β. In this case we report a different situation in comparison to what happened for the estimation of the anisotropy. In fact the optimal values of the field h^* do not correspond to the critical ones, but a clear connection between optimal and critical lines exists. Several *optimal* lines are present for each *critical* line, correspondingly to slightly larger or smaller values of the field. As the inverse temperature is increased, the optimal lines are deformed, converging to the corresponding critical one either above or below. This link between critical and optimal lines will be examined in more details later in this section.

As for the previous estimation of the anisotropy γ an explicit expression of the Quantum Fisher Information $G_\beta(\gamma, h^*, \beta)$ could be easily given for the $N = 2$ chain

$$G_\beta = \frac{1}{2}\frac{\kappa_3}{\kappa_4} \tag{3.35}$$

where

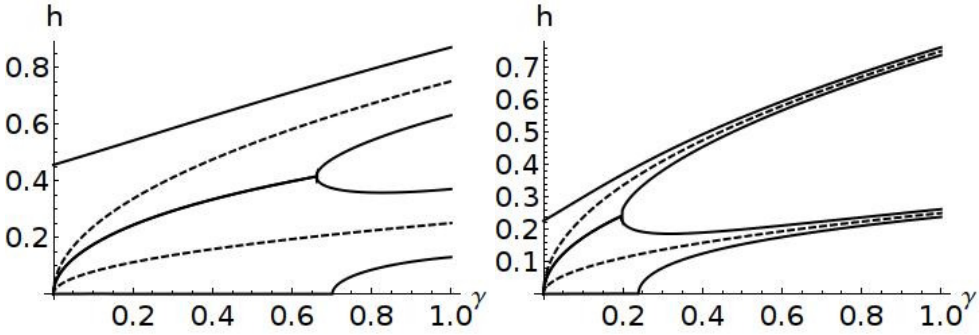

Figure 3.6: Quantum thermometry using LMG systems for $N = 4$. The plots show the optimal field h^*, maximizing the Quantum Fisher Information G_β, as a function of the anisotropy of the system for different values of β and for different lengths of the LMG chain. The two left column correspond to $\beta = 10$ whilst the right to $\beta = 100$. The optimal values of the field are the solid lines whereas the dashed lines are the critical lines h_c of Eq. (3.18).

$$\begin{aligned}\kappa_3 =& e^{\frac{1}{2}\beta(v+r)}\Big[\frac{1}{2}(v+r)^2 + 4(1+8h^2+\gamma^2)e^{\frac{1}{2}\beta(v+r)} + \\ & \frac{1}{2}(v-r)^2 e^{\beta(v+r)} + \frac{1}{2}(v+r)^2 e^{\beta r} + \frac{1}{2}(v+r)^2 e^{\beta v}\Big] \\ \kappa_4 =& \Big[e^{\frac{1}{2}\beta v} + e^{\frac{1}{2}\beta r} + e^{\frac{1}{2}\beta(v+2r)} + e^{\beta(v+\frac{1}{2}r)}\Big]^2 ,\end{aligned}$$

with v and r as in Eq. (3.15). Analogue expressions, with several more terms, are obtained for $N = 3$ and $N = 4$: we are not showing the explicit expressions here, anyway when the temperature approaches zero Eq. (3.35) may be rewritten as

$$G_\beta \simeq \frac{1}{4}(v-r)^2 \begin{cases} e^{\frac{1}{2}\beta(v-r)} & h \geq \sqrt{\gamma}/2 \\ e^{-\frac{1}{2}\beta(v-r)} & h < \sqrt{\gamma}/2 \end{cases} , \tag{3.36}$$

where, as in Eq. (3.20), the exponent is the energy gap between the two lowest energy levels.

The Quantum Fisher Information behaviour, is shown in Fig. 3.7 as a function of the anisotropy and of the external field for different values of β and for the number of sites. The first think that should be noticed is that the presence of optimal lines clearly emerges from the plot. The Quantum Fisher Information, G_β decreases with β for any value of the anisotropy and external field. A simple explanation could be provided considering that as temperature decreases $\rho(\gamma, h, \beta)$ approaches the projector on the ground state space and being this projector as any other eigenstate independent on the temperature, the Quantum Fisher Information vanishes.

On the other hand, the quantitative features of the decay, that is how fast the optimal G_β tends to zero, are strongly influenced by the criticality of the system. Indeed, outside the critical regions the Quantum Fisher Information vanishes exponentially, whereas along the optimal lines it vanishes as $\frac{1}{\beta^2}$ independently on γ. When lowering the temperature two interesting phenomena occur. The first one is that the optimal lines approach the critical ones, $h^* \to h_c$; secondly the Quantum Fisher Information G_β is independent on the number of lattice sites, i.e. Eq. (3.36) may generalized to $N = 3, 4$ and rewritten

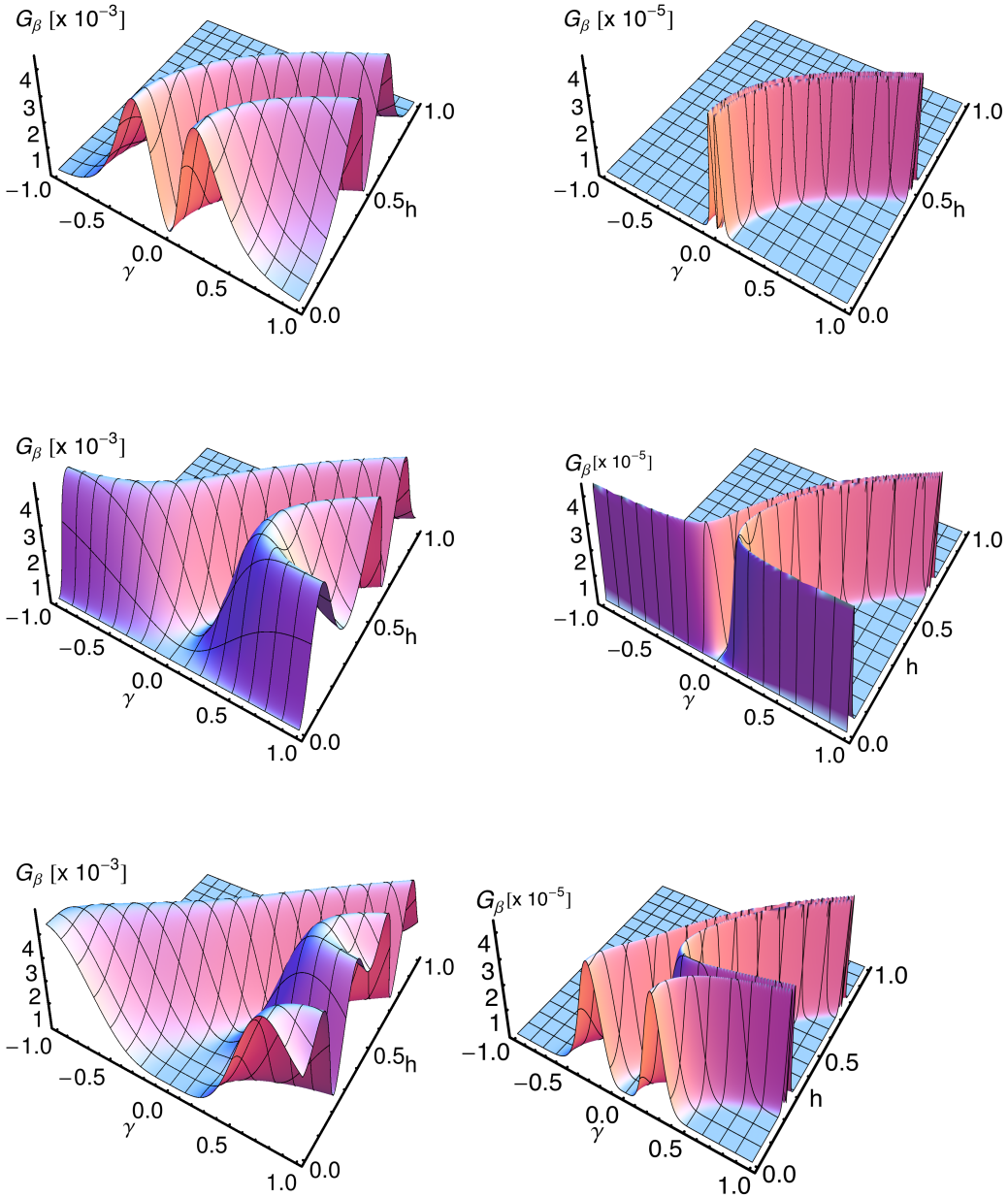

Figure 3.7: Quantum thermometry using LMG systems. The plots show G_β versus γ and h for different β and number of sites. The three rows report results for $N = 2, 3, 4$ respectively. The two columns refer to $\beta = 10$ and $\beta = 100$.

as

$$G_\beta \simeq k(\gamma, h) e^{-\beta\, f(\gamma,h)} \tag{3.37}$$

where the functions $k(\gamma, h)$ and $f(\gamma, h)$ are non negative, independent on β and zero only on the critical/optimal lines. Overall, we argue that the presence of degeneracy, i.e. crossing between the lowest eigenvalues, allow us to find optimal fields where G_β decreases as $1/\beta^2$, and such enhancement is due to criticality.

In order to confirm this intuition and to gain more insight on the Quantum Fisher Information behaviour in the low temperature regime we again consider the two-level approximation used before. Using the notation of Eq. (3.22), the Quantum Fisher Information rewrites

$$G_\beta(a,b,\beta) = \frac{e^{\beta x(a,b)}\left[\beta x(a,b)\right]^2}{\left[1+e^{\beta x(a,b)}\right]^2}\frac{1}{\beta^2} = \frac{F(\beta x(a,b))}{\beta^2}\,, \tag{3.38}$$

where $F(y)$ is a symmetric function vanishing in the origin, $F(0) = 0$, and it shows two global maxima at $y = \pm y_{opt}$. This explains the behaviour shown in Fig. 3.4 and 3.7 where for each critical line, i.e. $x(a,b) = 0$, two optimal lines are present, corresponding to $\beta x(a,b) = \pm y_{opt}$. Moreover, the dependence of $F(y)$ on the product of β with $x(a,b)$ clarifies why, as β increases, the optimal lines approach the critical ones. Finally, we see that on the optimal lines the Quantum Fisher Information vanishes as $1/\beta^2$ independently on any parameter, since the maximization of $F(y)$ factored out the parameter dependence. In other words, the precision is basically governed by the energy gap between the two lowest energy levels. This behaviour, in the limit of large β, is independent on the actual model, so that the argument may be equally employed to describe any system with an energy spectrum made of two crossing lowest levels well separated from the other levels.

We finally emphasize that the ultimate bound to precision may be practically achieved, since, as shown by Eq. (3.34) the SLD turns out to be the total energy of the system, which we assume to be measurable.

3.7 Robustness against fluctuations of the external field

The results reported in the previous paragraphs shows that criticality is a resource for quantum metrology in LMG systems. As it has been extensively discussed, in order to achieve the ultimate bounds to precision we should be able to tune the magnetic field to the appropriate value ,i.e. h_c for the estimation of the anisotropy or h_o for the estimation of the inverse temperature, driving the system towards the critical region. A question thus arises on whether and how an imprecise tuning of the external field affects the metrological performances of the system.

This issue basically amounts to a perturbation analysis in order to discuss the robustness of the optimal estimators against fluctuations of the external field. The canonical approach to attack this problem would be that of considering the state of the system as a mixture of different ground states, each one corresponding to a different value of the external field, and then evaluating the quantum Fisher information for this family of states. This is a very challenging procedure to pursue, even numerically, and some approximated approach should be employed instead. In fact, it is possible to provide an estimate of this effect by averaging the Quantum Fisher Information over a given distribution for the external field: this is an approximation since the Quantum Fisher Information is a non linear function of the density operator, but it is not a crude one, owing to the small value of fluctuations that we should consider for this kind of perturbation analysis.

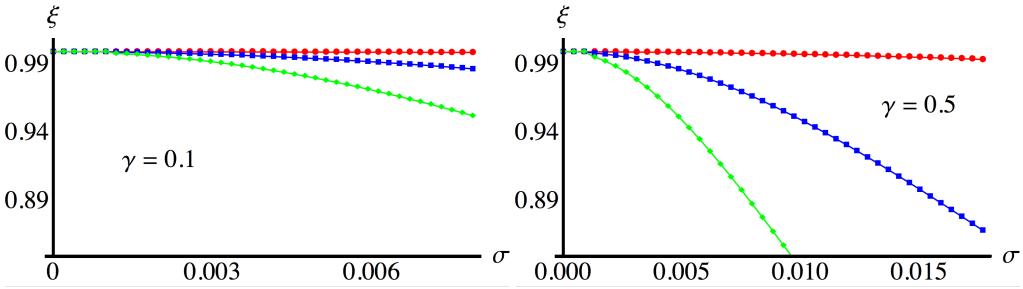

Figure 3.8: The ratio $\xi = \overline{G}_\gamma(\beta)/G_\gamma(\gamma, h_c, \beta)$ between the field-averaged Quantum Fisher Information and the optimal one as a function of the width Σ of the field distribution. The upper panel show results for $\gamma = 0.1$ and the lower one for $\gamma = 0.5$. In both panels we show the behaviour for $\beta = 5$ (red points), $\beta = 25$ (blue squares), and $\beta = 50$ (green diamonds).

In order to obtain a quantitative estimate we assume that the actual value of the external field is normally distributed around the optimal one h_c, and evaluate the averaged Quantum Fisher Information for the anisotropy

$$\overline{G}_\gamma(\beta) = \int dh\, G_\gamma(\gamma, h, \beta)\, g_\Sigma(h) \tag{3.39}$$

as a function of the width Σ of the Gaussian $g_\Sigma(h)$, viewed as a convenient measure of the fluctuations (i.e. of the imprecise tuning) of the external field. In particular, we choose the range of Σ as to describe an imprecise tuning of the external field up to $\pm 5\%$. In Fig. 3.8 we show the ratio between the field-averaged Quantum Fisher Information and the optimal one

$$\xi = \frac{\overline{G}_\gamma(\beta)}{G_\gamma(\gamma, h_c, \beta)}\,, \tag{3.40}$$

as a function of the of the width Σ of the Gaussian distribution, for different value of γ and for different temperatures. Looking at the plots becomes clear that the ratio is close to unit,this is a signature of the robustness of the optimal estimator. The plots also show that the detrimental effects of an imprecise tuning of h increase with γ and decrease with temperature. Analogue results may be obtained for $N = 3$ and $N = 4$ as well as for the estimation of temperature. Overall, we have that the optimal estimators are robust against possible fluctuations of the external field, thus providing a realistic benchmark for precision measurements on LMG systems.

3.8 Quantum estimation in large LMG system: the thermodynamical limit

The study of the thermodynamical limit of the model could be conducted using the diagonal form of the Hamiltonian in Eq.(3.12). The family of quantum states we are dealing with may be expressed as the unitary evolution of the density matrix we have used until now

$$\rho_\Theta = U_\Theta \rho(\gamma, h, \beta) U_\Theta^\dagger \tag{3.41}$$

where the operator $U_\Theta = \exp\left(-i\Theta(\gamma, h)G\right)$ is a unitary, $G \equiv (a^2 + a^{\dagger 2})$ is the Hermitian operator related to the Bogolyubov transformation in Eq.(3.11). This let us to compute

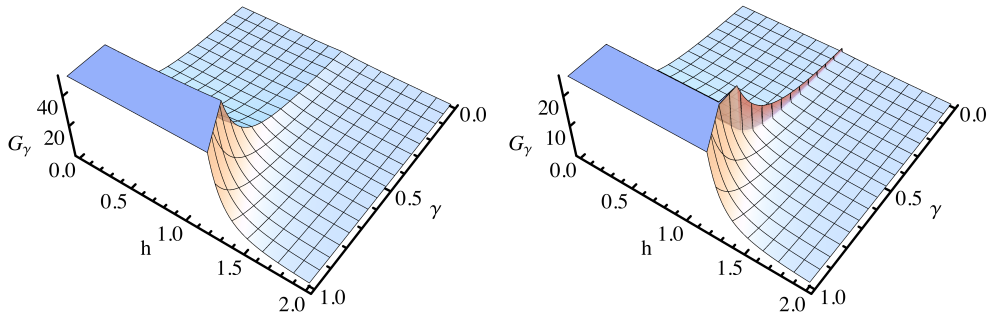

Figure 3.9: Characterization of anisotropy in the thermodynamical limit. The plots show the behaviour of G_γ for the LMG model as function of the anisotropy parameter γ and the external magnetic field h. The left panel refers to $\beta = 1$ and the right one to $\beta = 10^5$.

the Quantum Fisher Information for anisotropy G_γ and temperature G_β using Eq.(1.68), where the parameter λ turns out to be in the first case γ and in the second the inverse temperature β. It is useful to underline that, in the limit of an infinite number of particle the sum in Eq.(1.68) is infinite thus leading to region where the quantum Fisher information is divergent.

We do not report here the analytic expressions of the Quantum Fisher Informations since they are quite cumbersome. Rather we discuss their behaviour analyzing their main features. In Fig. 3.9 we show G_γ as a function of the external field h and of the anisotropy γ itself. As it is apparent from the plot, in the ordered phase ($h > 1$) G_γ has a finite value everywhere, showing a cusp for h approaching the critical value. In the broken phase G_γ increases with γ showing a divergent behaviour approaching $\gamma = 1$ for all value of the magnetic field in the region, thus signaling the sudden change of universality class of the system. In both phases the scaling with the temperature on the critical regions goes as β^2. More specifically, we have

$$G_\gamma(\gamma, h^*, \beta) \simeq \frac{9}{4(h-1)^2} - \frac{25\beta^2}{12} + O(h), \tag{3.42}$$

in the orderd phase, $h > 1$ and

$$G_\gamma(\gamma, h^*, \beta) \simeq \frac{9}{4(\gamma-1)^2} - \frac{25\beta^2(h-1)}{6(\gamma-1)} + O(h)\,, \tag{3.43}$$

in the broken one, i.e. for $0 \leq h < 1$.

The evaluation of the quantum Fisher information for the temperature shows how it reaches is maximum, without showing divergences, along the degeneracy lines previously outlined, but this time it scales as β^{-2} at the first order near the critical field. If $h \geq 1$ we have

$$G_\beta(\gamma, h, \beta) \simeq \frac{1}{\beta^2} + \frac{1}{3}(\gamma-1)(h-1) + O(h^{\frac{3}{2}}) \tag{3.44}$$

instead in the other phase where $0 \leq h < 1$ we obtain

$$G_\beta(\gamma, h, \beta) \simeq \frac{1}{\beta^2} - \frac{2}{3}(\gamma - 1)(h - 1) + O(h^{\frac{3}{2}}) \,. \tag{3.45}$$

We notice that this results could be improved only going beyond the Gaussian approximation performed in Eqs.(3.10, 3.11) since in the broken phase region the effective separation between the degenerate ground state vanishes as $\exp(-N)$. As a matter of fact, it would be possible to recover the results obtained for the finite chain cases, i.e. divergences along $h^* \simeq \sqrt{\gamma}$, only looking at the fine structure of the level in the broken phase.

3.9 Conclusions

We have addressed quantum metrology in LMG model as a paradigmatic example of criticality-assisted estimation in systems with interaction beyond the first-neighbor approximation. In particular, we analyzed in details the use of criticality in improving precision of measurement procedures aimed at estimating the anisotropy of the system or its temperature.

Upon considering LMG systems in thermal equilibrium with the environment we have evaluated exactly the quantum Fisher information of small-size LMG chains made of $N = 2, 3$ and 4 lattice sites and analyzed the same quantity in the thermodynamical limit by means of a zero-th order approximation of the system Hamiltonian. In this way we proved that quantum criticality of the system represents a resource in estimating the anisotropy. In fact, the quantum Fisher information G_γ is maximized at the critical lines, where, in the low temperature regime, it diverges as β^2, while being finite everywhere else. We have then shown that the ultimate bounds to precision may be achieved by tuning the external field and by measuring the total magnetization of the system.

We have also addressed the use of LMG systems as quantum thermometers showing that: i) precision is governed by the gap between the lowest energy levels of the systems, ii) field-dependent level crossing provides a resource to extend the operating range of the quantum thermometer. Our results are encouraging for the emergent field of quantum thermometry. Indeed, despite the fact that the Quantum Fisher Information G_β vanishes everywhere for decreasing temperature, criticality continues to represent resource: the Quantum Fisher Information is maximized along optimal lines approaching the critical ones for decreasing temperature, and there the optimal Quantum Fisher Information vanishes as $1/\beta^2$ instead of exponentially.

Finally, we have introduced a simple model, based on a two-level approximation of the system, which allows us to provide an intuitive understanding of our findings for both G_γ and G_β. Our model also suggests that similar behaviours may be expected for a larger class of critical systems with interaction beyond the first-neighbor approximation.

CHAPTER 4

Decoherence model for extended environment

This chapter is devoted to the microscopic description of the emergence of collective decoherence in extended systems. In the first section we introduce a dissipative model in d-dimension for a system constituted by two harmonic oscillators and we derive the master equation and the coefficients describing their damping. Then in the following two sections we study how the dimension of the bath affect the two probes decoherence. In the last two section we compare the correlation distance of the bath with the cross damping of the two probes and we remark the physics behind different ways the system decoheres.

4.1 Dissipative Model

A strong limitation in pursuing a feasible realization of quantum technologies is the lack of deep knowledge of how a system degrades its quantum features in its surrounding environment. Learning how to treat the decohering abilities of a bath, where a quantum system is merged, has a broad field of application ranging from quantum optics, where it was first observed, to novel bio-chemical application Fassioli et al. (2010). Despite those tricky losses it has been shown that a couple of spatially separated quantum systems, such as two-level systems Benatti et al. (2003) or harmonic oscillators (H.O.)Paz & Roncaglia (2008), could entangle by means of an interaction with a bath; in particular the environment plays an active role when the eigenstate of one collective degree of freedom of the systems belongs to a Decoherence-Free Subspace. The entanglement limitation Doll et al. (2006) or generation Zell et al. (2009) studied in terms of the distance between the systems offers a dichotomous approach to the systems-bath interaction: they can be considered plugged to the same bath or to different reservoirs Galve et al. (2010); Wolf et al. (2011); Giorgi et al. (2012).

Besides these detrimental consideration a new way to turn in advantage the unavoidable environmental noise has been proposed in the framework of the quantum computation and quantum state engineering Verstraete et al. (2009); Diehl et al. (2008); Kraus et al. (2008).

We considera D-dimensional harmonic crystal with nearest neighbour interactions, i.e a crystal consisting on an infinite collection of harmonically coupled masses ($\hbar = m = 1$) with on-site harmonic potential of frequency ω_0 (see Fig. 4.1a for a representation of the bidimensional lattice) :

$$H_B = \sum_{\vec{n}} \frac{P_{\vec{n}}^2}{2} + \frac{\omega_0^2 Q_{\vec{n}}^2}{2} + \frac{g}{2} \sum_{\vec{l}} (Q_{\vec{n}} - Q_{\vec{n}+\vec{l}})^2 \tag{4.1}$$

where $\vec{n} \equiv (n_1, n_2, ...n_d)$ is the site index where each mass lies, and $\vec{l}$ are unit lattice vectors, being for a cubic structure $\vec{l} \in \{\hat{u}_x, \hat{u}_y, ..., \hat{u}_D\}$ in each of the D spatial directions. The environment dispersion relation

$$\omega(\vec{k}) = \sqrt{\omega_0^2 + 4dg(\sin^2 \frac{k_x}{2} + \sin^2 \frac{k_y}{2} + ... + \sin^2 \frac{k_d}{2})} \tag{4.2}$$

follows from the symmetries of the crystal.

This kind of model was firstly introduced in Rubin (1963) whose interest was to employ a linear harmonic chain as a microscopic model of an Ohmic bosonic bath Wolf et al. (2011); Vasile et al. (2014). This model allows to model spatially correlated dissipation and provides a common ground to assess the role of different crystal dimensionality D and geometries, including spatial disorder effects, either for point-like and for non-local system-bath interactions.

Now we can consider the system as two harmonic probes, that are firstly considered as point-like structures coupled to the bath at fixed points $\vec{n}$ and $\vec{n'} = \vec{n} + \vec{r}$, so the system-bath interaction is

$$H_{SB} = \lambda(q_1 Q_{\vec{n}} + q_2 Q_{\vec{n}'}), \tag{4.3}$$

Hence we can finally introduce the overall Hamiltonian given by

$$H = H_B + H_S + H_{SB}$$

where the extended system, as previously anticipated, consists of the two identical uncoupled harmonic probes of frequency Ω

$$H_S = \Omega(a_1^\dagger a_1 + a_2^\dagger a_2) \tag{4.4}$$

weakly interacting with the environment and located to different spatial locations $\vec{n}$ and $\vec{n'} = \vec{n} + \vec{r}$

The master equation of the system (two probes) density matrix up to the second order in the coupling strength, is obtained in the Born-Markov approximation Breuer & Petruccione (2002) and given by

$$\dot{\tilde{\rho}}(t) = -\int_0^t d\tau \mathrm{Tr}_B\{[\tilde{H}_{SB}(t), [\tilde{H}_{SB}(t-\tau), R_0 \otimes \tilde{\rho}_S(t)]]\} \tag{4.5}$$

in the interaction picture $\tilde{\rho}_S$, where $\tau = t' - t$ and

$$R_0 = \frac{\exp(-\beta H_B)}{Z_B}$$

the invariant thermal state of the crystalline environment.

The bath Hamiltonian is diagonalized through the plane wave transformation

$$Q_{\vec{n}} = (2\pi)^{-D/2} \int_{-\pi}^{\pi} d\vec{k}\, e^{i\vec{k}\,\vec{n}} Q_{\vec{k}} \tag{4.6}$$

into

$$H_B = \int_{-\pi}^{\pi} d\vec{k}\, \omega_{\vec{k}}\, A_{\vec{k}}^\dagger A_{\vec{k}} \tag{4.7}$$

where now $Q_{\vec{k}}$ is complex and, provided its conjugate momentum P, fulfills the commutation relation

$$[Q_{\vec{k}}, P_{-\vec{k}'}] = i\delta(\vec{k} - \vec{k}'), \tag{4.8}$$

and $Q^\dagger_{\vec{k}} = Q_{-\vec{k}}$. Its corresponding annihilation/creation operators read

$$Q_{\vec{k}} = \frac{A_{\vec{k}} + A^\dagger_{-\vec{k}}}{\sqrt{2\omega_{\vec{k}}}}, \tag{4.9}$$

so these operators satisfy the usual bosonic algebra $[A_{\vec{k}}, A^\dagger_{\vec{k}'}] = \delta(\vec{k}-\vec{k}')$. The system-bath Hamiltonians for the crystalline case is

$$H_{SB} = \int_{-\pi}^{\pi} d^D\vec{k}\, \frac{\lambda(2\pi)^{-D/2}}{2\sqrt{\Omega\,\omega_{\vec{k}}}} \left[(a_1 e^{i\vec{k}\vec{n}} + a_2 e^{i\vec{k}\vec{n}'})A^\dagger_{\vec{k}} + h.c.\right] \tag{4.10}$$

$$= \int d^D\vec{k} \frac{\lambda}{2\sqrt{\Omega\,\omega_{\vec{k}}}}(S^\dagger_{\vec{k}} A_{\vec{k}} + S_{\vec{k}} A^\dagger_{\vec{k}}), \tag{4.11}$$

with $S_{\vec{k}} = (2\pi)^{-D/2}(a_1 e^{i\vec{k}\vec{n}} + a_2 e^{i\vec{k}\vec{n}'})$. In the case of a crystal with disorder, translational invariance is broken and the bath is not any more diagonalized by plane waves, but by the general transformation

$$Q_{\vec{n}} = \int_{-\pi}^{\pi} d\vec{k}\, f_{\vec{n},\vec{k}} Q_{\vec{k}} \tag{4.12}$$

and the system operators read $S_{\vec{k}} = a_1 f_{\vec{n},\vec{k}} + a_2 f_{\vec{n}',\vec{k}}$.

We can derive the master equation for the system dynamics

$$\begin{aligned}
\dot{\tilde{\rho}}(t) = &- \int_0^t dt' \mathrm{Tr}_B \\
&\{[\tilde{H}_{SB}(t), [\tilde{H}_{SB}(t'), R_0 \otimes \tilde{\rho}(t')]]\} \\
&= -\int_0^t dt' \int_{-\pi}^{\pi} d^D\vec{k} d^D\vec{k}' \frac{\lambda^2(2\pi)^{-D}}{2\sqrt{(\Omega\,\omega_{\vec{k}})(\Omega\,\omega_{\vec{k}'})}} \mathrm{Tr}_B \big\{[\tilde{S}^\dagger(\vec{k},t)\tilde{A}(\vec{k},t), [\tilde{S}^\dagger(\vec{k}',t')\tilde{A}(\vec{k}',t'), R_0\otimes\tilde{\rho}(t')]] \\
&+ [\tilde{S}^\dagger(\vec{k},t)\tilde{A}(\vec{k},t), [\tilde{S}(\vec{k}',t')\tilde{A}^\dagger(\vec{k}',t'), R_0\otimes\tilde{\rho}(t')]] \\
&+ [\tilde{S}(\vec{k},t)\tilde{A}^\dagger(\vec{k},t), [\tilde{S}(\vec{k}',t')\tilde{A}^\dagger(\vec{k}',t'), R_0\otimes\tilde{\rho}(t')]] \\
&+ [\tilde{S}(\vec{k},t)\tilde{A}^\dagger(\vec{k},t), [\tilde{S}^\dagger(\vec{k}',t')\tilde{A}(\vec{k}',t'), R_0\otimes\tilde{\rho}(t')]]\big\}
\end{aligned} \tag{4.13}$$

When averaging on

$$R_0 = \bigotimes_{\vec{k}} \frac{e^{-\beta N_{\vec{k}}}}{Z_B}$$

the first and the third commutator vanish so we omit them immediately

$$\begin{aligned}\dot{\tilde{\rho}}(t) = &-\int_0^t dt' \int_{-\pi}^{\pi} d^D\vec{k}d^D\vec{k'} \frac{\lambda^2(2\pi)^{-D}}{2\sqrt{(\Omega\,\omega_{\vec{k}})(\Omega\,\omega_{\vec{k'}})}} \mathrm{Tr}_B \\ &\big\{\tilde{S}^\dagger(\vec{k},t)\tilde{A}(\vec{k},t)S(\vec{k'},t')\tilde{A}^\dagger(\vec{k'},t')R_0\otimes\tilde{\rho}(t') - \tilde{S}^\dagger(\vec{k},t)\tilde{A}(\vec{k},t)R_0\otimes\tilde{\rho}(t')\tilde{S}(\vec{k'},t')\tilde{A}^\dagger(\vec{k'},t') \\ &- \tilde{S}(\vec{k'},t')\tilde{A}^\dagger(\vec{k'},t')R_0\otimes\tilde{\rho}(t')\tilde{S}^\dagger(\vec{k},t)\tilde{A}(\vec{k},t) + R_0\otimes\tilde{\rho}(t')\tilde{S}(\vec{k'},t')\tilde{A}^\dagger(\vec{k'},t')\tilde{S}^\dagger(\vec{k},t)\tilde{A}(\vec{k},t) \\ &+ \tilde{S}(\vec{k},t)\tilde{A}^\dagger(\vec{k},t)\tilde{S}^\dagger(\vec{k'},t')\tilde{A}(\vec{k'},t')R_0\otimes\tilde{\rho}(t') - \tilde{S}(\vec{k},t)\tilde{A}^\dagger(\vec{k},t)R_0\otimes\tilde{\rho}(t')\tilde{S}^\dagger(\vec{k'},t')\tilde{A}(\vec{k'},t') \\ &- \tilde{S}^\dagger(\vec{k'},t')\tilde{A}(\vec{k'},t')R_0\otimes\tilde{\rho}(t')\tilde{S}(\vec{k},t)\tilde{A}^\dagger(\vec{k},t) + R_0\otimes\tilde{\rho}(t')\tilde{S}^\dagger(\vec{k'},t')\tilde{A}(\vec{k'},t')\tilde{S}(\vec{k},t)\tilde{A}^\dagger(\vec{k},t)\big\}\end{aligned} \tag{4.14}$$

We can collect the terms depending on the same bath correlation function obtaining:

$$\begin{aligned}\dot{\tilde{\rho}}(t) = &-\int_0^t dt' \int_{-\pi}^{\pi} d^D\vec{k}d^D\vec{k'} \frac{\lambda^2(2\pi)^{-D}}{2\sqrt{(\Omega\,\omega_{\vec{k}})(\Omega\,\omega_{\vec{k'}})}} \\ &\langle\tilde{A}(\vec{k},t)\tilde{A}^\dagger(\vec{k'},t')\rangle_{R_0}(\tilde{S}^\dagger(\vec{k},t)\tilde{S}(\vec{k'},t')\tilde{\rho}(t') - \tilde{S}(\vec{k'},t')\tilde{\rho}(t')\tilde{S}^\dagger(\vec{k},t)) \\ &+ \langle\tilde{A}^\dagger(\vec{k'},t')\tilde{A}(\vec{k},t)\rangle_{R_0}(\tilde{\rho}(t')\tilde{S}(\vec{k'},t')\tilde{S}^\dagger(\vec{k},t) - \tilde{S}^\dagger(\vec{k},t)\tilde{\rho}(t')\tilde{S}(\vec{k'},t')) \\ &+ \langle\tilde{A}^\dagger(\vec{k},t)\tilde{A}(\vec{k'},t')\rangle_{R_0}(\tilde{S}(\vec{k},t)\tilde{S}^\dagger(\vec{k'},t')\tilde{\rho}(t') - \tilde{S}^\dagger(\vec{k'},t')\tilde{\rho}(t')\tilde{S}(\vec{k},t)) \\ &+ \langle\tilde{A}(\vec{k'},t')\tilde{A}^\dagger(\vec{k},t)\rangle_{R_0}(\tilde{\rho}(t')\tilde{S}^\dagger(\vec{k'},t')\tilde{S}(\vec{k},t) - \tilde{S}(\vec{k},t)\tilde{\rho}(t')\tilde{S}^\dagger(\vec{k'},t'))\end{aligned} \tag{4.15}$$

To give an example we compute just the first average value

$$\begin{aligned}\langle\tilde{A}(\vec{k},t)\tilde{A}^\dagger(\vec{k'},t')\rangle_{R_0} &= \mathrm{Tr}_B[\tilde{A}(\vec{k},t)\tilde{A}^\dagger(\vec{k'},t')R_0] \\ &= \mathrm{Tr}_B[e^{iH_Bt}A(\vec{k})e^{-iH_Bt}e^{iH_Bt'}A^\dagger(\vec{k'})e^{-iH_Bt'}R_0] = \mathrm{Tr}_B[A(\vec{k})\tilde{A}^\dagger(\vec{k'},\tau)R_0] \\ &= \mathrm{Tr}_B[\int d\vec{k}d\vec{k'}A(k)A(k')e^{-i\omega_{k'}\tau}R_0] \\ &= \int_{-\pi}^{\pi} d\vec{k}e^{-i\omega_{\vec{k}}\tau}(N_{\vec{k}}+1)\end{aligned} \tag{4.16}$$

where $\tau = t - t'$

Finally, performing the Markov approximation $\tilde{\rho}(t') \simeq \tilde{\rho}(t)$, we can return in the

Schrodinger picture where we get

$$\begin{aligned}\dot{\rho(t)} = -i[H_S,\rho] - \int_0^t d\tau \int_{-\pi}^{\pi} d^D\vec{k}\frac{\lambda^2(2\pi)^{-D}}{2(\Omega\,\omega_{\vec{k}})} \\ \{e^{-i(\omega_{\vec{k}}-\Omega)\tau}N_{\vec{k}}+1)(a_1^\dagger a_1\rho - a_1\rho a_1^\dagger) + N_{\vec{k}}(\rho a_1 a_1^\dagger - a_1^\dagger\rho a_1) \\ + e^{i(\omega_{\vec{k}}-\Omega)\tau}(N_{\vec{k}}+1)(\rho a_1^\dagger a_1 - a_1\rho a_1^\dagger) + N_{\vec{k}}(a_1 a_1^\dagger\rho - a_1^\dagger\rho a_1)\} \\ \{e^{-i(\omega_{\vec{k}}-\Omega)\tau}N_{\vec{k}}+1)(a_2^\dagger a_2\rho - a_2\rho a_2^\dagger) + N_{\vec{k}}(\rho a_2 a_2^\dagger - a_2^\dagger\rho a_2) \\ + e^{i(\omega_{\vec{k}}-\Omega)\tau}(N_{\vec{k}}+1)(\rho a_2^\dagger a_2 - a_2\rho a_2^\dagger) + N_{\vec{k}}(a_2 a_2^\dagger\rho - a_2^\dagger\rho a_2)\} \\ + e^{-i\vec{k}\vec{r}} \\ \{e^{-i(\omega_{\vec{k}}-\Omega)\tau}(N_{\vec{k}}+1)(a_1^\dagger a_2\rho - a_2\rho a_1^\dagger) + N_{\vec{k}}(\rho a_2 a_1^\dagger - a_1^\dagger\rho a_2) \\ + e^{i(\omega_{\vec{k}}-\Omega)\tau}(N_{\vec{k}}+1)(\rho a_1^\dagger a_2 - a_2\rho a_1^\dagger) + N_{\vec{k}}(a_2 a_1^\dagger\rho - a_1^\dagger\rho a_2)\} \\ + e^{i\vec{k}\vec{r}} \\ \{e^{-i(\omega_{\vec{k}}-\Omega)\tau}N_{\vec{k}}+1)(a_2^\dagger a_1\rho - a_1\rho a_2^\dagger) + N_{\vec{k}}(\rho a_1 a_2^\dagger - a_2^\dagger\rho a_1) \\ + e^{i(\omega_{\vec{k}}-\Omega)\tau}(N_{\vec{k}}+1)(\rho a_2^\dagger a_1 - a_1\rho a_2^\dagger) + N_{\vec{k}}(a_1 a_2^\dagger\rho - a_2^\dagger\rho a_1)\}\end{aligned} \tag{4.17}$$

and gathering together the real and imaginary coefficients

$$\begin{aligned}\dot{\rho(t)} = -i[H_S,\rho] + \int_0^t d\tau \int_{-\pi}^{\pi} d^D\vec{k}\frac{\lambda^2(2\pi)^{-D}}{2(\Omega\,\omega_{\vec{k}})} \\ 2\{\cos((\omega_{\vec{k}}-\Omega)\tau)[(N_{\vec{k}}+1)\mathcal{L}[a_1](\rho) + N_{\vec{k}}\mathcal{L}[a_1^\dagger](\rho)] \\ + i\sin((\omega_{\vec{k}}-\Omega)\tau)[a_1\dagger a_1,\rho] \\ + \cos((\omega_{\vec{k}}-\Omega)\tau)[(N_{\vec{k}}+1)\mathcal{L}[a_2](\rho) + N_{\vec{k}}\mathcal{L}[a_2^\dagger](\rho)] \\ + i\sin((\omega_{\vec{k}}-\Omega)\tau)[a_2\dagger a_2,\rho]\} \\ \cos((\omega_{\vec{k}}-\Omega)\tau)e^{-i\vec{k}\vec{r}}(T_1+T_2) \\ + i\sin((\omega_{\vec{k}}-\Omega)\tau)e^{-i\vec{k}\vec{r}}(T_1-T_2) \\ + \cos((\omega_{\vec{k}}-\Omega)\tau)e^{i\vec{k}\vec{r}}(T_3+T_4) \\ + i\sin((\omega_{\vec{k}}-\Omega)\tau)e^{i\vec{k}\vec{r}}(T_4-T3)\end{aligned} \tag{4.18}$$

where $\mathcal{L}[O](\rho) = (O\rho O^\dagger - \frac{1}{2}\{O^\dagger O,\rho\})$

$$T_1 = (N_{\vec{k}}+1)(a_1^\dagger a_2\rho - a_2\rho a_1^\dagger) + N_{\vec{k}}(\rho a_2 a_1^\dagger - a_1^\dagger\rho a_2) \tag{4.19}$$

$$T_2 = (N_{\vec{k}}+1)(\rho a_1^\dagger a_2 - a_2\rho a_1^\dagger) + N_{\vec{k}}(a_2 a_1^\dagger\rho - a_1^\dagger\rho a_2) \tag{4.20}$$

$$T_3 = N_{\vec{k}}+1)(a_2^\dagger a_1\rho - a_1\rho a_2^\dagger) + N_{\vec{k}}(\rho a_1 a_2^\dagger - a_2^\dagger\rho a_1) \tag{4.21}$$

$$T_4 = (N_{\vec{k}}+1)(\rho a_2^\dagger a_1 - a_1\rho a_2^\dagger) + N_{\vec{k}}(a_1 a_2^\dagger\rho - a_2^\dagger\rho a_1). \tag{4.22}$$

The terms depending on $\sin((\omega_{\vec{k}}-\Omega)\tau)$ describe an extra unitary evolution of the probes induced by their coupling mediated by the bath because

$$T_1 - T_2 = (N_{\vec{k}}+1)[a_1^\dagger a_2;\rho] + N_{\vec{k}}[\rho; a_2 a_1^\dagger] = [a_1^\dagger a_2;\rho] \tag{4.23}$$

$$T_4 - T_3 = (N_{\vec{k}}+1)[\rho; a_2^\dagger a_1] + N_{\vec{k}}[a_1 a_2^\dagger;\rho] = [\rho; a_2^\dagger a_1]. \tag{4.24}$$

Avoiding to report the free evolution terms in order to account only the dissipation of the two probes the master equation becomes

$$\begin{aligned}\dot{\rho(t)} = \int_0^t d\tau \int_{-\pi}^{\pi} d^D\vec{k} \frac{\lambda^2(2\pi)^{-D}}{(\Omega\,\omega_{\vec{k}})} \{ &\cos((\omega_{\vec{k}}-\Omega)\tau)[(N_{\vec{k}}+1)\mathcal{L}[a_1](\rho)+N_{\vec{k}}\mathcal{L}[a_1^\dagger](\rho)] \\ &+\cos((\omega_{\vec{k}}-\Omega)\tau)[(N_{\vec{k}}+1)\mathcal{L}[a_2](\rho)+N_{\vec{k}}\mathcal{L}[a_2^\dagger](\rho)]\} \\ &-\cos((\omega_{\vec{k}}-\Omega)\tau)e^{-i\vec{k}\vec{r}}(T_1+T_2) \\ &-\cos((\omega_{\vec{k}}-\Omega)\tau)e^{i\vec{k}\vec{r}}(T_3+T_4)\end{aligned} \tag{4.25}$$

After that back into Schrödinger picture, the master equation reduces to

$$\dot{\rho}(t) = -i[H_S+H_{LS},\rho_S(t)] + \frac{\lambda^2}{2\Omega}\int_{-\pi}^{\pi} d^D\vec{k}\,\frac{1}{\omega_{\vec{k}}}\frac{\sin[t(\Omega-\omega_{\vec{k}})]}{\Omega-\omega_{\vec{k}}}\left\{(N_{\vec{k}}+1)\mathcal{L}_{S_{\vec{k}}}(\rho_S)+N_{\vec{k}}\mathcal{L}_{S_{\vec{k}}^\dagger}(\rho_S)\right\} \tag{4.26}$$

where we have introduced the Lamb shift hamiltonian that induce a system frequency renormalization

$$H_{LS} = \frac{\lambda^2}{2\Omega}\int_{-\pi}^{\pi} d^D\vec{k}\,\frac{1}{\omega_{\vec{k}}}\frac{1-\cos[t(\Omega-\omega_{\vec{k}})]}{\Omega-\omega_{\vec{k}}}S_{\vec{k}}^\dagger S_{\vec{k}}$$

Notice that we have introduced only one degree of freedom for each site, i.e. one dimensional harmonic oscillators in a D-dimensional real space, which corresponds also to a massive Klein Gordon field with spatial discrete structure. In addition setting the proper frequency of the oscilators $\omega_0 = 0$, in 3D lattice the model can be associated to studying cross-talk dynamics in a realistic crystal mediated by phonons of only one polarization, as for example gold Lynn et al. (1973), with a linear anisotropic dispersion that saturates for high momenta. Since dissipation into the crystal can be decomposed into three polarizations, we can choose to separate the problem into the three sets of polarizations, each having an anisotropic dispersion relation, as here considered.

In terms of $F_i = \{a_1, a_1^\dagger, a_2, a_2^\dagger\}$, the dissipative part reads:

$$\dot{\rho} = \sum_{j,l=1}^{4}\Gamma_{jl}(\vec{r},t)(F_j\rho_S F_l^\dagger - \frac{1}{2}\{F_l^\dagger F_j,\rho_S\})\,, \tag{4.27}$$

with

$$\begin{aligned}\Gamma_{11}(t) = \Gamma_{33}(t) &= \frac{\lambda^2}{2\Omega(2\pi)^D}\int_{-\pi}^{\pi} d^D\vec{k}\,\frac{N_{\vec{k}}+1}{\omega_{\vec{k}}}\,\frac{\sin[t(\Omega-\omega_{\vec{k}})]}{\Omega-\omega_{\vec{k}}} \\ \Gamma_{22}(\vec{r},t) = \Gamma_{44}(\vec{r},t) &= \frac{\lambda^2}{2\Omega(2\pi)^D}\int_{-\pi}^{\pi} d^D\vec{k}\,\frac{N_{\vec{k}}}{\omega_{\vec{k}}}\,\frac{\sin[t(\Omega-\omega_{\vec{k}})]}{\Omega-\omega_{\vec{k}}} \\ \Gamma_{13}(\vec{r},t) = \Gamma_{31}(\vec{r},t) &= \frac{\lambda^2}{2\Omega(2\pi)^D}\int_{-\pi}^{\pi} d^D\vec{k}\,\frac{N_{\vec{k}}+1}{\omega_{\vec{k}}}\,\frac{\sin[t(\Omega-\omega_{\vec{k}})]}{\Omega-\omega_{\vec{k}}}\cos(\vec{k}\cdot\vec{r}) \\ \Gamma_{24}(\vec{r},t) = \Gamma_{42}(\vec{r},t) &= \frac{\lambda^2}{2\Omega(2\pi)^D}\int_{-\pi}^{\pi} d^D\vec{k}\,\frac{N_{\vec{k}}}{\omega_{\vec{k}}}\,\frac{\sin[t(\Omega-\omega_{\vec{k}})]}{\Omega-\omega_{\vec{k}}}\cos(\vec{k}\cdot\vec{r}).\end{aligned} \tag{4.28}$$

The Lamb Hamiltonian reads $H_{LS} = \Delta\Omega(a_1^\dagger a_1 + a_2^\dagger a_2) + \gamma(a_1 a_2^\dagger + a_1^\dagger a_2)$ with

$$\Delta\Omega = \frac{-\lambda^2}{4\Omega(2\pi)^D}\int_{-\pi}^{\pi} d^D\vec{k}\,\frac{1-\cos[t(\Omega-\omega_{\vec{k}})]}{\omega_{\vec{k}}(\Omega-\omega_{\vec{k}})} \tag{4.29}$$

$$\gamma = \frac{-\lambda^2}{4\Omega(2\pi)^D}\int_{-\pi}^{\pi} d^D\vec{k}\,\frac{1-\cos[t(\Omega-\omega_{\vec{k}})]}{\omega_{\vec{k}}(\Omega-\omega_{\vec{k}})}\cos(\vec{k}\cdot\vec{r}). \tag{4.30}$$

In the disordered crystal case, the damping coefficients are

$$\begin{aligned}
\Gamma_{11}(t) = \Gamma_{33}(t) &= \frac{\lambda^2}{2\Omega}\int_{-\pi}^{\pi} d^D\vec{k}\,\frac{N_{\vec{k}}+1}{\omega_{\vec{k}}}\,\frac{\sin[t(\Omega-\omega_{\vec{k}})]}{\Omega-\omega_{\vec{k}}}|f_{\vec{n},\vec{k}}|^2\\
\Gamma_{22}(\vec{r},t) = \Gamma_{44}(\vec{r},t) &= \frac{\lambda^2}{2\Omega}\int_{-\pi}^{\pi} d^D\vec{k}\,\frac{N_{\vec{k}}}{\omega_{\vec{k}}}\,\frac{\sin[t(\Omega-\omega_{\vec{k}})]}{\Omega-\omega_{\vec{k}}}|f_{\vec{n},\vec{k}}|^2\\
\Gamma_{13}(\vec{r},t) = \Gamma_{31}(\vec{r},t) &= \frac{\lambda^2}{2\Omega}\int_{-\pi}^{\pi} d^D\vec{k}\,\frac{N_{\vec{k}}+1}{\omega_{\vec{k}}}\,\frac{\sin[t(\Omega-\omega_{\vec{k}})]}{\Omega-\omega_{\vec{k}}}f_{\vec{n},\vec{k}}f^*_{\vec{n}',\vec{k}}\\
\Gamma_{24}(\vec{r},t) = \Gamma_{42}(\vec{r},t) &= \frac{\lambda^2}{2\Omega}\int_{-\pi}^{\pi} d^D\vec{k}\,\frac{N_{\vec{k}}}{\omega_{\vec{k}}}\,\frac{\sin[t(\Omega-\omega_{\vec{k}})]}{\Omega-\omega_{\vec{k}}}f_{\vec{n},\vec{k}}f^*_{\vec{n}',\vec{k}},
\end{aligned} \tag{4.31}$$

always understanding that $\vec{r} = \vec{n} - \vec{n}'$. Correspondingly :

$$\Delta\Omega = \frac{-\lambda^2}{4\Omega}\int_{-\pi}^{\pi} d^D\vec{k}\,\frac{1-\cos[t(\Omega-\omega_{\vec{k}})]}{\omega_{\vec{k}}(\Omega-\omega_{\vec{k}})}|f_{\vec{n},\vec{k}}|^2 \tag{4.32}$$

$$\gamma = \frac{-\lambda^2}{4\Omega}\int_{-\pi}^{\pi} d^D\vec{k}\,\frac{1-\cos[t(\Omega-\omega_{\vec{k}})]}{\omega_{\vec{k}}(\Omega-\omega_{\vec{k}})}f_{\vec{n},\vec{k}}f^*_{\vec{n}',\vec{k}}. \tag{4.33}$$

The self-damping coefficients of each oscillator are given for $j = l$ whilst cross terms, such as $|j-l| = 2$ characterize the dissipation with

$$\Gamma_{jl}^{(D)}(\vec{r},t) = \int_{-\pi}^{\pi} d^D\vec{k}C_{jl}(\vec{k},\vec{r},t) \tag{4.34}$$

whose non-vanishing terms are

$$C_{11} = [n(\vec{k})+1]\sin[(\omega(\vec{k})-\Omega)t]/[\omega(\vec{k})-\Omega] = C_{33}, \tag{4.35}$$

$$C_{22} = n(\vec{k})\,\sin[(\omega(\vec{k})-\Omega)t]/[\omega(\vec{k})-\Omega] = C_{44}, \tag{4.36}$$

$$C_{13} = C_{11}\cos(\vec{k}\cdot\vec{r}), \tag{4.37}$$

$$C_{24} = C_{22}\cos(\vec{k}\cdot\vec{r}). \tag{4.38}$$

For a lattice with null temperature, the only nonvanishing coefficients are the the self-damping $\Gamma_{11} = \Gamma_{33}$ and cross dissipation $\Gamma_{13} = \Gamma_{24}$. It should be noticed now a crucial point: if the two probes are attached to a common environment point, i.e. $H_{SB} = \lambda(a_1 + a_2)A_{\vec{n}}^\dagger + h.c.$, we have

$$\Gamma_{11} = \Gamma_{13} \quad \text{and} \quad \Gamma_{22} = \Gamma_{24} \tag{4.39}$$

Jeske & Cole (2013), whereas for probes attached to two independent environments (SB case) we would have

$$\Gamma_{13} = \Gamma_{24} = 0, \tag{4.40}$$

implying that no cross terms appear. Separate baths can also be found probing the opposite edges of a string (a scalar version of the Casimir force setting) Ford & O'Connell (2014). The cross-over between common bath and separate bathes regimes with the probes distance can now be derived from our microscopic model without any further assumptions. When the interaction time becomes long enough, i.e. $\tau \to \infty$ only a family of resonant momentum crystal phonons is relevant, such that $\omega(\vec{k}_\Omega) = \Omega$. This condition identifies the manifold of phonons mediating an eventual cross-talk between the oscillators. The dependence on probes distance and position at $T = 0$ and long times is then

$$\Gamma_{13}^{(D)}(\vec{r}) = \int d^D\vec{k}\cos(\vec{k}\vec{r})\delta(\omega(\vec{k}) - \Omega) \tag{4.41}$$

4.2 The exceptional 1D case and disorder effects

It is worth noting an immediate consequence, previously yet observed in Doll et al. (2006); Jeske & Cole (2013); McCutcheon et al. (2009), but whose valence was scarcely emphasized. In 1D chain, with any arbitrary dispersion relation, we obtain after the time integration

$$\Gamma_{jl}^{(D)}(x) \propto \cos(k_\Omega x), \tag{4.42}$$

since the dirac delta constraining the frequency of the bath to be resonant to the probes' ones exhausts all freedom in choosing the crystal momenta. In other world this implies that two probes will experience a collective dissipation even if they are far away from each other. In fact not only when they are attached to the same point but also when at the anti-nodes of the resonant mode. This configuration is also responsible of some entanglement creation mechanism among distant probes **?**. Depending on the probes position, one of the two relevant degree of freedom; the center of mass or relative position the of the two of probes, can be decoupled from the environment and relies to a decoherence free subspace. The surprising result is that a cross-over between a SB and CB is periodically predicted in contrast to the naive intuitive expectation of an asymptotic cross-damping decay for longer distances. For a finite chain environment this leads to SB dissipation for probes at the edges Ford & O'Connell (2014). Further, if the relative size of cross-damping and self-damping are considered, this result is unchanged when increasing the temperature of the thermal bath because the mean number of phonons in the bath $N_{\vec{k}}$ factors out of the integrals depending only on the frequency.

The emergence of collective dissipation even at long distances is reminiscent of the lattice symmetry but the fragility of this phenomenon could be assessed considering the effect of adding disorder to the chain, as in a more realistic and experimentally testable scenario. The cross-talk can be thought, with the same spirit of a Fourier analysis, as the sum of overlaps of resonant crystal normal modes present at the probes positions. The expression in eq.(4.42) is just a sum of the normal modes in the crystal that are plane waves of the form $\exp(i\vec{k}\vec{r})$. In general, when some defects are added, it can be expressed as $\int d\vec{k} f_{\vec{n},\vec{k}} f^*_{\vec{n}',-\vec{k}} t\ \mathrm{sinc}[t(\omega(\vec{k} - \Omega)]$ where instead of plane waves, f is the transformation matrix between the real space of crystal oscillators and its dual space. Whenever there is disorder in the crystal, it will break the translational invariance, and thus its normal modes will not be plane waves, but rather periodic, localized waves. This can be seen in Fig.4.1 where the cross-talk $cos(k_\Omega x)$ becomes distance-decaying for large enough noise in the crystal. This localization effect Anderson (1958), will reduce the spatial overlap with deep consequences on the periodic cross-over between CB and SB shown in Fig.4.7.

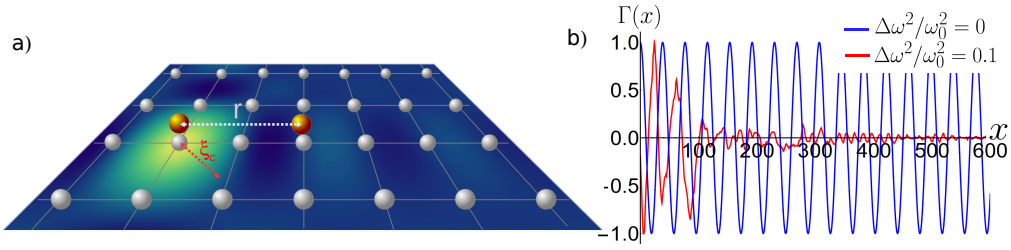

Figure 4.1: Cross-talk for the 1D crystal with the same parameters as Fig.4.2, but with added random noise in the onsite potential $\Delta\omega^2$. We have chosen a probe frequency Ω resonant with $k_\Omega = 0.0157$. The cross-talk without noise is $\Gamma(x) = cos(k_\Omega x)$ while it becomes increasingly localized when adding noise to local crystal frequencies. The figure has been produced with a finite crystal with 600 atoms, and the cross-talk has been averaged as $\Gamma(x) \hat{=} \sum_{x_0} \Gamma_{x0}(x)$, that is, evaluating the cross-talk with origin at x_0 (remember that with noise the crystal eigenfunctions do not follow anymore translational invariance and are thus position dependent).

The presence of some degree of disorder in the lattice, here modeled by inhomogeneity in the local crystal potentials, breaks breaks the symmetry of the crystal and hence the periodicity of the cross damping terms, leading to a decaying function. Beyond a critical distance, the pair of probes will dissipate into different environments.

4.3 Higher dimensions

The generalization to higher dimensional environment leads to a richer scenario. Anyway when moving to $D > 1$ the isotropy of the dispersion relation of the environment was widely assumed in several phenomenological approaches, either they refers to spin-boson models Venuti & Zanardi (2007); McCutcheon et al. (2009); Doll et al. (2006); Jeske & Cole (2013); Dorner (2012); Rivas Vargas & Müller (2015); Jeske et al. (2014) or boson-boson Zell et al. (2009). In the isotropy configuration the dispersion relation of the environment depends only on the wave vector modulus $\omega_{\vec{k}} \propto |\vec{k}|$, a typical situation in electromagnetic environment Dicke (1954); Breuer & Petruccione (2002). This enables some analytical insight and leads to a spatial decaying cross-talk in the master equation. For $T = 0$ and long times the cross-talk dependence on the environment dimension is

$$\Gamma_{13}^{(1)}(r) \propto \cos(|k_\Omega| x), \tag{4.43}$$

$$\Gamma_{13}^{(2)}(\vec{r}) \propto J_0(|\vec{k}_\Omega| r), \tag{4.44}$$

$$\Gamma_{13}^{(3)}(\vec{r}) \propto \mathrm{sinc}(|\vec{k}_\Omega| r). \tag{4.45}$$

In a crystal model this happens when Ω is engineered to be slightly above ω_0, so the probes resonate only with low-momentum phonons. This can be seen in Fig.4.2b (2D crystal): the contour of crystal momenta which are resonant with Ω is parametrized only by the modulus $|\vec{k}|$ (fig. 4.2 black circle) and the polar integration yields a Bessel J_0 of the radial distance between probes a transition to a separate environment arises insensitive of the crystal direction probed by the system components.

Departure from isotropic dispersion relations has deep consequences. Although in general there will be a spatial non-monotonic decay of $\Gamma_{13}^{(d)}(\vec{r})$, different scenarios can arise like those of Fig. 4.2c and 4.2d. In general the anisotropy of the dispersion will translate in a sensitivity of the probes dissipation to the crystal geometry. In Fig. 4.2c

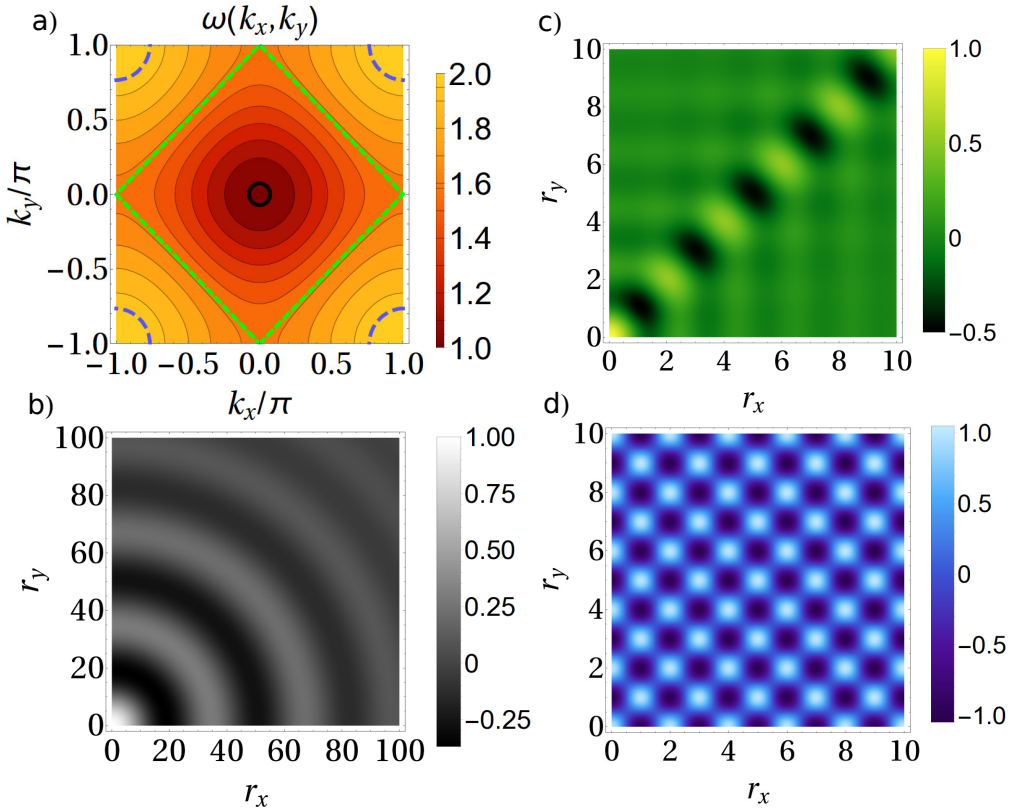

Figure 4.2: a) 2D dispersion relation in color code with $\omega_0 = 1$ and $g = 3/16$, so that $\omega(\vec{k}) \in [1, 2]$. Iso-frequency surfaces are shown for the limiting cases discussed in the text: black) $\Omega = 1.01$ corresponding to the isotropic case, green) $\Omega = \sqrt{5/2}$ and blue) $\Omega = 1.95$. Normalized cross-damping term $\Gamma(r_x, r_y) \hat{=} \Gamma^{(2)}_{13}(\vec{r})/\Gamma^{(2)}_{13}(0)$ for b) the isotropic case (low momenta), for c) directional non-decay (medium momenta) and d) non-decay (high momenta) (see text for details). We plot only one spatial quadrant because of the symmetry of the setting.

we observe for a particular resonance value Ω an interference effect resulting in decay of $\Gamma^{(d)}_{13}(\vec{r})$ along all directions *except* for the lattice diagonals $y = \pm x$ where it does not decay. For $\cos(\vec{k}\vec{r})$ as exponentials and using $\vec{k}_\Omega = \{k_x, \pm(\pi - |k_x|)\}$ actually it can be seen that along these spatial directions the product $\vec{k}\vec{r}$ cancels except for a $\exp i\pi r_y$ term, yielding an integral which does not depend on momenta and therefore does not yield a decay: $\Gamma^{(2)}_{13}(\vec{r}) \propto (x\sin(\pi x) - y\sin(\pi y))/(x^2 - y^2)$ not yielding decay on the crystal diagonals. Strong anisotropy is also displayed in Fig. 4.2d, for Ω resonant to highest crystal momenta: here, integration over $\vec{k}_\Omega$ is a sum over a tiny amount of momenta (ideally for the highest allowed momenta we should integrate only $k_x = \pm\pi$, $k_y = \pm\pi$ and leading to a periodic cross-term $\Gamma^{(2)}_{13}(\vec{r}) \propto \cos(\pi r_x)\cos(\pi r_y)$. Then no asymptotic decay of the cross-damping with distance occurs and these high frequency probes are able to 'resolve' the spatial structure of the crystal.

When considering 3 spatial dimensions, the reasoning is similar: resonant momenta for a given Ω will lie on a surface, and the interference made by their sum will produce

the spatial shape of the cross-talk. For isotropic (low momenta) case we have the form $\Gamma_{13}^{(3)}(|\vec{r}|) \propto \mathrm{sinc}(|\vec{k}_\Omega||\vec{r}|)$, while for high momentum we have a highly oscillating behavior in 3D $\Gamma_{13}^{(3)}(\vec{r}) \propto \cos(\pi r_x)\cos(\pi r_y)\cos(\pi r_z)$.

4.3.1 2D triangular lattice

If we consider a triangular lattice, instead of cubic, diagonalization of H_B would be done through plane waves along momentum directions corresponding to the correct Bravais lattice. Since the direct lattice has proper vectors

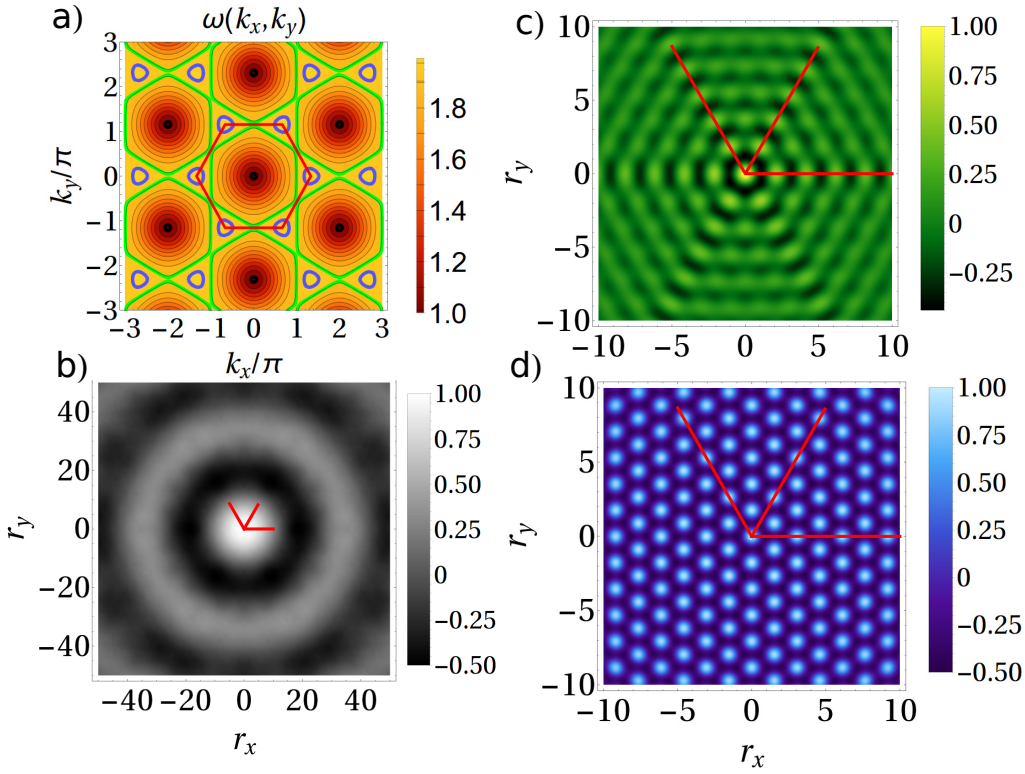

Figure 4.3: a) 2D dispersion relation in colour code with $\omega_0 = 1$ and $g = 0.165$, so that $\omega_{\vec{k}} \in [1, 1.992]$. Isofrequency surfaces are shown for the limiting cases equivalent to those of the cubic crystal of the main text: black) $\Omega = 1.01$ corresponding to the isotropic case, green) $\Omega = 1.905$ directional non-decay, and blue) $\Omega = 1.99$ non-decay. We have also plotted in red the fundamental (Wigner-Seitz) cell, to which momentum integrals are restricted. Normalized cross-damping term $\Gamma(r_x, r_y) \hat{=} \Gamma_{13}^{(2)}(\vec{r})/\Gamma_{13}^{(2)}(0)$ for b) the isotropic case (low momenta), for c) directional non-decay (medium momenta) and d) non-decay (high momenta), where we have added in red the crystal symmetry directions to show that the cross-damping term conserves the symmetry of the problem.

$$\vec{v}_1 = \hat{u}_x \tag{4.46}$$

$$\vec{v}_2 = \hat{u}_x/2 + \sqrt{3}/2\hat{u}_y, \tag{4.47}$$

its Bravais lattice has corresponding vectors

$$\vec{b}_1 = 2\pi(\hat{u}_x - \hat{u}_y/\sqrt{3}) \tag{4.48}$$

$$\vec{b}_1 = 4\pi\hat{u}_y/\sqrt{3}. \tag{4.49}$$

The momentum expansion should be done in this directions and the dispersion relation results

$$\omega(\vec{k}) = \sqrt{\omega_0^2 + 8g(\sin^2(l_1/2) + \sin^2(l_2/2) + \sin^2(l_3/2))} \tag{4.50}$$

having imposed $l_1 = k_x$, $l_2 = k_x/2 + \sqrt{3}k_y/2$ and $l_3 = k_x/2 - \sqrt{3}k_y/2$. An analysis of this setting shows a similar behaviour of the cross-damping term: isotropic decay with distance for Ω resonant with low momentum phonons, interference effects along symmetry directions at resonance with larger momenta and non-decaying cross-damping for very high momenta as it is shown in fig.4.3. In order to compare the cross-damping terms with the bath correlation function we report it in fig.**??**.

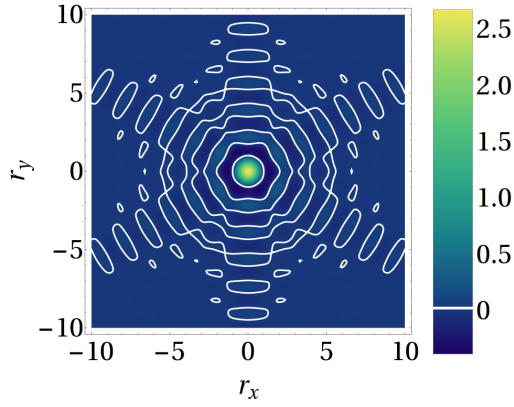

Figure 4.4: Correlation function $C(r_x, r_y)$ for the 2D triangular crystal in colour code. We have highlighted the particular value $C(r_x, r_y) = 0.01$ in white to guide the eye.

4.3.2 Finite time regime

Previous results are presented considering dissipation in the long time limit while at short times there is transient behavior in which signal travels from one probe to the other at the fastest group velocity allowed in the crystal. This is seen in the cross-talk, which expands its spatial structure at that velocity, reaching its final (momentum dependent) form (displayed for $t \to \infty$ in Figs. 4.1 and 4.2).

In fig.4.5 we report the results of the integration of the damping coefficients when the of system-bath interaction time is finite. However the finite time regime could be explored expanding the integrand terms $C_{jl}(\vec{k}, \vec{r}, t)$ yielding to $\Gamma^{(D)}(\vec{r})$ in series of a parameter $\epsilon^{(D)} = \frac{2Dg}{\omega_0^2}$ that describes the strength among the oscillators of the environment, viz. their mutual interaction is much smaller than the square of the proper frequency. In this case we consider the bath Hamiltonian in the rotating wave approximation

$$H_B = \sum_{\vec{n}} \Delta^{(D)} A^\dagger_{\vec{n}} A_{\vec{n}} - \frac{g}{\Delta^{(D)}}(A^\dagger_{\vec{n}+\vec{l}} A_{\vec{n}} + h.c.)$$

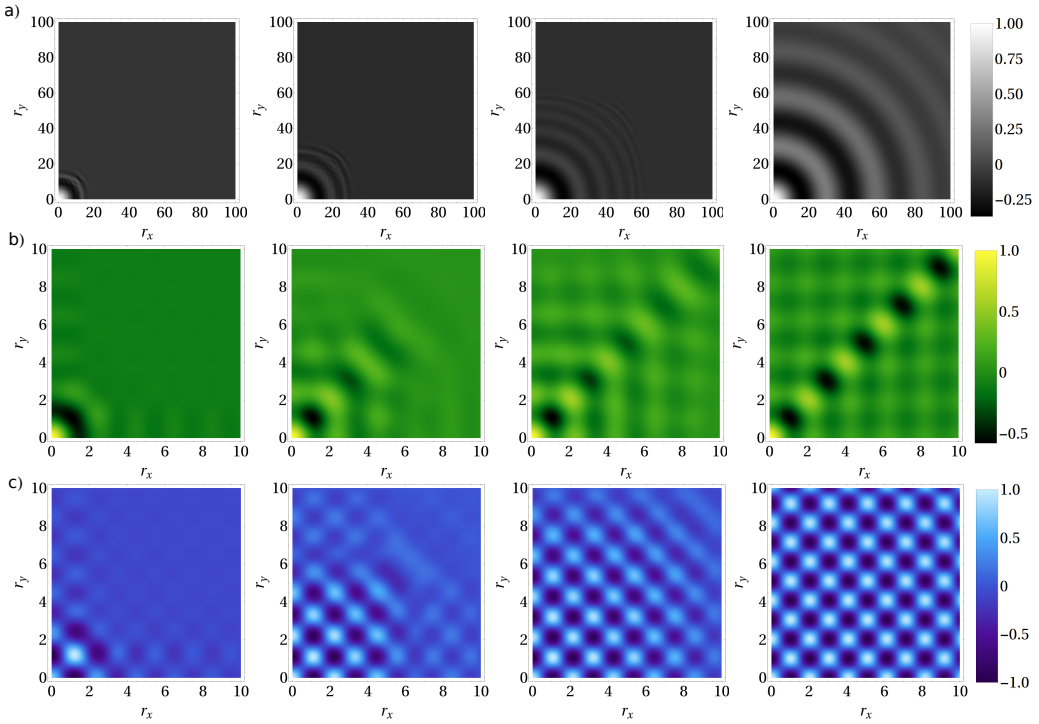

Figure 4.5: Short-time behaviour of the 2D crystal cross-talk, for the limiting cases of figure 2 in main text: a) isotropic, b) directional non-decay, c) non-decay. From left to right, we show times a) $\omega_0 t = 50, 100, 200, 1000$ and b,c) $\omega_0 t = 10, 30, 70, 10000$. For b) and c) it was necessary to plot longer times in order to see better the resulting cross-talk obtained in main text's figure 2 for the long time limit.

where $\Delta^{(D)} = \sqrt{\omega_0^2 + 2Dg}$ Afterward we are able to integrate it in time and over momenta, conducting to expression easy to manipulate. We report here just some relevant cases in 1D and 2D. When dealing with an harmonic chain we can easily find

$$\Gamma_c^{(1)}(r,t) \propto \frac{\sin(\pi r)}{r} \frac{f_1^{(1)}(r^\alpha)}{f_2^{(1)}(r^\alpha)} \tag{4.51}$$

where $f_{1,2}^{(1)}(r^\alpha)$ are polynomials of maximum order α namely the expansion order. Their expression reads

$$\begin{aligned} f_1^{(1)}(r,t) &= \frac{1}{2(r^2-1)(\Omega-\omega_0)^2}\{\cos[t(\Omega-\omega_0)](t\epsilon(2-3r^2)\omega_0(\Omega-\omega_0)+ \\ &\sin[t(\Omega-\omega_0)](2(r^2-1)(\omega_0(\epsilon-2)+2\Omega)+r^2\epsilon\omega_0)\}; \\ f_2^{(1)}(r^2,t) &= \frac{1}{16(4-5r^2+r^4)(\Omega-\omega_0)^3}\{\cos[t(\Omega-\omega_0)]g_1+\sin[t(\Omega-\omega_0)]g_2\} \end{aligned} \tag{4.52}$$

that depends on other two polynomials:

$$g_1(r,t) = (2t\epsilon(\Omega-\omega_0)\omega_0(2(r^2-4)(4+2r^2(\epsilon-3)-\epsilon)\Omega+(32+r^4(12-13\epsilon)-26\epsilon+r^2(57\epsilon-56))\omega_0) \tag{4.53}$$

and

$$\begin{aligned} g_2(r,t) =&\Omega^2(128-18t^2\epsilon^2\omega_0^2+r^4(32-9t^2\epsilon^2\omega_0^2)+r^2(39t^2\epsilon^2\omega_0^2-160))+\\ &2\Omega\omega_0[r^2(160-56\epsilon+\epsilon^2(18-39t^2\omega_0^2))+r^4(12\epsilon+\epsilon^2(9t^2\omega_0^2-4)-32)+\\ &2(16\epsilon+\epsilon^2(9t^2\omega_0^2-4)-64)]+\\ &\omega_0^2[128-64\epsilon+\epsilon^2(52-18t^2\omega_0^2)+r^4(32-24\epsilon+\epsilon^2(26-9t^2\omega_0^2))+\\ &r^2(112\epsilon+3\epsilon^2(13t^2\omega_0^2-38)-160)]. \end{aligned} \tag{4.54}$$

The $f_3^{(1)}(r^3)$ expression, i. e. the polynomial appearing at the third order expansion, is quite cumbersome and we are not reporting it but results are shown in fig. 4.6. A comparison with the results discussed along the text shows that increasing the interaction time the probes interact with bath normal modes in a range of frequency narrower and narrower, untill they become resonant with just only one mode. When performing the $\epsilon-$expansion we are assuming that the interaction among the oscillators of the bath could be treated just as a perturbation to the Hamiltion of an infinite collection of free harmonic oscillator. This perturbation modify slightly the isotropic dispersion of a collection of free boson and it is in agreement with the analytical behaviour of the probes resonant with the low momenta of the bath.

For different order of expansion $\Gamma_c^{(1)}(r,t) \propto \frac{\sin(\pi r)}{r}\frac{f_1^{(1)}(r^\alpha)}{f_2^{(1)}(r^\alpha)}$ where $f_{1,2}^{(1)}(r^\alpha)$ are polynomials of maximum order α namely the expansion order. In addition $\Gamma_c^{(1)}(r,t)$ at fixed distance is always bounded by a two polynomial function

The cross-damping term of the 2D square lattice at the first order expansion in $\epsilon^{(2)}$ is

$$\begin{aligned} \Gamma^{(2)}(r_x,r_y,t) \propto & \frac{\sin(\pi r_x)\sin(\pi r_y)}{r_x(r_x^2-1)r_y(r_y^2-1)(\Omega-\omega_0)^2}\\ &\left[f_1^{(2)}(r_x,r_y,t)\cos((\Omega-\omega_0)t)+f_2^{(2)}(r_x,r_y)\sin((\Omega-\omega_0)t)\right] \end{aligned} \tag{4.55}$$

having introduced the two functions

$$f_1^{(2)}(r_x,r_y,t) = t(\Omega-\omega_0)\epsilon(3r_y^2-2+r_x^2(3-4r_y)) \tag{4.56}$$

$$f_2^{(2)}(r_x,r_y) = r_x^2(r_y^2-1)\epsilon\omega_0+(rx^2-1)(4\Omega(r_y^2-1)+\omega_0(r_y^2(3\epsilon-4)-2\epsilon+4)) \tag{4.57}$$

$h_\pm(t) = \pm(k_1+k_2t^\alpha)$ with $k_{1,2}$ two constant depending on the distance and frequencies chosen.

4.3.3 Non point-like interaction

Our conclusions are rather general even if the probes have a finite spatial extension and are hence interacting with a finite-sized region of the crystal, $H_{SB} = \lambda\sum_{\vec{R}} g(\vec{R})(a_1A^\dagger_{(\vec{n}+\vec{R})}+ a_2A^\dagger_{(\vec{n}'+\vec{R})}+h.c.)$ with $g(\cdot)$ a function decaying for $\vec{R}$ up to each probe size. Whereas for point-like contact with the bath we had $H_{SB} = \int d^d\vec{k}(S^\dagger(\vec{k})A(\vec{k})+h.c)$ and $S^\dagger(\vec{k}) = e^{i\vec{k}\vec{r}_1}S_0^\dagger(\vec{k})$ with $S_0^\dagger(\vec{k}) = (a_1+e^{i\vec{k}(\vec{r}_2-\vec{r}_1)}a_2)$, for extended probes the systems operators acquire a spatial interaction of the form

$$S^\dagger(\vec{k}) = \sum_{\vec{R}} g(\vec{R})e^{i\vec{k}(\vec{r}_1-\vec{R})}S_0^\dagger(\vec{k}). \tag{4.58}$$

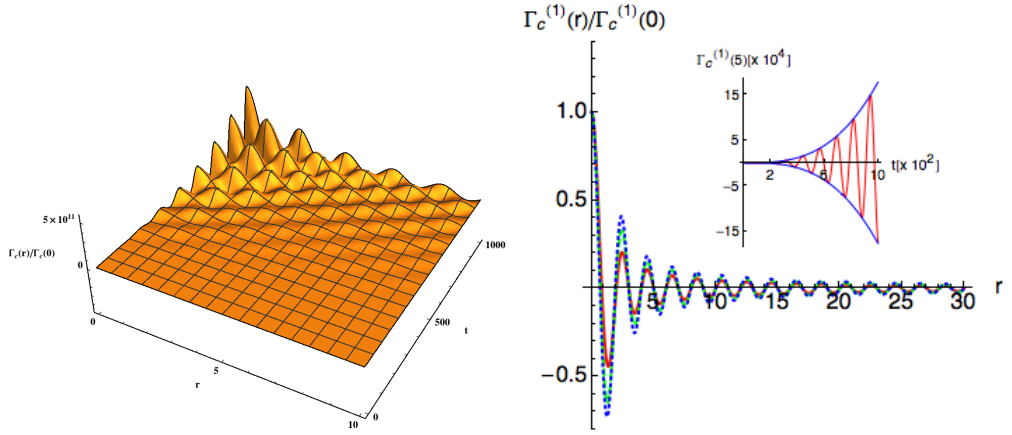

Figure 4.6: The left panel shows the behavior of the cross damping rate $\Gamma_c^{(1)}$ up the third order in $\epsilon^{(1)}$ in function of the distance between the probes r and the interaction time t. In the right panel we plot the ratio of $\Gamma_c^{(1)}$ at distance r and when they are attached to same site for $t = 1000$. Red solid, dashed green, dotted blue lines correspond respectively to first, second, third order in ϵ-expansion. In the inset we show $\Gamma_c^{(1)}(t)$, neglecting $o(\epsilon^{(1)^4})$ terms, at fixed distance $r = 5$ that bounded by the functions $\pm(-0.778793 + 0.000018t^{3.000146})$. In all plots $\Omega = 1.05, \omega_0 = 1.0, \epsilon^{(1)} = 0.1$

It is easy to check that combinations like $S^\dagger(\vec{k})S(\vec{k})$ are the ones entering the master equation, and therefore we have finally that self-damping terms such as $\Gamma_1 1$ are proportional to

$$\Gamma_{11} \propto \sum_{\vec{R},\vec{R}'} g(\vec{R})g(\vec{R}')e^{i\vec{k}(\vec{R}-\vec{R}')} \tag{4.59}$$

while cross-terms like $\Gamma_1 3$ are proportional to

$$\Gamma_{13} \propto e^{i\vec{k}(\vec{r}_1-\vec{r_2})} \sum_{\vec{R},\vec{R}'} g(\vec{R})g(\vec{R}')e^{i\vec{k}(\vec{R}-\vec{R}')} \tag{4.60}$$

with relative factor $e^{i\vec{k}(\vec{r}_1-\vec{r_2})}$ as before. Since the comparison common vs. separate baths is a matter of balance between cross and self damping, the case of spatially-extended probes is also governed by a relative factor $e^{i\vec{k}(\vec{r}_1-\vec{r_2})}$ and therefore the arguments and figures presented apply equally well. Of course the case of point-like system-bath interaction is recovered for $g(\vec{R}) = \delta_{\vec{R},\vec{0}}$.

4.4 Correlation length in the crystal.

An interesting question arise when considering the relationship between the picture of common versus separate environment, viz. decay vs. non-decay cross-damping, we have just seen and the correlation length of the environment. The cross- and self-damping terms in the dissipation equation (4.26) come from bath operator spatial correlation functions $\left\langle A_{\vec{n}}(0)A^\dagger_{\vec{n}'}(t)\right\rangle$ at two times. This time dependence is the one that, for long times, selects a unique wave vector due to resonance with Ω, coming from the integration of $\mathrm{sinc}[(\omega(\vec{k}) - \Omega)t]$. Therefore follows from a reduced manifold of momenta that

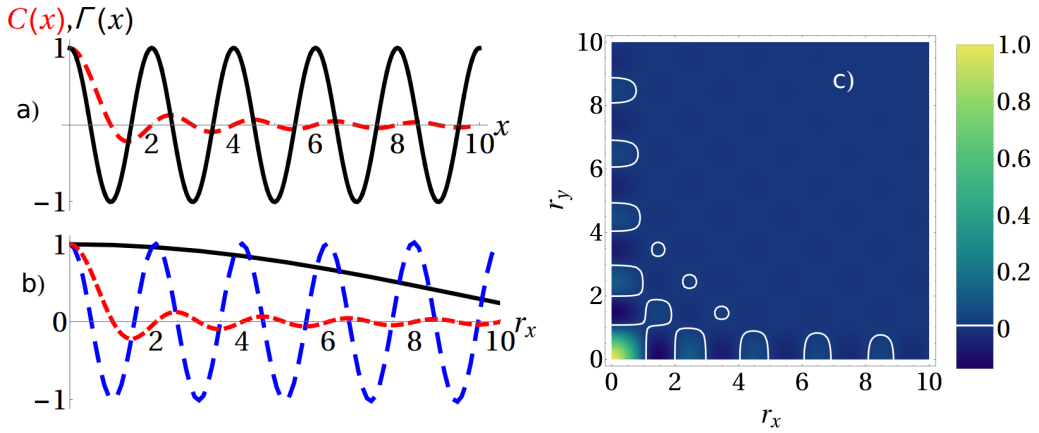

Figure 4.7: a) Crystal correlation function $C(x)$ in 1D in red, vs. the cross-damping term in black of probes with frequency $\Omega = 2\omega_0$. We have chosen $\omega_0 = 1$ and $g = 3/4\omega_0^2$, so that again $\omega(\vec{k}) \in [1, 2]$. Lower Ω would simply resonate with a lower momentum and we would see a cosine with longer periodicity. b) Correlation function for the 2D-crystal in red, compared with the cross-damping along r_x (with $r_y = 0$) for the isotropic case (black) and high momentum case (blue), as previously shown in fig1b and 1d, respectively, with the same parameters as figure 1. c) The crystal correlation function is plotted at the right for the two coordinates (r_x, r_y) in color code, and we have highlighted the particular value $C(r_x, r_y) = 0.01$ in white to guide the eye.

is that of dimension $D-1$. On the other hand, the correlation in the crystal at two different points comes from the two points cumulant at equal time $\langle A_{\vec{n}}(t) A_{\vec{n}'}(t)\rangle$ and depends on all phonons momenta. In other words cross-damping is caused by resonant phonons, while generic correlations in the crystal are caused by interference of all phonons. Since part of 'all frequencies' is the isotropic part of the phonon spectrum, it is to be expected that correlations are decaying with distance, even in 1D. Indeed, the spatial correlations of observables like the crystal displacement field $\phi(\vec{r}) = A_{\vec{r}} + A^\dagger_{\vec{r}}$ between crystal locations $\vec{r}$ and $\vec{r} + \vec{R}$ and for a thermal state leads to

$$\left\langle \phi(\vec{r})\phi(\vec{r}+\vec{R})\right\rangle \propto \int_0^\pi d^D\vec{k}\left[2n(\vec{k})+1\right]\cos(\vec{k}\cdot\vec{R}) \tag{4.61}$$

or, for $T = 0$, simply $\int_0^\pi d^D\vec{k}\cos(\vec{k}\cdot\vec{R})$. The main difference with the cross-damping eq. (4.41) is the filter at resonant frequencies. Therefore spatially decaying correlations are not the cause of the CB/SB cross-over as illustrated in Fig. 4.2, where the normalized correlation function $C(r_x, r_y) = \left\langle \phi(\vec{0})\phi(\vec{r})\right\rangle$ is compared with the cross-damping in different cases. Indeed spatial correlations decay at distances of the order of the crystal lattice $\xi_c \approx a$ (notice that all spatial coordinates are scaled with a in the rest of the manuscript) while the cross-over between CB and SB arises on a scale given by the resonant normal mode wave-length $\approx |k_\Omega|^{-1}$.

The environment's correlation function at finite temperature is

$$\left\langle \phi(\vec{r})\phi(\vec{r}+\vec{R})\right\rangle \propto \int_0^\pi d^D\vec{k}\left[2n(\vec{k})+1\right]\cos(\vec{k}\cdot\vec{R}) = \int_0^\pi d^D\vec{k}\coth\left[\frac{\hbar\omega_{\vec{k}}}{2k_BT}\right]\cos(\vec{k}\cdot\vec{R})$$

, and therefore the temperature dependence contributes to its spatial shape. This is in

contrast with the long-times behaviour of the cross-talk at finite temperature

$$\begin{aligned}\Gamma_{13}^{(D)}(\vec{r}) &\propto \int_{-\pi}^{\pi} d^D\vec{k}\delta(\omega_{\vec{k}}-\Omega)\left[n(\vec{k})+1\right]\cos(\vec{k}\cdot\vec{R}) \\ &= \int_{-\pi}^{\pi} d^D\vec{k}\delta(\omega_{\vec{k}}-\Omega)\frac{1}{2}\left[\coth\left(\frac{\hbar\omega_{\vec{k}}}{2k_BT}\right)+1\right]\cos(\vec{k}\cdot\vec{R})\end{aligned} \tag{4.62}$$

where the cotangent factors out of the integral. Thus we have a common prefactor $(1/2)\left[\coth(\hbar\Omega/2k_BT)+1\right]$ and an integral in momenta which does not depend on temperature, meaning that the spatial shape is independent of temperature. It must be stressed though, as seen in Fig. 4.8, that the correlation function is not too different for different temperature scales, mostly its basic spacing which coincides with the crystal constant.

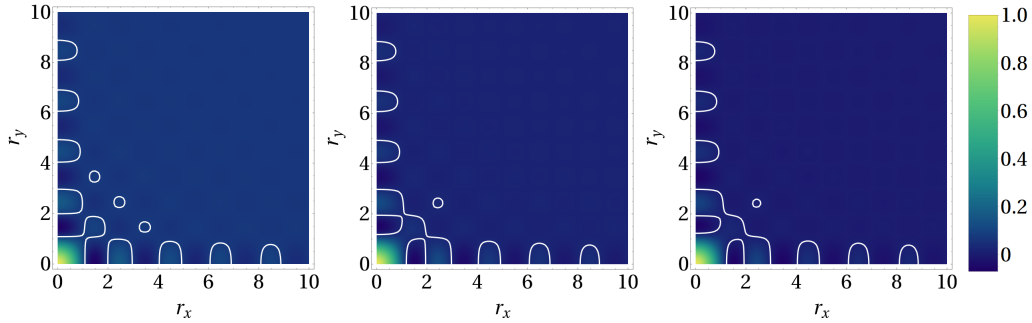

Figure 4.8: Normalized correlation function at finite temperature $C(\vec{r},T)$ for the 2D cubic crystal in colour code. From left to right, $T/\omega_0 = 0, 1, 100$. We stress the prominently weak influence of temperature on most features, specially its spatial distribution.

4.5 Conclusive remarks on physical Insight and experimental Implementation

We have tackled the subtle question if individual units of a spatially extended system undergo dissipation and decoherence from common or separate environments. Whilst a point-like system dissipate in unique bath, for an extended object the physical situation are more sophisticated. A microscopic model is needed to properly determine the relevant scales, the importance of geometric characteristics and the ineffectiveness of spatial correlations. For a system composed by two distant components in a 1D chain environment, the cross-damping never disappears asymptotically, and a periodic cross-over between CB and SB occurs by separating the two system components. This can be understood since at resonance only one normal mode establishes a communication channel between two separate probes. By moving the probes far apart a cross-over between CB and SB occurs periodically depending on the probes position with respect to the resonant normal mode: with one probe in anti-node the other one will be coupled (decoupled) to it through the bath if placed in another anti-node (node) of such resonant phonon. This opens up interesting possibilities in phonon wave-guides Habraken et al. (2012) and surface phononic cavities Schuetz et al. (2015).

For environments with $D > 1$, several normal modes in a $D-1$ manifold will resonate with the system, causing dissipation and decoherence of both probes. The cross-term

will be strongly influenced by the crystal anisotropy being determined by the interference of these modes. Isotropic environment models reproduce the common intuition that, at long distances, probes will always feel a separate environment. We want to stress though that isotropic dispersions can only be assumed when either the environment does not have a fine structure (like for electromagnetic fields in linear media), or when Ω is far below c/ℓ, with c the effective propagation velocity in the medium and ℓ wavelength of the crystal periodicity or distance between disorder patches in an otherwise homogeneous medium Brownnutt et al. (2014). This means that whenever the system has frequencies close to the Debye frequency, anisotropy effects are dominant and dissipation and decoherence are determined by crystal symmetries, which will indeed be felt by the cross-damping. In fact at resonance with high phonon momenta, the lattice structure of the bath is sensed by the system, leading to a non-decaying, directional, bath-mediated interaction between probes, and to a CB/SB transition periodic with the distance. The described scenario arises in a long time limit, when the resonance condition is enforced with the probes interacting only with resonant phonons, as predicted by Fermi golden rule. Transient dynamics will display these features after the build-up of an eventual cross-term in the master equation, being the initial dynamics governed by independent dissipation for the probes. This will occur when a communication channel between the probes is established in the environment, after a time given by the product of their relative distance and the maximum group velocity within the crystal.

Even if at low momenta an isotropic interaction leads to a cross-over from CB to SB for distant probes, the important point is that the spatial scales of this cross-over (the inverse of k_Ω) for crystals in thermal states do *not* follow the correlation function of the bath, which decays as the inverse of the crystal spacing. Also, for distances well-above environment correlation length ξ_c, collective dissipation can occur for 1D crystals (for all system frequencies) or for D-dimensional crystals for probes' frequencies resonant with high crystal momenta. The ineffectiveness of the correlation length as a measure of CB versus SB can be generalized to more generic dissipation mechanisms as follows: whatever the Hamiltonians involved in the setting, the system-bath interaction $H_{SB} = \sum_{i=1,2} S^{(i)} B^{(i)}$ can be either able to cause transitions between system eigenstates (damping, $[S^{(i)}, H_S] \neq 0$) or not (pure dephasing). In presence of damping, cross-talk between probes is realized through resonant energy exchange through the bath, and given by the two-time two-site correlations $\int d\tau e^{i\Omega_\alpha \tau} \left\langle B^{(1)}(\tau) B^{(2)}(0) \right\rangle$ where Ω_α are the different system energy gaps (coming from an eigen-operator decomposition as in usual derivations, Breuer & Petruccione (2002)). On the other hand, the environment correlation is not limited by such resonance. Different is the case of dephasing $[S^{(i)}, H_S] = 0$: here the interaction picture of system operators does not filter the bath second moments to be selected at resonance with the system and the cross-dephasing samples all frequency/momenta components in the environment, as the bath correlator does. Typical spectral densities $\omega^{(D-2)} \exp(-\omega/\omega_c)$ favor small momenta for 1D while for 3D this occurs for frequencies/momenta near the cutoff frequency ω_c Doll et al. (2006)). Thus, correlation length and CB to SB cross-over are still inequivalent in the dephasing case, although cross-talk and correlation will be both spatially decaying functions because both have sampled all momenta (although with different weights). In this case too, a transient SB time will be present before the final spatial cross-talk shape is produced, related with the maximum propagation speed in the medium.

Confirmation of the decribed mechanism for the CB/SB cross-over is seen when focusing on the role of regularity in the crystal geometry. As argued in the 1D case, if crystal modes which are resonant with probes have been localized due to disorder in

the crystal, the cross-talk coming from their overlap $\int d\vec{k} f_{\vec{n},\vec{k}} f^*_{\vec{n}',-\vec{k}} t\,\mathrm{sinc}[t(\omega(\vec{k}-\Omega)]$ will become localized too to shorter distances. This localization will be proportional to the degree of disorder and thus of spatial localization of normal modes. Thus, the cross dissipation, characeristic of a common bath, can generically be seen as the channel established between probes formed by superposition of the medium's resonant modes which are able to spatially connect the two remote probes locations.

One feasible way to experimentally implement the 2D crystal is via trapped ions with a tight axial confinement so that they effectively lie on a plane and form a triangular-symmetric Coulomb crystal, such as in Porras & Cirac (2006). The major problem in that setting is that axial motion is coupled to radial degrees of motion, but this can be overcome if the detuning between the axial frequency and the radial one is sufficiently. The probe ions would need to be sitting in the same plane thus distorting the modes of the Coulomb crystal. Hence the implemented model would result a little bit more complicated, although the basic physics would be the same. Addressability of the probe ions, e.g. by fluorescence Leibfried et al. (2003), would be a central requirement. Another possible way of investigation is the intentional deposition of adatoms, i.e. atoms adsorbed on metallic surfaces. This way has always been seen as a drawback and a source of anomalous heating in ion trap electrodes Hite et al. (2013); Brownnutt et al. (2014), but could suit our purposes. Adatoms bound to a metallic surface can have oscillation frequencies in the THz regime, very close to Debye frequencies of metals (gold for example has a Debye frequency of around 3.6 THz). In this way, by placing intentionally adsorbed atoms at different distances would allow us to check our results. Different masses of these atoms would scan the different frequencies as compared to the maximum phonon frequency of the metallic substrate. For this to be possible we should deal with fluorescent adsorbed atoms which can be trapped in optical molasses. Investigation of cross-damping could be done by exciting the motion of one atom and evaluating the effect on the other. A coupling of the fluorescent transition to the motional degree of freedom would probably be needed, though.

Conclusions

In this thesis I presented and discussed the results of some question I asked as PhD student. The framework of knowledges where I moved is shorthand called quantum technologies, it was born as a speculation on the foundation of quantum mechanics in the low energy regime partially in parallel with the other XX century big discover that is the Standard Model of the fuondamental interactions.

Quantum technologies could be understood as the subsequent revolution of the two that has changed the XX century; one is the development of quantum mechanics in the context of the *normal* science, the other is the development of the Information and Communication Technology. The merging of this two has lead to a seminal field of research called Quantum information and communication that know gather a lots of concepts, tools and results from a broad range physics subdisciplines such as quantum optics and photonics, condensed matter physics and quantum field theory. This merging does not entailed a confusion among branches but instead it has implied the born of new and amazing field of research with unexpected descriptive power, among all quantum biology. My contributions belong to this class of physics where a multiple knowledge is required and multiple implication could have.

In the first part of this thesis the proper use of fidelity when assessing quantum resources has been questioned. We have showed by mean of some example that the usual threshold used to certify that two states are near in the Hilbert space and hence they have the same physical properties, e.g. $F > 0.9$, could lead to adopt states without quantum features instead of pure quantum states. The concept of quantumness is somehow vague and in the second chapter multiple signature of quantum behavior have been adopted. For the single mode gaussian state we have used the singular behavior of their corresponding Glauber P-function and the Subpoissianity accounted by the Fano-factor, both markers signal a non classical mode of radiation in the sense that its properties cannot be derived starting from the Maxwell equations. Then for couple of qubits and a pair of light mode the correlation between them have been investigated, in particular we have chosen the negativity as entanglement quantifier and the discord. All the examples show that we should use with increasing caution fidelity, to certify the presence of quantum characteristics by comparison with a target one, when approaching the border that sunders quantum and classical world. In addition we have shown that adding a suitable number of physical constraints, for example on the energy, can partially avoid the previous commented situation. In contrast imposing too much constraint it is not so different than perform the tomographic reconstruction of the state, hence we have stated that fidelity is for sure a good way to summarize the results of state tomography. A future

development could be a modification of the actual definition of fidelity in order to take in account that mismatching pair of states can reach high values of fidelity.

In the third chapter we have outlined the spin model we employ: the Lipkin-Meshkov-Glick model. It describes critical systems with interaction beyond the first-neighbor approximation. Here we address quantum metrology in LMG systems and show how criticality may be exploited to improve precision. At first we focus on the characterization of LMG systems themselves, i.e., the estimation of anisotropy, and address the problem by considering the quantum Cramer-Rao bound. We evaluate the quantum Fisher information of small-size LMG chains made of N = 2, 3, and 4 lattice sites and also analyze the same quantity in the thermodynamical limit. Our results show that criticality is indeed a resource and that the ultimate bounds to precision may be achieved by tuning the external field and measuring the total magnetization of the system. We then address the use of LMG systems as quantum thermometers and show that:

1. precision is governed by the gap between the lowest energy levels of the systems;
2. field-dependent level crossing is a metrological resource to extend the operating range of the quantum thermometer.

Finally in the fourth section we have questioned again the role of physical intuition: although it is often anticipating formal derivations and the construction of coherent theories may fail and misconceptions not supported by calculation can originate 'folklore' within the community, until it is dispelled by exact results whereby exciting pieces of new research can emerge. This is the case when answering the very general question: given a system composed by several units, are these dissipating separately or collectively? The importance of such apparently technical distinction is that the latter situation is able to produce noiseless subsystems (part of the degrees of freedom of the quantum system not dissipating) or decoherence-free subspaces (part of the system's available quantum states are conserved undissipated), a well-recognized advantage for quantum informational tasks. In our work we clarify the issue with the full power of a microscopic model of a discrete environment, and dispel the widespread "intuitive" misconception relating the correlation length of the environment to the transition from common to independent environments, thus laying the basis for a clear analysis and understanding of the physical conditions for such crossover. Our results, further, go deeply in the positive, predicting novel and surprising effects such as collective dissipation even for system components at large distances, as it occurs for anisotropic dispersions (typical in structured environments) and in 1D. Strikingly, even when a distance-dependent crossover arises this is never related to a correlation length. The full picture arises from a comprehensive analysis of all aspects of the problem, like spatial crystal symmetries, disorder, temperature, extension of system-bath contact regions, each of them introducing interesting and distinctive phenomenology.

Appendices

APPENDIX A

LMG systems with $N = 2, 3, 4$ sites

Here we provide the explicit expression, in the computational basis, of the Hamiltonian for LMG systems with $N = 2, 3, 4$ sites, as well as the eigenvalues and eigenvectors for $N = 2, 3$. Throughout the Section we use the shorthand $u = (\gamma - 1)$ and $v = (\gamma + 1)$.

A.1 N=2

The matrix form of the two-site LMG Hamiltonian in the computational basis reads as follows

$$H_2 = -\frac{1}{2}\begin{pmatrix} 4h & 0 & 0 & u \\ 0 & 0 & v & 0 \\ 0 & v & 0 & 0 \\ u & 0 & 0 & -4h \end{pmatrix} . \tag{A.1}$$

The eigenvalues are given by

$$\lambda_1 = -\frac{1}{2}v \quad \lambda_3 = -\frac{1}{2}\sqrt{16h^2 + u^2} \tag{A.2}$$

$$\lambda_2 = \frac{1}{2}v \quad \lambda_4 = \frac{1}{2}\sqrt{16h^2 + u^2}\,, \tag{A.3}$$

and the corresponding (unnormalized) eigenvectors by

$$\mathbf{u_1^T} = \begin{pmatrix} 0, & 1, & 1, & 0 \end{pmatrix} \tag{A.4}$$

$$\mathbf{u_2^T} = \begin{pmatrix} 0, & -1, & 1, & 0 \end{pmatrix} \tag{A.5}$$

$$\mathbf{u_3^T} = \begin{pmatrix} \frac{4h+\sqrt{16h^2+u^2}}{u}, & 0, & 0, & 1 \end{pmatrix} \tag{A.6}$$

$$\mathbf{u_4^T} = \begin{pmatrix} \frac{4h-\sqrt{16h^2+u^2}}{u}, & 0, & 0, & 1 \end{pmatrix} . \tag{A.7}$$

A.2 N=3

The Hamiltonian for the three-site LMG system is given by

$$H_3 = -\frac{1}{3}\begin{pmatrix} 9h & 0 & 0 & -u & 0 & -u & -u & 0 \\ 0 & 3h & v & 0 & v & 0 & 0 & -u \\ 0 & v & 3h & 0 & v & 0 & 0 & -u \\ -u & 0 & 0 & -3h & 0 & v & v & 0 \\ 0 & v & v & 0 & 3h & 0 & 0 & -u \\ -u & 0 & 0 & v & 0 & -3h & v & 0 \\ -u & 0 & 0 & v & 0 & v & -3h & 0 \\ 0 & -u & -u & 0 & -u & 0 & 0 & -9h \end{pmatrix} , \tag{A.1}$$

leading to the eigenvalues

$$\mu_{1,2} = \frac{1}{3}(v - 3h) \quad \mu_{3,4} = \frac{1}{3}(v + 3h) \tag{A.2}$$

$$\mu_5 = \frac{1}{3}(-3h - v - \Delta_-) \tag{A.3}$$

$$\mu_6 = \frac{1}{3}(-3h - v + \Delta_-) \tag{A.4}$$

$$\mu_7 = \frac{1}{3}(3h - v - \Delta_+) \tag{A.5}$$

$$\mu_8 = \frac{1}{3}(3h - v + \Delta_+) \tag{A.6}$$

and eigenvectors

$$\mathbf{v_1^T} = (0, -1, 0, 0, 1, 0, 0, 0) \tag{A.7}$$

$$\mathbf{v_2^T} = (0, -1, 1, 0, 0, 0, 0, 0) \tag{A.8}$$

$$\mathbf{v_3^T} = (0, 0, 0, -1, 0, 0, 1, 0) \tag{A.9}$$

$$\mathbf{v_4^T} = (0, 0, 0, -1, 0, 1, 0, 0) \tag{A.10}$$

$$\mathbf{v_5^T} = \left(\tfrac{\delta_+ - \Delta_-}{u},\ 0,\ 0,\ 1,\ 0,\ 1,\ 1,\ 0\right) \tag{A.11}$$

$$\mathbf{v_6^T} = \left(\tfrac{\delta_+ + \Delta_-}{u},\ 0,\ 0,\ 1,\ 0,\ 1,\ 1,\ 0\right) \tag{A.12}$$

$$\mathbf{v_7^T} = \left(0,\ \tfrac{\delta_- - \Delta_+}{3u},\ \tfrac{\delta_- - \Delta_+}{3u},\ 0,\ \tfrac{\delta_- - \Delta_+}{3u},\ 0,\ 0,\ 1\right) \tag{A.13}$$

$$\mathbf{v_8^T} = \left(0,\ \tfrac{\delta_- + \Delta_+}{3u},\ \tfrac{\delta_- + \Delta_+}{3u},\ 0,\ \tfrac{\delta_- + \Delta_+}{3u},\ 0,\ 0,\ 1\right) \tag{A.14}$$

where $\Delta_\pm = 2\sqrt{1 + 9h^2 \pm 3hv + \gamma u}$ and $\delta_\pm = -6h \pm v$.

A.3 N=4

The Hamiltonian of a four-site LMG system may be expressed in a block-diagonal form given by

$$H_4 = \begin{pmatrix} A & 0 & \cdots & 0 \\ 0 & B & \cdots & 0 \\ 0 & \cdots & B & 0 \\ 0 & \cdots & 0 & C \end{pmatrix} \tag{A.1}$$

where

$$A = -\frac{1}{4}\begin{pmatrix} 16h & 0 & -\sqrt{6}u & 0 & 0 \\ 0 & 3v + 8h & 0 & -3u & 0 \\ -\sqrt{6}u & 0 & 4v & 0 & -\sqrt{6}u \\ 0 & -3u & 0 & 3v - 8h & 0 \\ 0 & 0 & -\sqrt{6}u & 0 & -16h \end{pmatrix} \tag{A.2}$$

$$B = \frac{1}{4}\begin{pmatrix} v - 8h & 0 & u \\ 0 & 0 & 0 \\ u & 0 & v + 8h \end{pmatrix} \tag{A.3}$$

$$C = \frac{1}{4}\begin{pmatrix} 2v & 0 & 0 & 0 & 0 \\ 0 & v-8h & 0 & u & 0 \\ 0 & 0 & 0 & 0 & 0 \\ 0 & u & 0 & v+8h & 0 \\ 0 & 0 & 0 & 0 & 2v \end{pmatrix}. \tag{A.4}$$

Bibliography

Abramovicz, H., Abt, I., Zarnecki, A., et al. 2013, The European physical journal. C, particles and fields, 73, 1

Allegra, M., Giorda, P., & Paris, M. G. 2010, Physical review letters, 105, 100503

Allegra, M., Giorda, P., & Paris, M. G. 2011, International Journal of Quantum Information, 9, 27

Amico, L., Fazio, R., Osterloh, A., & Vedral, V. 2008, Reviews of Modern Physics, 80, 517

Anderson, P. W. 1958, Physical review, 109, 1492

Banaszek, K., D'Ariano, G. M., Paris, M. G. A., & Sacchi, M. F. 1999, Phys. Rev. A, 61, 010304

Banchi, L., Braunstein, S. L., & Pirandola, S. 2015, Phys. Rev. Lett., 115, 260501

Bell, J. S. 2004, Speakable and unspeakable in quantum mechanics: Collected papers on quantum philosophy (Cambridge university press)

Benatti, F., Floreanini, R., & Piani, M. 2003, Physical review letters, 91, 070402

Benedetti, C., Shurupov, A. P., Paris, M. G., Brida, G., & Genovese, M. 2013, Physical Review A, 87, 052136

Bengtsson, I. & Zyczkowski, K. 2006, Geometry of quantum states: an introduction to quantum entanglement (Cambridge University Press)

Bina, M., Mandarino, A., Olivares, S., & Paris, M. G. 2014, Physical Review A, 89, 012305

BIPM, I., IFCC, I., IUPAC, I., & ISO, O. 2008, Evaluation of measurement data—guide for the expression of uncertainty in measurement. JCGM 100: 2008

Blandino, R., Genoni, M. G., Etesse, J., et al. 2012, Physical review letters, 109, 180402

Botet, R. & Jullien, R. 1983, Physical Review B, 28, 3955

Botet, R., Jullien, R., & Pfeuty, P. 1982, Physical Review Letters, 49, 478

Breuer, H.-P. & Petruccione, F. 2002, The theory of open quantum systems (Oxford university press)

Brody, D. C. & Hughston, L. P. 1996, Physical review letters, 77, 2851

Brownnutt, M., Kumph, M., Rabl, P., & Blatt, R. 2014, arXiv preprint arXiv:1409.6572

Buono, D., Nocerino, G., D'Auria, V., et al. 2010, JOSA B, 27, A110

Cahill, K. E. & Glauber, R. 1969a, Physical Review, 177, 1882

Cahill, K. E. & Glauber, R. 1969b, Physical Review, 177, 1857

Caneva, T., Fazio, R., & Santoro, G. 2009in , IOP Publishing, 012004

Caneva, T., Fazio, R., & Santoro, G. E. 2008, Physical Review B, 78, 104426

Castaños, O., López-Peña, R., Hirsch, J. G., & López-Moreno, E. 2006, Physical Review B, 74, 104118

Castaños, O., López-Peña, R., Nahmad-Achar, E., & Hirsch, J. 2012in , IOP Publishing, 012021

Chen, G., Liang, J.-Q., & Jia, S. 2009, Optics express, 17, 19682

Cialdi, S., Brivio, D., & Paris, M. G. 2010, Applied Physics Letters, 97, 041108

Cialdi, S., Brivio, D., Tabacchini, A., Kadhim, A. M., & Paris, M. G. 2012, Optics letters, 37, 3951

Cialdi, S., Brivio, D., Tesio, E., & Paris, M. G. 2011, Physical Review A, 84, 043817

Cialdi, S., Castelli, F., Boscolo, I., & Paris, M. G. 2008, Applied optics, 47, 1832

Cialdi, S., Castelli, F., & Paris, M. G. 2009, Journal of Modern Optics, 56, 215

Cochrane, P., Ralph, T., & Milburn, G. 2002, Physical Review A, 65, 062306

Cozzini, M., Giorda, P., & Zanardi, P. 2007, Physical Review B, 75, 014439

D'ariano, G., Macchiavello, C., & Paris, M. 1994, Physical Review A, 50, 4298

D'Ariano, G. M., Paris, M. G., & Sacchi, M. F. 2003, Advances in Imaging and Electron Physics, 128, 206

D'Auria, V., Fornaro, S., Porzio, A., et al. 2009, Physical review letters, 102, 020502

Dicke, R. H. 1954, Physical Review, 93, 99

Diehl, S., Micheli, A., Kantian, A., et al. 2008, Nature Physics, 4, 878

Doll, R., Wubs, M., Hänggi, P., & Kohler, S. 2006, EPL (Europhysics Letters), 76, 547

Dorner, U. 2012, New Journal of Physics, 14, 043011

Dowling, J. P. & Milburn, G. J. 2003, Philosophical Transactions of the Royal Society of London A: Mathematical, Physical and Engineering Sciences, 361, 1655

Drever, R., Hall, J. L., Kowalski, F., et al. 1983, Applied Physics B, 31, 97

Dusuel, S. & Vidal, J. 2004, Physical review letters, 93, 237204

Dusuel, S. & Vidal, J. 2005, Physical Review B, 71, 224420

Fano, U. 1957, Reviews of Modern Physics, 29, 74

Fassioli, F., Nazir, A., & Olaya-Castro, A. 2010, The Journal of Physical Chemistry Letters, 1, 2139

Ferraro, A., Olivares, S., & Paris, M. G. 2005, Gaussian states in quantum information (Bibliopolis)

Feynman, R. P. 1982, International journal of theoretical physics, 21, 467

Ford, G. & O'Connell, R. 2014, Physical Review A, 89, 054101

Fuchs, C., Van De Graaf, J., et al. 1999, Information Theory, IEEE Transactions on, 45, 1216

Fuentes-Schuller, I. & Barberis-Blostein, P. 2007, Journal of Physics A: Mathematical and Theoretical, 40, F601

Fulconis, J., Alibart, O., O'Brien, J. L., Wadsworth, W. J., & Rarity, J. G. 2007a, Physical review letters, 99, 120501

Fulconis, J., Alibart, O., O'Brien, J. L., Wadsworth, W. J., & Rarity, J. G. 2007b, Physical review letters, 99, 120501

Galve, F., Giorgi, G. L., & Zambrini, R. 2010, Physical Review A, 81, 062117

Garanin, D., Hidalgo, X. M., & Chudnovsky, E. 1998, Physical Review B, 57, 13639

Garnerone, S., Jacobson, N. T., Haas, S., & Zanardi, P. 2009, Physical review letters, 102, 057205

Gatteschi, D., Sessoli, R., & Villain, J. 2006, Molecular nanomagnets (Oxford University Press)

Genoni, M. G., Giorda, P., & Paris, M. G. 2011, Journal of Physics A: Mathematical and Theoretical, 44, 152001

Genoni, M. G. & Paris, M. G. 2010, Physical Review A, 82, 052341
Genoni, M. G., Paris, M. G., & Banaszek, K. 2008, Physical Review A, 78, 060303
Giorda, P. & Paris, M. G. 2010, Physical review letters, 105, 020503
Giorgi, G. L., Galve, F., Manzano, G., Colet, P., & Zambrini, R. 2012, Physical Review A, 85, 052101
Glauber, R. J. 1963a, Physical Review, 131, 2766
Glauber, R. J. 1963b, Phys. Rev., 131, 2766
Glick, A., Lipkin, H., & Meshkov, N. 1965, Nuclear Physics, 62, 211
Habraken, S., Stannigel, K., Lukin, M. D., Zoller, P., & Rabl, P. 2012, New Journal of Physics, 14, 115004
Helstrom, C. W. 1976, Quantum detection and estimation theory (Academic press)
Hite, D., Colombe, Y., Wilson, A., et al. 2013, MRS bulletin, 38, 826
Huang, L., Guo, Q., Xu, X.-x., & Yuan, W. 2014, International Journal of Theoretical Physics, 53, 3970
Invernizzi, C., Korbman, M., Venuti, L. C., & Paris, M. G. 2008, Physical Review A, 78, 042106
Invernizzi, C. & Paris, M. G. 2010, Journal of Modern Optics, 57, 198
James, D. F., Kwiat, P. G., Munro, W. J., & White, A. G. 2001, Physical Review A, 64, 052312
Jeske, J. & Cole, J. H. 2013, Physical Review A, 87, 052138
Jeske, J., Cole, J. H., & Huelga, S. F. 2014, New Journal of Physics, 16, 073039
Jozsa, R. 1994, Journal of Modern Optics, 41, 2315
Kim, M. S., Park, E., Knight, P. L., & Jeong, H. 2005, Phys. Rev. A, 71, 043805
Kloskowska, E. 2008, Amyloid precursor protein with the Alzheimer´ s disease 670/671 mutation: Animal and cellular models (Institutionen för neurobiologi, vårdvetenskap och samhälle/Department of Neurobiology, Care Sciences and Society)
Kraus, B., Büchler, H., Diehl, S., et al. 2008, Physical Review A, 78, 042307
Kwok, H.-M., Ning, W.-Q., Gu, S.-J., Lin, H.-Q., et al. 2008, Physical Review E, 78, 032103
Larson, J. 2010, EPL (Europhysics Letters), 90, 54001
Lee, C. T. 1991, Physical Review A, 44, R2775
Leibfried, y., Blatt, R., Monroe, C., & Wineland, D. 2003, Reviews of Modern Physics, 75, 281
Lipkin, H. J., Meshkov, N., & Glick, A. 1965, Nuclear Physics, 62, 188
Luo, S. 2008, Phys. Rev. A, 77, 042303
Lvovsky, A. I. & Raymer, M. G. 2009, Reviews of Modern Physics, 81, 299
Lynn, J., Smith, H., & Nicklow, R. 1973, Physical Review B, 8, 3493
Ma, J. & Wang, X. 2009, Physical Review A, 80, 012318
Ma, J., Wang, X., & Gu, S.-J. 2009, Physical Review E, 80, 021124
Mandarino, A., Bina, M., Olivares, S., & Paris, M. G. 2014, International Journal of Quantum Information, 12, 1461015
Marian, P. & Marian, T. A. 2012, Physical Review A, 86, 022340
McCutcheon, D. P., Nazir, A., Bose, S., & Fisher, A. J. 2009, Physical Review A, 80, 022337
Meshkov, N., Glick, A., & Lipkin, H. 1965, Nuclear Physics, 62, 199
Micheli, A., Jaksch, D., Cirac, J. I., & Zoller, P. 2003, Physical Review A, 67, 013607
Miranowicz, A. & Grudka, A. 2004, Journal of Optics B: Quantum and Semiclassical Optics, 6, 542
Morrison, S. & Parkins, A. 2008, Physical review letters, 100, 040403

Neyman, J. 1937, Philosophical Transactions of the Royal Society of London. Series A, Mathematical and Physical Sciences, 236, 333
Nha, H., Lee, S.-Y., Ji, S.-W., & Kim, M. 2012, Physical review letters, 108, 030503
Olivares, S. 2012, The European Physical Journal Special Topics, 203, 3
Olivares, S. & Paris, M. G. 2005, Journal of Optics B: Quantum and Semiclassical Optics, 7, S616
Opatrnỳ, T., Kurizki, G., & Welsch, D.-G. 2000, Physical Review A, 61, 032302
Pan, F. & Draayer, J. 1999, Physics Letters B, 451, 1
Paraoanu, G.-S. & Scutaru, H. 2000, Phys. Rev. A, 61, 022306
Paris, M. G. 2009, International Journal of Quantum Information, 7, 125
Paternostro, M. & Kim, M. 2005, New Journal of Physics, 7, 43
Paul, H. 1982, Reviews of Modern Physics, 54, 1061
Pauli, W. 1933, Handbuch der Physik vol XXIV, part 1, ed Geiger and Scheel (Reprinted 1958 Encyclopedia of Physics vol V, part I
Paz, J. P. & Roncaglia, A. J. 2008, Physical review letters, 100, 220401
Porras, D. & Cirac, J. I. 2006, Physical review letters, 96, 250501
Prokopenko, M., Lizier, J. T., Obst, O., & Wang, X. R. 2011, Physical Review E, 84, 041116
Řeháček, J., Englert, B.-G., & Kaszlikowski, D. 2004, Physical Review A, 70, 052321
Řeháček, J., Olivares, S., Mogilevtsev, D., et al. 2009, Physical Review A, 79, 032111
Reichenbach, H. 1944, Philosophic foundations of quantum mechanics (Courier Corporation)
Ribeiro, P., Vidal, J., & Mosseri, R. 2007, Physical review letters, 99, 050402
Ribeiro, P., Vidal, J., & Mosseri, R. 2008, Physical Review E, 78, 021106
Riste, D., Dukalski, M., Watson, C., et al. 2013, Nature, 502, 350
Rivas Vargas, Á. & Müller, M. 2015, New journal of physics, 17
Roos, C., Lancaster, G., Riebe, M., et al. 2004, Physical review letters, 92, 220402
Rosensteel, G., Rowe, D., & Ho, S. 2008, Journal of Physics A: Mathematical and Theoretical, 41, 025208
Rubin, R. J. 1963, Physical Review, 131, 964
Sachdev, S. 1999, Quantum phase transition, Cambridge Uni
Schuetz, M. J., Kessler, E. M., Giedke, G., et al. 2015, arXiv preprint arXiv:1504.05127
Scutaru, H. 1998, Journal of Physics A: Mathematical and General, 31, 3659
Shannon, C. E. 2001, ACM SIGMOBILE Mobile Computing and Communications Review, 5, 3
Smithey, D., Beck, M., Raymer, M., & Faridani, A. 1993, Physical review letters, 70, 1244
Solinas, P., Ribeiro, P., & Mosseri, R. 2008, Physical Review A, 78, 052329
Sommers, H.-J. & Zyczkowski, K. 2003, Journal of Physics A: Mathematical and General, 36, 10083
Steffen, M., Ansmann, M., Bialczak, R. C., et al. 2006, Science, 313, 1423
Troiani, F. & Zanardi, P. 2013, Physical Review B, 88, 094413
Tsomokos, D. I., Ashhab, S., & Nori, F. 2008, New Journal of Physics, 10, 113020
Turing, A. M. 1936, J. of Math, 58, 5
Twamley, J. 1996, Journal of Physics A: Mathematical and General, 29, 3723
Uhlmann, A. 1976, Reports on Mathematical Physics, 9, 273
Ulyanov, V. & Zaslavskii, O. 1992, Physics reports, 216, 179
Unanyan, R. & Fleischhauer, M. 2003, Physical review letters, 90, 133601

Vasile, R., Galve, F., & Zambrini, R. 2014, Physical Review A, 89, 022109
Venuti, L. C. & Zanardi, P. 2007, Physical review letters, 99, 095701
Verstraete, F., Wolf, M. M., & Cirac, J. I. 2009, Nature physics, 5, 633
Wenger, J., Tualle-Brouri, R., & Grangier, P. 2004, Physical review letters, 92, 153601
Wichterich, H., Vidal, J., & Bose, S. 2010, Physical Review A, 81, 032311
Wolf, A., De Chiara, G., Kajari, E., Lutz, E., & Morigi, G. 2011, EPL (Europhysics Letters), 95, 60008
Zanardi, P., Giorda, P., & Cozzini, M. 2007a, Physical review letters, 99, 100603
Zanardi, P., Giorda, P., & Cozzini, M. 2007b, Physical review letters, 99, 100603
Zanardi, P., Paris, M. G., & Venuti, L. C. 2008, Physical Review A, 78, 042105
Zanardi, P. & Paunković, N. 2006, Physical Review E, 74, 031123
Zell, T., Queisser, F., & Klesse, R. 2009, Physical review letters, 102, 160501
Zhong, Q. & Castleman Jr, A. 2003, in Quantum Phenomena in Clusters and Nanostructures (Springer), 223–258

List of Publications

Refereed publications

Bina M. , Mandarino A., Olivares S. and Paris M.G.A., Drawbacks of the use of fidelity to assess quantum resources Phys. Rev. A **89**, 012305 (2014);

Mandarino A., Bina M., Olivares S. and Paris M.G.A., About the use of fidelity in CV systems Int. J. Quantum Inform. **12** 1461015 (2014);

Salvatori G., Mandarino A., and Paris M.G.A., Quantum metrology in Lipkin-Meshkov-Glick critical systems Phys. Rev. A **90**, 022111 (2014).

Publications in preparation

Galve F., Mandarino A., Paris M.A.G., Benedetti C. and Zambrini R., Microscopic description for the emergence of collective decoherence in extended systems;

Mandarino A., Porto C., Bina M., Olivares S., Cialdi S., and Paris M.G.A., Fidelity in tomographic reconstruction of quantum states.

Acknowledgments

Alla fine è arrivato il momento di riverire e di ringraziare. Il primo ringraziamento va a Matteo Paris, sì per avermi preso a bottega da lui, ma soprattutto per l' insegnamento a praticare gentilezza a casaccio e atti di bellezza privi di senso come avermi permesso di far parte di uno splendido gruppo per questi 3 anni.

Quindi devo un grazie: a Stefano per i consigli e le discussioni degeneranti in improbabili iniziative di commercio di quantum amulets, a Bina (da leggersi a gran voce e con B calabra) per essere un ottimo sodale tanto nel lavoro quanto nell' allestimento di estemporanee piece da avanspettacolo e ai giovani Jacopo e Matteo R. che mi hanno rubato alla solitudine.

Un particolare grazie anzi un muchas gracias a Roberta y Fernando por el derecho a vagabundear y aventurarme romanticamente en la utopía que es la investigacion cientifica.

Grazie a Claudia perché se di fisica ne abbiamo fatta poca insieme, di lacrime e di risate ne abbiamo fatte tante assieme e perché ci accomunerà per sempre un' isola vera e l' inizio della rinascita su un' isola che non c'è.

Ad Ilia il mio appuntamento quotidiano con la follia, a Francesca e ad Ermanna per la pensosa condivisione di diaframmatiche palpitazioni, a Valentina per le verità custodite e perché noi non mentiamo, a Simone l'unico uomo che a distanza di qualche lustro ancora mi sopporta e a Maria Chiara per il costante supporto a non mollare.

E poi grazie agli amici di sempre che non c'è distanza che te li faccia sentire lontani: Cinzia, Omero, Rita, Rosa, Concetta, Angela e Francesca G, Teresa, Paolo, Benedetta e Valentina: le Pu, SaBrina.

Un doveroso e forse il più significativo grazie devo rivolgerlo a Franco: l' esistenza di questa tesi è figlia del nostro incontro quando ero ancora un giovane di belle speranze.

Infine grazie alla mia famiglia al Padre alla Madre e alla Sorella perché ci siamo ancora nonostante le avversità grazie alla malinconica poesia che sospinge le nostre esistenze su un indolente meridiano.